NORTHWESTERN UNIVERSITY

Inelastic Nuclear Resonant Scattering and Its Application to Tin Materials

A DISSERTATION

SUBMITTED TO THE GRADUATE SCHOOL
IN PARTIAL FULFILLMENT OF THE REQUIREMENTS

for the degree

DOCTOR OF PHILOSOPHY

Field of Physics

By

Michael Yu Hu

EVANSTON, ILLINOIS

December 1999

To Grandma

献 给 姥 姥

Everybody knows that in our days more than ever before a man or a woman who wishes to make a genuine contribution to the advancement of science has to specialize: Which means to intensify one's endeavor to learn all that is known within a certain narrow domain and then to try and increase this knowledge by one's own work—by studies, experiments, and thinking. Being engaged in such specialized activity one naturally at times stops to think what it is good for. . . .

You may ask—you are bound to ask me now: What, then, is in your opinion the value of natural science? I answer: Its scope, aim and value is the same as that of any other branch of human knowledge. Ney, none of them alone, only the union of all of them, has any scope or value at all, and that is simply enough described: it is to obey the command of the Delphic deity, $\Gamma\nu\omega\theta\iota\ \sigma\varepsilon\alpha\upsilon\tau\omicron\nu$, get to know yourself.

—Erwin Schrödinger, *Science and Humanism—Physics in Our Time*

Acknowledgments

First of all, I would like to thank my thesis advisor Prof. Donald Ellis for providing the opportunity for me to work at a synchrotron radiation facility, and for his support and guidance throughout the course of my study. One person I could not thank enough is Dr. Ercan E. Alp, who introduced me into the fields of synchrotron radiation and nuclear resonant scattering and has acted as my advisor on a daily basis. His constant encouragement and advices have played an important role in both my professional and personal growth during the past few years. I would also like to thank Dr. Wolfgang Sturhahn, whose knowledge of physics is always a big help and an inspiration to me. His insistence on accuracy and clearity of any statements in scientific writings and discussions has largely shaped my attitude towards physics. I am very much in debt to Dr. Thomas S. Toellner, for I practically learned all my crystal optics from him. I am lucky to be able to work with him, do many experiments together and I surely learned a lot from him. Thanks also go to Dr. Sarvjit D. Shastri, with whom I have had many fun and stimulating discussions. I am very fortunate to have the opportunities to work with and get to know Klaus Quast, Dr. Ralf Röhlsberger, John Sutter, Philip Hession, Dr. Peter L. Lee, and Dr. Gabor Bortel, with whom I have had shared many night shifts and the joy and agonies of daily work. Outside my immediate professional family, I would like to thank Prof. Clyde W. Kimball and Prof. Dennis E. Brown of Northern Illinois University for their interests in my work and the lending of many tin samples to us.

I would also like to express my gratitude to Northwestern University for accepting me into its graduate program and the financial support for my graduate study. I also thank the Advance Photon Source and its staffs for hosting my thesis research work and the help and assistance they have provided.

Finally, I want to thank my wife and my families. Without Lulu's love, understanding, and support, I could not have achieved anything. I owe so much to my parents for their upbringing of me, their support and believing in me. I also thank my parents-in-law, for their love and support. Thanks also go to Joann and Tom Griffith, our friendship started the first day I set foot onto this continent and whose kindness means so much to me.

Contents

List of Tables

List of Figures

Chapter 1

Introduction

Vibrational properties of solids is an important part of our understanding of materials. There are well established experimental techniques to investigate these properties, inelastic thermal neutron scattering, Raman and infrared light scattering, inelastic X-ray scattering. Neutron and light scattering took advantages of the developments in nuclear and laser technologies. Synchrotron radiation, growing out of particle accelerator technologies by the demands of researchers in condensed matter physics and materials science, proves to be an essential tool today and for the future. The intense and collimated beam from synchrotron storage ring makes inelastic X-ray scattering possible. The application of nuclear resonant scattering with synchrotron radiation also provides a new method to study lattice dynamics, and this is the main topic of this thesis. As we will discuss later in detail, this inelastic nuclear resonant scattering (INRS) technique has element selectivity, is able to provide energy spectrum of vibrational modes as well as integrated lattice vibrational properties, such as the recoilless factor and mean kinetic energy per atom. It works with small amount of materials, so is suitable to study impurities, thin films, interfaces, and samples under artificial high pressure. It is a unique and complementary technique for vibrational dynamics studies.

Soon after the discovery of Mössbauer effect [1], it was realized that it is a powerful technique in studying properties of materials. Mössbauer spectroscopy is a common technique now to probe local electronic and magnetic environment of resonant isotopes. In 1974, Ruby suggested using synchrotron radiation to excite nuclei [2]. Gerdau et al., in 1985, made the first unambiguous observations of synchrotron X-rays resonantly scattered from ^{57}Fe nuclei [3]. Since then, the field of nuclear resonant scattering using synchrotron radiation has been progressing rapidly [4]. Nuclear forward scattering and nuclear Bragg scattering were observed and studied at synchrotron sources. Nuclear forward scattering can be regarded as the counterpart of the conventional Mössbauer spectroscopy in time domain. In principle it provides similar information as does Mössbauer spectroscopy. However, to interpret time spectrum for complicated system is not a trivial matter.

One problem in nuclear forward scattering experiment is the overwhelming prompt radiation at synchrotron sources. Since the nuclear resonant level is very narrow, typically on the order of neV, only a tiny portion of the incident beam is contributing to the resonance signal and the rest of it causes enormous background. This prompt radiation is the result of various electronic processes which are much

faster than nuclear resonance commonly used in such studies. It saturates detectors and prevents detecting signals in the early part of time spectrum. The solution is to develop high resolution X-ray optics to cut down incident energy bandwidth from eVs to meVs [5, 6, 7] in conjunction with the use of detectors having large dynamic range [8, 9, 10]. This development eventually paved the way to inelastic nuclear resonant scattering (INRS). In 1995, using a monochromator having 6.7 meV resolution at 14.4 keV, Seto et al. first observed the phonon excitation spectrum of a polycrystalline α-Fe foil [11]. Shortly after, partial phonon density of states were extracted for several iron compounds [12].

In contrast to Mössbauer spectroscopy, inelastic nuclear resonant scattering exploits nuclear resonant absorption with recoil to reveal vibrational dynamics of the resonant isotope. When the low-lying nuclear level of a particular isotope in a crystal is excited by external γ-radiation, the resonant energy is modified by the interaction between the resonating nuclei and its environment. That interaction can be separated into two parts. One is the hyperfine interaction which modifies the nuclear levels. The resulting corrections to the nuclear level of a single nucleus are on the neV energy scale. The other part is the binding forces in the lattice, which determines lattice vibrations and has energy on the order of meV. Because the nuclear force is much stronger than the binding force of a crystal, the nuclear states are decoupled from the lattice vibrational states. The resonant energy can be regarded as a summation of two parts, the nuclear part is the energy difference between the nuclear ground state and the nuclear excited state, the lattice part is the change in the kinetic and cohesive energies of the nuclei, which we can refer as lattice energy. Since the excited nuclear level is very narrow on the energy scale of lattice vibrations, it provides a well defined reference and can be used as a probe to study the lattice energy of the nucleus when resonance occurs. The nuclear part of resonant energy can be determined as the energy of resonance when the lattice energy of the nucleus does not change and it is a constant part of resonant energy. Thus by monitoring the resonant energies, we can find the energy transfer between photon and the lattice, which then reveals the energy states of the lattice.

There are three very different energy scales involved in such experiments. The nuclear resonant energy which is on the order of 10 keV (for ^{119}Sn it is 23.880 keV), the Debye temperature of lattice which is on the order of 100 meV, and the excited nuclear level linewidth which is on the order of 10 neV (for the 23.880 keV level of ^{119}Sn, it is 25.6 neV). In principle, the very narrow nuclear resonance linewidth provides excellent precision in the studies of vibrational states of materials, even for very low energy excitations. However, unless we wish to study low energy lattice excitations, we do not need such a fine probe in lattice dynamics studies. Usually meV or sub-meV resolution is sufficient compared with the typical Debye temperatures. If we can obtain an X-ray beam with meV energy resolution and use it to scan a phonon spectrum, then the overall energy resolution of our experiment will

be just that of the incident beam, since the nuclear resonant level linewidth is negligibly small on this scale. If we think of nuclear resonance as the analyzer in such experiments, its perfect resolution allows us to achieve wanted energy resolution by monochromatizing the incident beam only, not worrying about the analyzer optics. On the other hand, the resonant energy, i.e., the energy of X-rays we need to work with, is very large compared with the energy resolution in such studies. Thus high degree of monochromatization of hard X-rays is required.

The idea of using nuclear recoil to study lattice dynamics had already been presented in early 1960's [13, 14]. But it was impossible to realize in experiments. To perform such experiments, one would require an X-ray source with adequate spectral flux in meV bandwidth and not too big beam size at sample. It also needs to be tunable to provide enough energy difference to scan phonon spectrum. There was no such source until synchrotron radiation became available. Its superior brightness (photons per solid angle per eV per second) over the conventional X-ray generators and radioactive sources made enough room to develop X-ray optics for monochromatization. Today, silicon monochromators can be made to provide a hard X-ray beam with meV bandwidth and a tunability range over a hundred eV. That is a monochromatization of 10^{-7} of hard X-rays.

Another requirement for inelastic nuclear resonant scattering experiments is the time structure of the source. Since nuclear resonance has characteristic lifetime, timing is needed to distinguish it from electronic processes and enough time separation must be allowed between excitations of nuclei in order to observe nuclear excitations through their decays. Synchrotron radiation is a pulsed source and fits in naturally. Electrons or positrons in a storage ring are bundled in bunches and put into selected places among a discrete set of buckets determined by the storage ring RF frequency. By filling the storage ring in different patterns, i.e. filling selected buckets only, one can chose different time structures of incident radiation. The filling pattern one would need for nuclear resonant scattering experiments is a separation of about 100 - 200 ns between adjacent bunches, since the isotopes mostly used have lifetime on the order of 10 - 100 ns. In addition, each pulse length must be significantly smaller than the lifetime of nuclear resonant isotopes so that electronic scattering and nuclear resonance can be distinguished as prompt and delayed radiation respectively. This is also satisfied at the third generation synchrotron facilities, where the pulse length from each bucket is about 100 ps. By using timing technique to look for delayed signals only, one can achieve very good signal-to-noise ratio even for experiments in which the samples have a low concentration of resonant isotopes. The high signal-to-noise ratio allows one to extract from data the higher order contributions such as multi-phonon processes.

This thesis is concerned with the application of inelastic nuclear resonant scattering method, particularly for ^{119}Sn. A detailed study of INRS with synchrotron radiation in general is given in the first chapter, where we start with nuclear resonant

cross section to explain what is measured in such experiments. Then data analysis procedure is described for extracting information from measured spectra. Count rate estimate is also given for establishing the feasibility and planning of experiments. The monochromator development at its resonant energy 23.88 keV is a necessary and important part of realizing INRS experiments for ^{119}Sn. By extending the design of high resolution monochromator at lower energy, we have developed the capability of 1 meV resolution for 24 keV X-rays. A description of the monochromators and their operation is given in Chapter 3. Then in the next chapter, we present results of INRS measurements of several tin materials and compounds. They are more of a demonstrative nature to show the capabilities and limits of this method. More systematic and dedicated experiments are needed to investigate questions in condensed matter physics and materials science. Finally, we will point out a few future developments and applications in the last chapter. This work was done at the Advanced Photon Source (Argonne, Illinois) Sector 3 undulator beamline, which is dedicated to high resolution X-ray scattering.

Chapter 2

Inelastic Nuclear Resonant Scattering

When an X-ray beam with energy close to the nuclear resonant energy of a particular isotope impinges on a material containing that isotope, part of the incident radiation will be absorbed by some of the isotopes which are then excited to a higher nuclear level. Such absorption process has a very large cross section as compared to electronic scattering (see Table 2.1). It was Mössbauer's discovery that this absorption process can happen with an appreciable probability, the so called f-factor, in solids when the incident photons have exactly the same energy as the nuclear resonant energy [1]. This recoilless absorption makes it possible to study hyperfine structure of nuclear ground level and excited level, which sometimes is called the Mössbauer level. Conversely since the hyperfine structure of a nucleus is influenced by its local electronic and magnetic environment, given the nuclear moments one can use this recoilless absorption – the Mössbauer effect – to probe electronic and magnetic structure of materials. It has become a common technique in material characterization and studies.

It was also studied that the absorption with recoil is determined by the lattice dynamics of the material [13, 14]. This inelastic absorption spans a large energy range centered at the resonant energy. The range is estimated by the Debye temperature of material. So the probability density of absorption with recoil is rather small, $(1-f)/2\Theta_{\mathrm{D}}$, compared to that of recoilless absorption, which is f/Γ. Typically, Θ_{D} is about six orders of magnitude larger than Γ. With conventional radioactive sources, whose energy bandwidth is on the order of Γ, the lattice dynamic contribution is negligible. With synchrotron radiation, the energy bandwidth of X-ray beam can be manipulated by X-ray optics, and meV bandwidth can be achieved with high resolution monochromators. This resolution is appropriate for lattice vibration studies. The high brightness of 3rd generation synchrotron sources facilitate enough photon flux in this bandwidth so that the inelastic absorption signals are quite measurable.

In this chapter, after a brief description of nuclear resonant isotope ^{119}Sn, we will calculate the cross section for inelastic nuclear resonant scattering (INRS) and the intensity we expect in such experiments. Data analysis procedure is also outlined.

2.1 Nuclear Resonance of ^{119}Sn

Among all the Mössbauer isotopes, ^{119}Sn is one of the most used. This is particularly true for nuclear resonant experiments at synchrotron sources. Because its resonant

Table 2.1: Mössbauer isotopes whose nuclear resonance has been observed at a synchrotron source. E_0 is the resonant energy, Γ the natural linewidth of the level, $t_{1/2}$ the half-life, α the internal conversion coefficient, σ_0 the maximum nuclear resonant absorption cross section, $E_R = E^2/2Mc^2$ the recoil energy, and A the natural abundance of the isotope.

isotope	E_0 (keV)	Γ (neV)	$t_{1/2}$ (ns)	α	σ_0 $(10^{-20}cm^2)$	E_R (meV)	A (%)	year and reference
^{57}Fe	14.4125*	4.66	97.8	8.21	256	1.96	2.14	1985 [3]
^{169}Tm	8.401	114	4.0	291	23.7	0.224	100	1991[17]
^{119}Sn	23.880†	25.55	17.86	5.12	140	2.57	8.58	1993 [15]
^{83}Kr	9.40	3.10	147	19.6	108	0.571	11.55	1995 [18, 19]
^{181}Ta	6.238	0.067	6800	80	94	0.115	99.988	1995 [20]
^{151}Eu	21.542‡	47	9.7	28.6	23.8	1.65	47.82	1997 [21]
^{161}Dy	25.655	16.2	28.2	2.9	95	2.19	18.88	1997 [21]

* by Yu. V. Shvyd'ko, 1999.
† by E. E. Alp et al., 1993.
‡ by O. Leopold, 1996.

energy is not too high so that there is efficient optics to handle X-rays at this energy. Its lifetime is not too short so that it can be distinguished from prompt scattering, and is not too long either so that with certain filling patterns of the storage ring all the excited nuclei essentially have decayed and are back in the ground state before the X-rays generated by the next bunch arrive. The first ^{119}Sn nuclear resonance at a synchrotron source was observed in 1993 [15]. Since then, the optics developments at several synchrotron sources have made this isotope an easily accessible one. This thesis is part of the effort to provide this capability. In Table 2.1 we list nuclear resonant isotopes that have been used with synchrotron sources [4]. Their resonant properties are taken from reference [16], unless otherwise indicated.

^{119}Sn is a stable isotope of Sn with natural abundance of 8.6%. The ground state is $\frac{1}{2}^+$. The first excited state is $\frac{3}{2}^+$. It is a Mössbauer level, with excitation energy $E = 23.880keV$, lifetime $\tau = 25.6ns$. The natural linewidth of this level is $\Gamma = 25.6neV$. The internal conversion coefficient $\alpha = 5.12$, the energy of the conversion electron is about 19.4 keV. The internally converted electron is from the

L atomic shell instead of K-shell since the binding energy for K-electron is 29.2 keV. Because of the low L-fluorescence yield, $\omega_L = 0.07$, for one nuclear fluorescence γ-ray ($23.88keV$) there is only 0.36 atomic fluorescence X-ray (about 3.5 keV). The next excited level is $\frac{11}{2}^-$, with $E = 89.5keV$, half-life $t_{1/2} = 245$ days. There is no transition from this level to ground level $\frac{1}{2}^+$. However, it decays to the Mössbauer level by internal conversion most of the time (the internal conversion coefficient $\alpha = 1860$).

The maximum nuclear resonant absorption cross section is an important characteristic number for nuclear resonant processes. Later we will see that the measured intensity is proportional to this number. It is given [22] by

$$\sigma_0 = \frac{\lambda^2}{2\pi}\frac{2I+1}{2I_0+1}\frac{\Gamma_R}{\Gamma} = \frac{2\pi}{1+\alpha}\left(\frac{\hbar c}{E_0}\right)^2\frac{2I+1}{2I_0+1}, \tag{2.1}$$

where λ is the wavelength, I and I_0 are the spins of the Mössbauer level and ground level respectively, Γ_R is the partial linewidth due to gamma-decay, while Γ is the total natural linewidth.

2.2 Inelastic Nuclear Resonant Scattering Cross Section

Nuclear resonant absorption is measured by detecting nuclear decay events following the absorption. The decay channels include nuclear fluorescence which has energy close to the transition energy, electrons ejected by internal conversion process, and atomic fluorescence following the electron ejection. Due to strong scattering of electrons inside material, only the internal conversion electrons come from near the surface can be observed. So in most cases, we are only looking for photons as decay products. The intrinsic relative intensity between nuclear and atomic fluorescences is determined by internal conversion coefficient and atomic fluorescence yield. However, due to the different energies of nuclear and atomic radiations, there is a difference in detection efficiencies for each channel, which mainly involves their electronic absorption lengthes in the sample, in the detector window material, and detector efficiency for different energy photons.

The isotopes often used have large internal conversion coefficients, thus they are more of absorbers than scatterers. So, often we can see more atomic fluorescence than nuclear fluorescence. ^{57}Fe is an example, for which the internal conversion channel makes bigger contribution than the radiative channel. With an internal coefficient of 8.21 and K-fluorescence yield of 0.347, there are 2.85 atomic fluorescence photons for every nuclear fluorescence photon. The total electronic absorptions of both nuclear (14.413 keV) and atomic fluorescences (about 6.4 keV for K-fluorescence) are about the same by Fe atoms[1]. So they have about same chance to escape the sample if iron

[1]The Fe atomic absorption cross section is 5870 $barn$ for 14.413 keV and 6413 $barn$ for 6.4 keV. Fe has K-edge at 7.112 keV.

dominates in the sample. Detector efficiency is higher for the lower energy atomic fluorescence. In ^{57}Fe INRS experiments, the 6.4 keV radiation, i.e., the internal conversion channel dominates the delayed signals.

The situation is different for ^{119}Sn. As discussed in Section 2.1, there is only about one third atomic fluorescence photon for every nuclear fluorescence photon from nuclear decays. In addition, the atomic fluorescence has an energy of about 3.5 keV which is more strongly attenuated in the sample. So generally in ^{119}Sn INRS experiments we are detecting the radiative channel.

The internal conversion channel is completely incoherent, since the atomic configuration is changed by the decay process at the atom where nuclear decay happens. For radiative channel, there are coherent elastic scattering processes, including nuclear forward scattering (NFS) and nuclear Bragg scattering (NBS), which are the subjects of intensive studies [4]. However, when the incident photon is absorbed inelastically, phonon is created or annihilated and the lattice is driven away from thermal equilibrium. Since nuclear decay is a slow process comparing to lattice vibrations, as it happens about 10 or 100 ns after the excitation, while lattice vibrations have a time scale on the order of ps. So, by the time the excited nucleus decays, the lattice is already back to thermal equilibrium and cannot stay in the state right after the absorption. It is in this sense we say that nuclear decay is decoupled from inelastic absorption. So if we count all nuclear decay events without doing energy and momentum analysis, as it is done in INRS experiments, the problem becomes absorption instead of scattering. The spectrum measured in this way is then described by the absorption cross section calculated by Singwi and Sjölander [14]. In the following paragraphs, we will give this derivation. A comprehensive study of incoherent nuclear resonant scattering in the frame of QED can be found in Ref. [23].

Since nuclear interaction is much stronger than lattice forces, the total wave function can be factorized with one factor depending only on the centers of mass of all nuclei, which represents the lattice states, and the other one depending on relative nucleon coordinates inside a nucleus, which represents the nuclear states. Let $|\xi\rangle$ represent lattice state of the scattering system, then the transition matrix element for photon absorption is

$$M_\nu = a \langle \xi_f | e^{i\vec{\mathbf{k}}\vec{\mathbf{r}}_\nu} | \xi_i \rangle \,, \tag{2.2}$$

for the ν-th nucleus in the lattice, where $\vec{\mathbf{r}}_\nu$ is its coordinate and $\vec{\mathbf{k}}$ is the incident photon wave vector. It describes a sudden momentum transfer of $\hbar\vec{\mathbf{k}}$ to the lattice. The initial lattice state $|\xi_i\rangle$ has a distribution governed by the statistical weight factor g_i at certain temperature. The factor a is a constant related to nuclear transition.

By Fermi's Golden Rule, the absorption cross section can be expressed in terms of transition matrix element. For a collection of resonant isotopes in the sample, the cross section is simply the sum over all resonant nuclei, provided that the incident beam is not too strong so that only one photon is absorbed. This is because inelastic

single photon absorptions by individual nuclei are independent. Later on we will show that the single photon absorption requirement is satisfied with today's synchrotron storage ring. The cross sections are obtained by summing over all possible excited states $|\xi_f\rangle$, and averaging over initial states $|\xi_i\rangle$,

$$\sigma(E,\vec{\mathbf{k}}) = \frac{\sigma_0\Gamma^2}{4}\sum_{i,f} g_i \frac{1}{N}\sum_{\nu} \frac{\left|\left\langle \xi_f | e^{i\vec{\mathbf{k}}\vec{\mathbf{r}}_\nu} | \xi_i \right\rangle\right|^2}{(E+\varepsilon_i-\varepsilon_f-E_0)^2+\Gamma^2/4} \tag{2.3}$$

where σ_0 is the nuclear resonant absorption cross section (Eq. 2.1) and E_0 is the nuclear resonant transition energy. ε_i and ε_f are energies of initial and excited lattice states respectively. N is the total number of resonant isotopes.

If we replace the energy denominator by the following,

$$\frac{1}{(E+\varepsilon_i-\varepsilon_f-E_0)^2+\Gamma^2/4} = \frac{1}{\hbar\Gamma}\int_{-\infty}^{\infty} dt\, e^{-\frac{i}{\hbar}(E-E_0)t} e^{-\frac{\Gamma}{2\hbar}|t|} e^{-\frac{i}{\hbar}\varepsilon_i t} e^{\frac{i}{\hbar}\varepsilon_f t} \tag{2.4}$$

and introduce Heisenberg operator $\vec{\mathbf{r}}(t) = e^{\frac{i}{\hbar}Ht}\vec{\mathbf{r}}_\nu e^{-\frac{i}{\hbar}Ht}$, then the cross section can be written as,

$$\begin{aligned}
\sigma(E,\vec{\mathbf{k}}) &= \frac{\sigma_0\Gamma}{4\hbar}\int_{-\infty}^{+\infty} dt\, e^{-\frac{i}{\hbar}(E-E_0)t} e^{-\frac{\Gamma}{2\hbar}|t|} \sum_i g_i \left\langle \xi_i \left| \frac{1}{N}\sum_\nu e^{-i\vec{\mathbf{k}}\vec{\mathbf{r}}_\nu(0)} e^{i\vec{\mathbf{k}}\vec{\mathbf{r}}_\nu(t)} \right| \xi_i \right\rangle \\
&= \frac{\sigma_0\Gamma}{4\hbar}\int_{-\infty}^{\infty} dt\, e^{-\frac{i}{\hbar}(E-E_0)t} \left\langle \frac{1}{N}\sum_\nu e^{-i\vec{\mathbf{k}}\vec{\mathbf{r}}_\nu(0)} e^{i\vec{\mathbf{k}}\vec{\mathbf{r}}_\nu(t)} \right\rangle_T
\end{aligned} \tag{2.5}$$

where Γ is taken to be zero in the exponential $exp(-\frac{\Gamma}{2\hbar}t)$, because we are interested in lattice vibrations which is on an energy scale much greater than it. And $\langle\cdots\rangle_T$ represents the statistical average at given temperature T.

2.3 Autocorrelation Function

In the above expression of INRS cross section (Eq. 2.5), we define a function $F_s(\vec{\mathbf{k}},t)$ to be the thermal average term,

$$F_s(\vec{\mathbf{k}},t) \equiv \left\langle \frac{1}{N}\sum_\nu e^{-i\vec{\mathbf{k}}\vec{\mathbf{r}}_\nu(0)} e^{i\vec{\mathbf{k}}\vec{\mathbf{r}}_\nu(t)} \right\rangle_T \tag{2.6}$$

By performing a Fourier transform on it, we have

$$\begin{aligned}
G_s(\vec{\mathbf{r}},t) &= \frac{1}{(2\pi)^3}\int d\vec{\mathbf{k}}\, e^{-i\vec{\mathbf{k}}\vec{\mathbf{r}}} F_s(\vec{\mathbf{k}},t) \\
&= \left\langle \frac{1}{N}\sum_\nu \frac{1}{(2\pi)^3}\int d\vec{\mathbf{k}}\, e^{-i\vec{\mathbf{k}}[\vec{\mathbf{r}}+\vec{\mathbf{r}}_\nu(0)]}\, e^{i\vec{\mathbf{k}}\vec{\mathbf{r}}_\nu(t)} \right\rangle_T \\
&= \frac{1}{N}\left\langle \sum_\nu \int d\vec{\mathbf{r}'}\, \delta\left(\vec{\mathbf{r}}+\vec{\mathbf{r}}_\nu(0)-\vec{\mathbf{r}'}\right)\delta\left(\vec{\mathbf{r}'}-\vec{\mathbf{r}}_\nu(t)\right) \right\rangle_T
\end{aligned} \tag{2.7}$$

which is recognized as the particle autocorrelation function of a many-body system [24]. That is the reason we put a subscript s to both functions G and F to indicate this single particle autocorrelation. This is the direct result of the fact that the total absorption cross section is just a sum of cross sections of individual nuclei. $F(\vec{\mathbf{k}}, t)$ is called the intermediate scattering function of a many-body system, while in this case it is only its autocorrelation part. Thus the cross section is related to this correlation function by,

$$\sigma(E, \vec{\mathbf{k}}) = \frac{\pi}{2\hbar}\sigma_0\Gamma \ \frac{1}{2\pi}\int dt d\vec{\mathbf{r}}\, e^{i(\vec{\mathbf{k}}\vec{\mathbf{r}}-\omega t)} G_s(\vec{\mathbf{r}}, t) \tag{2.8}$$

where $\hbar\omega = E - E_0$. The general relationship between correlation functions and scattering cross section of an interacting many-body system is discussed by van Hove [24].

Now we define another function $S_s(\omega, \vec{\mathbf{k}})$ to be

$$S_s(\omega, \vec{\mathbf{k}}) \equiv \frac{1}{2\pi}\int dt d\vec{\mathbf{r}}\, e^{i(\vec{\mathbf{k}}\vec{\mathbf{r}}-\omega t)} G_s(\vec{\mathbf{r}}, t) \tag{2.9}$$

It is similar to the dynamic structure factor defined by the same equation but using instead the particle pair correlation function,

$$G(\vec{\mathbf{r}}, t) = \frac{1}{N}\left\langle \sum_{\nu,\mu}\int d\vec{\mathbf{r}'}\, \delta\left(\vec{\mathbf{r}} + \vec{\mathbf{r}}_\nu(0) - \vec{\mathbf{r}'}\right)\delta\left(\vec{\mathbf{r}'} - \vec{\mathbf{r}}_\mu(t)\right)\right\rangle_T \tag{2.10}$$

The dynamic structure factor $S(\omega, \vec{\mathbf{k}})$ is a function of energy and momentum transfer and can be probed by inelastic X-ray scattering and coherent inelastic neutron scattering. Phonon dispersion surface can be mapped out by measuring the dynamic structure factor in the entire energy and momentum range. In contrast, the function $S_s(\omega, \vec{\mathbf{k}})$ obtained by inelastic nuclear resonant scattering is a function of incident X-ray energy and momentum instead of energy and momentum transfers and its interpretation is less direct than that of dynamic structure factor. Now we can rewrite the cross section in terms of $S_s(\omega, \vec{\mathbf{k}})$,

$$\sigma(E, \vec{\mathbf{k}}) = \frac{\pi}{2\hbar}\sigma_0\Gamma\, S_s(\omega, \vec{\mathbf{k}}) \tag{2.11}$$

where $\hbar\omega = E - E_0$. This equation relates what we measure in INRS experiments with the dynamical properties of sample. We shall call function $S_s(\omega, \vec{\mathbf{k}})$ the phonon excitation probability density. Next we will discuss some properties of $S_s(\omega, \vec{\mathbf{k}})$ and the information contained in this function. In the following discussions, we will omit the subscript s which denotes the self-correlation of $S_s(\omega, \vec{\mathbf{k}})$ to make formulas and equations less crowded. However, we should always keep in mind that in the context of INRS the function $S(\omega, \vec{\mathbf{k}})$ is not the same as commonly recognized dynamic structure factor.

2.4 Phonon Excitation Probability Function

The function $S(\omega, \vec{\mathbf{k}})$ is related to the intermediate scattering function by Fourier transform,

$$\begin{aligned} S(\omega, \vec{\mathbf{k}}) &= \frac{1}{2\pi} \int dt\, e^{-i\omega t}\, F_s(\vec{\mathbf{k}}, t) \qquad (2.12) \\ &= \frac{1}{2\pi} \int dt\, e^{-i\omega t} \left\langle \frac{1}{N} \sum_\nu e^{-i\vec{\mathbf{k}}\vec{\mathbf{r}}_\nu(0)} e^{i\vec{\mathbf{k}}\vec{\mathbf{r}}_\nu(t)} \right\rangle_T \\ F_s(\vec{\mathbf{k}}, t) &= \int d\omega\, e^{i\omega t}\, S(\omega, \vec{\mathbf{k}}) \qquad (2.13) \end{aligned}$$

and it can be shown that $S(\omega, \vec{\mathbf{k}})$ is normalized to 1 with respect to energy,

$$\begin{aligned} \int_{-\infty}^{+\infty} S(\omega, \vec{\mathbf{k}})\, d\omega &= \int dt F_s(\vec{\mathbf{k}}, t)\, \frac{1}{2\pi} \int_{-\infty}^{+\infty} e^{-i\omega t}\, d\omega \\ &= \int dt \left\langle \frac{1}{N} \sum_\nu e^{-i\vec{\mathbf{k}}\vec{\mathbf{r}}_\nu(0)} e^{i\vec{\mathbf{k}}\vec{\mathbf{r}}_\nu(t)} \right\rangle_T \delta(t) \\ &= \left\langle \frac{1}{N} \sum_\nu e^{-i\vec{\mathbf{k}}\vec{\mathbf{r}}_\nu(0)} e^{i\vec{\mathbf{k}}\vec{\mathbf{r}}_\nu(0)} \right\rangle_T \\ &= 1 \qquad (2.14) \end{aligned}$$

We know that when there is a sudden momentum transfer, moment sum rules will apply [25]. To verify this we will calculate first few moments $\langle \omega^n \rangle$ of the function $S(\omega, \vec{\mathbf{k}})$. In order to do this, it is useful to trace back the thermal average term and express it in terms of modulus square of transition matrix elements.

$$S(\omega, \vec{\mathbf{k}}) = \frac{\hbar\Gamma}{2\pi} \sum_i g_i \frac{1}{N} \sum_\nu \sum_m \frac{\left\langle \xi_i | e^{-i\vec{\mathbf{k}}\vec{\mathbf{r}}_\nu} | \xi_m \right\rangle \left\langle \xi_m | e^{i\vec{\mathbf{k}}\vec{\mathbf{r}}_\nu} | \xi_i \right\rangle}{(E + \varepsilon_i - \varepsilon_m - E_0)^2 + \Gamma^2/4} \qquad (2.15)$$

As mentioned before, on the energy scale of lattice vibrations, the nuclear resonant linewidth Γ is negligibly small, so it is justified to use the following identity,

$$\lim_{\Gamma \to 0} \frac{\Gamma/2\pi}{(E + \varepsilon_i - \varepsilon_m - E_0)^2 + \Gamma^2/4} = \delta(E - E_0 + \varepsilon_i - \varepsilon_m)$$

Then it reads,

$$S(\omega, \vec{\mathbf{k}}) = \frac{1}{N} \sum_\nu \sum_{i,m} g_i \left\langle \xi_i | e^{-i\vec{\mathbf{k}}\vec{\mathbf{r}}_\nu} | \xi_m \right\rangle \left\langle \xi_m | e^{i\vec{\mathbf{k}}\vec{\mathbf{r}}_\nu} | \xi_i \right\rangle \hbar\delta(\hbar\omega + \varepsilon_i - \varepsilon_m) \qquad (2.16)$$

from which we calculate its moments.

$$\begin{aligned}
\langle \omega^n \rangle &= \int_{-\infty}^{+\infty} \omega^n S(\omega, \vec{\mathbf{k}})\, d\omega \\
&= \frac{1}{N} \sum_{\nu} \sum_{i,m} g_i \left\langle \xi_i | e^{-i\vec{\mathbf{k}}\vec{\mathbf{r}}_\nu} | \xi_m \right\rangle \left\langle \xi_m | e^{i\vec{\mathbf{k}}\vec{\mathbf{r}}_\nu} | \xi_i \right\rangle \int_{-\infty}^{+\infty} \omega^n \hbar \delta(\hbar\omega + \varepsilon_i - \varepsilon_m) d\omega \\
&= \frac{1}{N} \sum_{\nu} \sum_{i,m} g_i \left\langle \xi_i | e^{-i\vec{\mathbf{k}}\vec{\mathbf{r}}_\nu} | \xi_m \right\rangle \left\langle \xi_m | e^{i\vec{\mathbf{k}}\vec{\mathbf{r}}_\nu} | \xi_i \right\rangle (\varepsilon_m - \varepsilon_i)^n \frac{1}{\hbar^n} \\
&= \frac{1}{\hbar^n N} \sum_{\nu} \sum_{i} g_i \left\langle \xi_i | e^{-i\vec{\mathbf{k}}\vec{\mathbf{r}}_\nu} (H - \varepsilon_i)^n e^{i\vec{\mathbf{k}}\vec{\mathbf{r}}_\nu} | \xi_i \right\rangle \qquad (2.17)
\end{aligned}$$

where H is the Hamiltonian of lattice, and we have

$$\begin{aligned}
H &= \sum_{\mu} \frac{\vec{\mathbf{p}}_\mu^2}{2M} + V(\vec{\mathbf{r}}) \qquad (2.18) \\
e^{-i\vec{\mathbf{k}}\vec{\mathbf{r}}_\nu} H e^{i\vec{\mathbf{k}}\vec{\mathbf{r}}_\nu} &= \sum_{\mu} e^{-i\vec{\mathbf{k}}\vec{\mathbf{r}}_\nu} \frac{\vec{\mathbf{p}}_\mu^2}{2M} e^{i\vec{\mathbf{k}}\vec{\mathbf{r}}_\nu} + V(\vec{\mathbf{r}}) \\
&= \sum_{\mu} \frac{\vec{\mathbf{p}}_\mu^2}{2M} + \left[i\vec{\mathbf{k}}\vec{\mathbf{r}}_\nu, \frac{\vec{\mathbf{p}}_\nu^2}{2M} \right] + \frac{1}{2} \left[i\vec{\mathbf{k}}\vec{\mathbf{r}}_\nu, \left[i\vec{\mathbf{k}}\vec{\mathbf{r}}_\nu, \frac{\vec{\mathbf{p}}_\nu^2}{2M} \right] \right] + V(\vec{\mathbf{r}}) \\
&= H - \frac{\hbar\vec{\mathbf{k}}\vec{\mathbf{p}}_\nu}{M} + \frac{\hbar^2 k^2}{2M} \qquad (2.19)
\end{aligned}$$

where $\vec{\mathbf{p}}_\nu$ is the momentum of ν-th atom, and M is the mass of the atom. Over a typical phonon spectrum the incident X-ray wave vector changes very little from the resonant wave vector k_0, so the last term can be approximated by $\hbar^2 k_0^2 / 2M = E_R$, the nuclear recoil energy.

If we calculate moments $\langle (\hbar\omega - E_R)^n \rangle$ instead of $\langle \omega^n \rangle$, then

$$\begin{aligned}
\langle (\hbar\omega - E_R)^n \rangle &= \frac{1}{N} \sum_{\nu} \sum_{i} g_i \left\langle \xi_i \middle| \left(H - \varepsilon_i - \frac{\hbar\vec{\mathbf{k}}\vec{\mathbf{p}}_\nu}{M} \right)^n \middle| \xi_i \right\rangle \qquad (2.20) \\
\langle (\hbar\omega - E_R)^1 \rangle &= \frac{1}{N} \sum_{\nu} \sum_{i} g_i \left\langle \xi_i \middle| \left(H - \varepsilon_i - \frac{\hbar\vec{\mathbf{k}}\vec{\mathbf{p}}_\nu}{M} \right) \middle| \xi_i \right\rangle \\
&= -\frac{\hbar\vec{\mathbf{k}}}{M} \frac{1}{N} \sum_{\nu} \sum_{i} g_i \left\langle \xi_i \middle| \vec{\mathbf{p}}_\nu \middle| \xi_i \right\rangle \quad = \quad 0 \qquad (2.21) \\
\langle (\hbar\omega - E_R)^2 \rangle &= \frac{1}{N} \sum_{\nu} \sum_{i} g_i \left\langle \xi_i \middle| \left(H - \varepsilon_i - \frac{\hbar\vec{\mathbf{k}}\vec{\mathbf{p}}_\nu}{M} \right)^2 \middle| \xi_i \right\rangle \\
&= \frac{1}{N} \sum_{\nu} \sum_{i} g_i \left\langle \xi_i \middle| \left(\frac{\hbar\vec{\mathbf{k}}\vec{\mathbf{p}}_\nu}{M} \right)^2 \middle| \xi_i \right\rangle
\end{aligned}$$

$$= 4\,E_R\;\overline{T}(\hat{\mathbf{k}}) \tag{2.22}$$

$$\begin{aligned}
\langle(\hbar\omega - E_R)^3\rangle &= \frac{1}{N}\sum_{\nu}\sum_{i} g_i \left\langle \xi_i \middle| \left(H - \varepsilon_i - \frac{\hbar\vec{\mathbf{k}}\vec{\mathbf{p}}_\nu}{M}\right)^3 \middle| \xi_i \right\rangle \\
&= \frac{1}{N}\sum_{\nu}\sum_{i} g_i \left\langle \xi_i \middle| \frac{\hbar\vec{\mathbf{k}}\vec{\mathbf{p}}_\nu}{M}\left(H - \varepsilon_i - \frac{\hbar\vec{\mathbf{k}}\vec{\mathbf{p}}_\nu}{M}\right)\frac{\hbar\vec{\mathbf{k}}\vec{\mathbf{p}}_\nu}{M} \middle| \xi_i \right\rangle \\
&= \frac{\hbar^2k^2}{M^2}\frac{1}{N}\sum_{\nu}\sum_{i} g_i \left\langle \xi_i \middle| \left(P_{\nu 0} H P_{\nu 0} - \frac{H P_{\nu 0}^2 + P_{\nu 0}^2 H}{2}\right) \middle| \xi_i \right\rangle \\
&= -\frac{\hbar^2k^2}{2M^2}\frac{1}{N}\sum_{\nu}\sum_{i} g_i \left\langle \xi_i \middle| [P_{\nu 0}, [P_{\nu 0}, H]] \middle| \xi_i \right\rangle \\
&= \frac{E_R}{M}\frac{1}{N}\sum_{\nu}\sum_{i} g_i \left\langle \xi_i \middle| \hbar^2\frac{\partial^2 V}{\partial r_{\nu 0}^2} \middle| \xi_i \right\rangle \\
&= \frac{E_R}{M}\hbar^2\;\overline{K}(\hat{\mathbf{k}})
\end{aligned} \tag{2.23}$$

where $\overline{T}(\hat{\mathbf{k}})$ is the average kinetic energy per atom along the incident beam direction $\hat{\mathbf{k}}$. $P_{\nu 0}$ is the $\hat{\mathbf{k}}$-component of momentum of ν-th atom and $\overline{K}(\hat{\mathbf{k}})$ is the average force constant along $\hat{\mathbf{k}}$-direction. Since the nuclear recoil energy is well known, the first moment sum rule (Eq.2.21) can be used to normalize the measured spectrum, which will be discussed later.

The above results show that certain lattice dynamic quantities can be obtained by simply calculating the first few moments of the measured spectrum. Such obtained quantities have directional dependence in general. We can expect this directional effect in high symmetry single crystal sample and indeed such anisotropy was observed in $^{57}FeBO_3$ single crystal [26, 27]. For polycrystalline sample, due to the random orientation of the constituent crystallites, it is equivalent to average $S(\omega, \vec{\mathbf{k}})$ over full 4π solid angle. In such cases, we have,

$$S(\omega) \equiv \int \frac{d\Omega}{4\pi} S(\omega, \vec{\mathbf{k}}) \tag{2.24}$$

$$\int_{-\infty}^{+\infty} S(\omega)\, d\omega = \int \frac{d\Omega}{4\pi} \int_{-\infty}^{+\infty} S(\omega, \vec{\mathbf{k}})\, d\omega = 1 \tag{2.25}$$

$$\int_{-\infty}^{+\infty} \hbar\omega S(\omega)\, d\omega = \int \frac{d\Omega}{4\pi} \int_{-\infty}^{+\infty} \hbar\omega S(\omega, \vec{\mathbf{k}})\, d\omega = E_R \tag{2.26}$$

$$\int_{-\infty}^{+\infty} (\hbar\omega - E_R)^2 S(\omega)\, d\omega = \int \frac{d\Omega}{4\pi} \int_{-\infty}^{+\infty} (\hbar\omega - E_R)^2 S(\omega, \vec{\mathbf{k}})\, d\omega = \frac{4}{3} E_R\;\overline{T} \tag{2.27}$$

$$\int_{-\infty}^{+\infty} (\hbar\omega - E_R)^3 S(\omega)\, d\omega = \int \frac{d\Omega}{4\pi} \int_{-\infty}^{+\infty} (\hbar\omega - E_R)^3 S(\omega, \vec{\mathbf{k}})\, d\omega = \frac{E_R}{M}\frac{\hbar^2}{3}\overline{K} \tag{2.28}$$

where $\overline{T}$ and $\overline{K}$ are respectively, the mean kinetic energy per atom of, and mean force constant experienced by the resonant nuclei.

Next, we will prove an important property of the phonon excitation probability function for a system in thermal eqilibrium. It is the general detailed balance relation.

$$S(-\omega, -\vec{\mathbf{k}}) = e^{-\beta\hbar\omega} S(\omega, \vec{\mathbf{k}}) \tag{2.29}$$

where $\beta = 1/k_B T$. The validity of above relation can be shown by rewriting Eq. (2.16) with $-\omega$ and $-\vec{\mathbf{k}}$, and replacing g_i by $e^{-\beta\hbar\omega_i}/Z$, where Z is the partition function of the system.

$$S(-\omega, -\vec{\mathbf{k}}) = \frac{1}{N} \sum_{\nu} \sum_{i,m} \frac{e^{-\beta\hbar\omega_i}}{Z} \left\langle \xi_i | e^{+i\vec{\mathbf{k}}\vec{\mathbf{r}}_\nu} | \xi_m \right\rangle \left\langle \xi_m | e^{-i\vec{\mathbf{k}}\vec{\mathbf{r}}_\nu} | \xi_i \right\rangle \hbar\delta(-\hbar\omega + \varepsilon_i - \varepsilon_m)$$

$$= \frac{1}{N} \sum_{\nu} \sum_{i,m} e^{\beta\hbar(\omega_m - \omega_i)} \frac{e^{-\beta\hbar\omega_m}}{Z} \left\langle \xi_m | e^{-i\vec{\mathbf{k}}\vec{\mathbf{r}}_\nu} | \xi_i \right\rangle \left\langle \xi_i | e^{+i\vec{\mathbf{k}}\vec{\mathbf{r}}_\nu} | \xi_m \right\rangle \hbar\delta(\hbar\omega + \varepsilon_m - \varepsilon_i)$$

$$= e^{-\beta\hbar\omega} \frac{1}{N} \sum_{\nu} \sum_{m,i} g_m \left\langle \xi_m | e^{-i\vec{\mathbf{k}}\vec{\mathbf{r}}_\nu} | \xi_i \right\rangle \left\langle \xi_i | e^{+i\vec{\mathbf{k}}\vec{\mathbf{r}}_\nu} | \xi_m \right\rangle \hbar\delta(\hbar\omega + \varepsilon_m - \varepsilon_i)$$

$$= e^{-\beta\hbar\omega} S(\omega, \vec{\mathbf{k}})$$

Later we will show that $S(\omega, \vec{\mathbf{k}})$ also satisfies the following relation,

$$S(-\omega, \vec{\mathbf{k}}) = e^{-\beta\hbar\omega} S(\omega, \vec{\mathbf{k}}) \tag{2.30}$$

which, in combination with the detailed balance, indicates that $S(\omega, \vec{\mathbf{k}})$ is invariant under momentum inversion, $S(\omega, \vec{\mathbf{k}}) = S(\omega, -\vec{\mathbf{k}})$. It is a result of time reversal symmetry of our absorption problem. This means that in principle we will get same dynamical information if we perform momentum and energy analysis of nuclear decays.

So far, we have been assuming that there are only nuclear resonant isotopes in our many-body system, which is clear in the way the lattice Hamiltonian is written in Eq. (2.18). Under such assumption, the lattice dynamic information obtained is that of the whole lattice. However, this assumption is not necessary. If we let the index ν and μ run through only nuclear resonant isotopes and N be the total number of them, and add kinetic energy terms for non-resonant isotopes and other atomic species in Eq. (2.18), then all the relations still hold, only now the lattice dynamic quantities obtained are just those of the sublattice formed by resonant isotopes. We shall keep this in mind as we continue the discussion. This element (isotope) selectivity and hence the possible site selectivity is the unique and important feature of INRS.

2.5 Partial Phonon Density of States

The quantities obtained by moment sum rules are averaged properties of the dynamics of the lattice studied. In order to make full use of the whole spectrum measured we need to find a model of the particle correlation function $G_s(\vec{\mathbf{r}}, t)$ or the intermediate scattering function $F_s(\vec{\mathbf{k}}, t)$. From the model one calculates $S(\omega, \vec{\mathbf{k}})$ then compares it with the measurement. For an arbitrary system, $F_s(\vec{\mathbf{k}}, t)$ is difficult to calculate. But for most solids, the harmonic model is a good approximation, and we shall use this model to study vibrational dynamics of solids.

In the harmonic approximation, the Hamiltonian can be written as a collection of harmonic oscillators,

$$H = \sum_l \hbar\omega_l \, (\mathbf{b}_l^\dagger \mathbf{b}_l + \frac{1}{2}) \tag{2.31}$$

where $\mathbf{b}_l^\dagger$, $\mathbf{b}_l$ are the creation and annihilation operator of phonons, or normal modes l of collective vibrations. For a system lacking periodicity, e.g., for amorphous material, l is just an index without any physical significance, while for crystals, phonons are indexed with the branch number s and wave vector $\vec{\mathbf{q}}$. For harmonic crystals the nuclear displacements can be expressed in terms of phonon operators,

$$\vec{\mathbf{u}}_\nu(t) = \sum_{\vec{\mathbf{q}},s} \left(\frac{\hbar}{2M\tilde{N}\omega_s(\vec{\mathbf{q}})} \right)^{\frac{1}{2}} \vec{\epsilon}_s^{\,\nu} \left\{ \mathbf{b}_{\vec{\mathbf{q}},s} e^{i\left(\vec{\mathbf{q}}\vec{\mathbf{R}}_\nu - \omega_s(\vec{\mathbf{q}})t\right)} + \mathbf{b}_{\vec{\mathbf{q}},s}^\dagger e^{-i\left(\vec{\mathbf{q}}\vec{\mathbf{R}}_\nu - \omega_s(\vec{\mathbf{q}})t\right)} \right\} \tag{2.32}$$

where $\vec{\epsilon}_s^{\,\nu}$ is the polarization vector of phonon branch s at lattice site ν. It is the same for equivalent sites in a crystal. $\vec{\mathbf{R}}_\nu$ is the equilibrium position of ν-th nucleus and $\vec{\mathbf{r}}_\nu(t) = \vec{\mathbf{R}}_\nu + \vec{\mathbf{u}}_\nu(t)$. $\tilde{N}$ is the total number of all atoms in the lattice, which may be different from the number of nuclear resonant isotopes N.

Substituting Eq. (2.32) into (2.6), we have,

$$F_s(\vec{\mathbf{k}}, t) = \left\langle \frac{1}{N} \sum_\nu e^{-i\vec{\mathbf{k}}\vec{\mathbf{r}}_\nu(0)} e^{i\vec{\mathbf{k}}\vec{\mathbf{r}}_\nu(t)} \right\rangle_T = \frac{1}{N} \sum_\nu \left\langle e^{-i\vec{\mathbf{k}}\vec{\mathbf{u}}_\nu(0)} e^{i\vec{\mathbf{k}}\vec{\mathbf{u}}_\nu(t)} \right\rangle_T$$

since $\vec{\mathbf{R}}_\nu$ commutes with any $\vec{\mathbf{u}}_\mu(t)$, and we have changed the order of summation over all resonant nuclei and the thermal average. It can be verified that the commutator $\left[\vec{\mathbf{k}}\vec{\mathbf{u}}_\nu(0),\, \vec{\mathbf{k}}\vec{\mathbf{u}}_\nu(t)\right]$ is a c-number. By the operator identity $e^A e^B = e^{A+B} e^{\frac{1}{2}[A,B]}$, and Ott's theorem $\langle e^{iy} \rangle = e^{-\frac{1}{2}\langle y^2 \rangle}$, we have

$$\left\langle e^{-i\vec{\mathbf{k}}\vec{\mathbf{u}}_\nu(0)} e^{i\vec{\mathbf{k}}\vec{\mathbf{u}}_\nu(t)} \right\rangle_T$$

$$= exp\left\{ -\frac{1}{2} \left\langle \Big(-\vec{\mathbf{k}}\vec{\mathbf{u}}_\nu(0) + \vec{\mathbf{k}}\vec{\mathbf{u}}_\nu(t) \Big)^2 \right\rangle_T \right\} \times exp\left\{ \frac{1}{2} [-i\vec{\mathbf{k}}\vec{\mathbf{u}}_\nu(0),\, i\vec{\mathbf{k}}\vec{\mathbf{u}}_\nu(t)] \right\}$$

$$= exp\left\{-\frac{1}{2}\left\langle \left(\vec{\mathbf{k}}\vec{\mathbf{u}}_\nu(0)\right)^2 + \left(\vec{\mathbf{k}}\vec{\mathbf{u}}_\nu(t)\right)^2 - 2\left(\vec{\mathbf{k}}\vec{\mathbf{u}}_\nu(0)\right)\left(\vec{\mathbf{k}}\vec{\mathbf{u}}_\nu(t)\right)\right\rangle_T\right\} \tag{2.33}$$

where the three terms in the above expression can be evaluated by substituting the $\vec{\mathbf{u}}$'s by Eq. (2.32). The first two terms are found to be,

$$\left\langle [\vec{\mathbf{k}}\cdot\vec{\mathbf{u}}_\nu(0)][\vec{\mathbf{k}}\cdot\vec{\mathbf{u}}_\nu(0)]\right\rangle_T = \left\langle [\vec{\mathbf{k}}\cdot\vec{\mathbf{u}}_\nu(t)][\vec{\mathbf{k}}\cdot\vec{\mathbf{u}}_\nu(t)]\right\rangle_T$$

$$= \sum_{\vec{\mathbf{q}},s}\left(\frac{\hbar}{2M\tilde{N}\omega_s(\vec{\mathbf{q}})}\right)\left(\vec{\mathbf{k}}\cdot\vec{\epsilon}_s^{\,\nu}\right)^2\left\langle \mathbf{b}_{\vec{\mathbf{q}},s}\mathbf{b}^\dagger_{\vec{\mathbf{q}},s} + \mathbf{b}^\dagger_{\vec{\mathbf{q}},s}\mathbf{b}_{\vec{\mathbf{q}},s}\right\rangle_T$$

$$= \sum_{\vec{\mathbf{q}},s}\left(\frac{\hbar}{2M\tilde{N}\omega_s(\vec{\mathbf{q}})}\right)\left(\vec{\mathbf{k}}\cdot\vec{\epsilon}_s^{\,\nu}\right)^2\left(2n_{\vec{\mathbf{q}},s}+1\right)$$

$$= \sum_{\vec{\mathbf{q}},s}\left(\frac{\hbar}{2M\tilde{N}\omega_s(\vec{\mathbf{q}})}\right)\left(\vec{\mathbf{k}}\cdot\vec{\epsilon}_s^{\,\nu}\right)^2\coth\frac{\hbar\omega_s(\vec{\mathbf{q}})}{2k_BT} \quad \equiv \quad 2W_\nu \tag{2.34}$$

which is the recoilless factor for lattice site ν. It is similar to the Debye-Waller factor in X-ray diffraction. In the context of nuclear resonant scattering, it is called Lamb-Mössbauer factor. The difference is that Debye-Waller factor is for fast scattering process and is a function of momentum transfer, while Lamb-Mössbauer factor is for slow scattering process and is a function of the incident momentum. The occupation number is $n_{\vec{\mathbf{q}},s} = 1/(e^{\beta\hbar\omega_s}-1)$.

For the third term in the expression (2.33), let's define a

$$2M_{\nu\nu}(t) \quad \equiv \quad \left\langle [\vec{\mathbf{k}}\cdot\vec{\mathbf{u}}_\nu(0)][\vec{\mathbf{k}}\cdot\vec{\mathbf{u}}_\nu(t)]\right\rangle_T$$

$$= \sum_{\vec{\mathbf{q}},s}\left(\frac{\hbar}{2M\tilde{N}\omega_s(\vec{\mathbf{q}})}\right)\left(\vec{\mathbf{k}}\cdot\vec{\epsilon}_s^{\,\nu}\right)^2\left\{(n_{\vec{\mathbf{q}},s}+1)e^{i\omega_s(\vec{\mathbf{q}})t} + n_{\vec{\mathbf{q}},s}e^{-\omega_s(\vec{\mathbf{q}})t}\right\} \tag{2.35}$$

Notice that both W_ν and $M_{\nu\nu}(t)$ are functions of $\vec{\mathbf{k}}$ which is the incident photon momentum, instead of the momentum transfer in case of X-ray diffraction. Notice that $M_{\nu\nu}(0) = W_\nu$. Finally, we have

$$F_s(\vec{\mathbf{k}},t) = \frac{1}{N}\sum_\nu e^{-2W_\nu}\, e^{2M_{\nu\nu}(t)} \tag{2.36}$$

where the sum is over all resonant nuclei and the site dependency shows up through phonon polarization $\vec{\epsilon}_s^{\,\nu}$. In a crystal, equivalent sites share same polarization vector and we can separate the right hand side in above equation into sums of non-equivalent sites in a unit cell,

$$F_s(\vec{\mathbf{k}},t) = \sum_j p_j\, e^{-2W_j}\, e^{2M_{jj}(t)} \tag{2.37}$$

$$\sum_j p_j = \sum_j \frac{N_j}{N} = 1 \tag{2.38}$$

where p_j is the fraction of sites of type j of all the sites occupied by resonant nucleus in the unit cell.

We know that $F_s(\vec{\mathbf{k}}, t)$ is the Fourier transform of $S(\omega, \vec{\mathbf{k}})$. The particular form of $F_s(\vec{\mathbf{k}}, t)$ for Harmonic lattice (Eq.2.36) allows us to decompose $S(\omega, \vec{\mathbf{k}})$ by expanding the second exponential in $F_s(\vec{\mathbf{k}}, t)$. For the sake of simplicity, let's consider the case where the crystal is made of only the resonant isotopes and there is one atom per unit cell. Then the site dependency can be dropped. The more general situation can be easily recovered by reinstalling the sum. For the simple case, we have,

$$\begin{aligned}
\mathcal{F}\left\{S(\omega,\vec{\mathbf{k}})\right\} &= F_s(\vec{\mathbf{k}},t) &= e^{-2W}\, e^{2M(t)} \\
\mathcal{F}\left\{S_0(\omega,\vec{\mathbf{k}})\right\} &= F_s^{(0)}(\vec{\mathbf{k}},t) &= e^{-2W}\,[2M(t)]^0 &= e^{-2W} \equiv f \\
\mathcal{F}\left\{S_1(\omega,\vec{\mathbf{k}})\right\} &= F_s^{(1)}(\vec{\mathbf{k}},t) &= e^{-2W}\,[2M(t)] \\
\mathcal{F}\left\{S_n(\omega,\vec{\mathbf{k}})\right\} &= F_s^{(n)}(\vec{\mathbf{k}},t) &= e^{-2W}\,\frac{[2M(t)]^n}{n!}
\end{aligned}$$

from which we can derive the following recursive relations,

$$\mathcal{F}\left\{\frac{S_n(\omega,\vec{\mathbf{k}})}{f}\right\} = \frac{1}{n}\mathcal{F}\left\{\frac{S_{n-1}(\omega,\vec{\mathbf{k}})}{f}\right\}\ \mathcal{F}\left\{\frac{S_1(\omega,\vec{\mathbf{k}})}{f}\right\} \tag{2.39}$$

where $f = e^{-2W}$ is Lamb-Mössbauer factor. Then by reverse transform and convolution theorem for Fourier transform, we find the expressions for $S(\omega, \vec{\mathbf{k}})$,

$$S(\omega,\vec{\mathbf{k}}) = S_0(\omega,\vec{\mathbf{k}}) + S_1(\omega,\vec{\mathbf{k}}) + S_2(\omega,\vec{\mathbf{k}}) + \cdots \tag{2.40}$$

$$S_0(\omega,\vec{\mathbf{k}}) = f\,\delta(\omega) \tag{2.41}$$

$$S_1(\omega,\vec{\mathbf{k}}) = \frac{f}{2\pi}\int 2M(t)\, e^{-i\omega t}\, dt \tag{2.42}$$

$$S_n(\omega,\vec{\mathbf{k}}) = \frac{1}{n\,f}\int S_{n-1}(\omega-\omega',\vec{\mathbf{k}})\, S_1(\omega',\vec{\mathbf{k}})\, d\omega' \tag{2.43}$$

The meaning of these terms is very clear. The zero-th order term represents the elastic peak. The first order term is for the processes only involving single phonon during the nuclear excitation. The n-th order term represents the contribution involving n phonons. Substituting Eqs. (2.35) into (2.42),

$$\begin{aligned}
S_1(\omega,\vec{\mathbf{k}}) &= f\sum_{\vec{\mathbf{q}},s}\frac{\hbar(\vec{\mathbf{k}}\cdot\vec{\epsilon}_s)^2}{2M\tilde{N}\omega_s(\vec{\mathbf{q}})}\int\frac{dt}{2\pi}e^{-i\omega t}\left\{(n_{\vec{\mathbf{q}},s}+1)e^{i\omega_s(\vec{\mathbf{q}})t} + n_{\vec{\mathbf{q}},s}e^{-\omega_s(\vec{\mathbf{q}})t}\right\} \\
&= f\sum_{\vec{\mathbf{q}},s}\frac{\hbar(\vec{\mathbf{k}}\cdot\vec{\epsilon}_s)^2}{2M\tilde{N}\omega_s(\vec{\mathbf{q}})}\left\{(n_{\vec{\mathbf{q}},s}+1)\,\delta\Big(\omega-\omega_s(\vec{\mathbf{q}})\Big) + n_{\vec{\mathbf{q}},s}\,\delta\Big(\omega+\omega_s(\vec{\mathbf{q}})\Big)\right\}
\end{aligned}$$

which, for $E = \hbar\omega > 0$, reads

$$S_1(E, \vec{\mathbf{k}}) = \frac{f\, E_R}{E\,(1 - e^{-\beta E})} \frac{1}{\tilde{N}} \sum_{\vec{\mathbf{q}},s} (\hat{\mathbf{k}} \cdot \vec{\epsilon}_s)^2\, \delta\Big(E - E_s(\vec{\mathbf{q}})\Big) \tag{2.44}$$

while for $E = \hbar\omega < 0$,

$$S_1(E, \vec{\mathbf{k}}) = \frac{f\, E_R}{-E\,(e^{-\beta E} - 1)} \frac{1}{\tilde{N}} \sum_{\vec{\mathbf{q}},s} (\hat{\mathbf{k}} \cdot \vec{\epsilon}_s)^2\, \delta\Big(|E| - E_s(\vec{\mathbf{q}})\Big) \tag{2.45}$$

To demonstrate its meaning, let's consider a polycrystalline sample, for which the average over 4π solid angle results in phonon density of states,

$$\begin{aligned} S_1(E) &= \int \frac{d\Omega}{4\pi} S_1(E, \vec{\mathbf{k}}) = \frac{f\, E_R}{E\,(1 - e^{-\beta E})} \frac{1}{3\tilde{N}} \sum_{\vec{\mathbf{q}},s} \delta\Big(|E| - E_s(\vec{\mathbf{q}})\Big) \\ &= \frac{f\, E_R}{3E\,(1 - e^{-\beta E})}\, \mathcal{D}(|E|) \end{aligned} \tag{2.46}$$

where $\mathcal{D}(E)$ is phonon density of states per atomic volume per eV. This is also true for single crystals with cubic symmetry, since in such cases the lattice properties are isotropic. In general we define,

$$\mathcal{D}(E, \hat{\mathbf{k}}) = \frac{1}{\tilde{N}} \sum_{\vec{\mathbf{q}},s} (\hat{\mathbf{k}} \cdot \vec{\epsilon}_s)^2\, \delta\Big(E - E_s(\vec{\mathbf{q}})\Big) \tag{2.47}$$

as a projected, or weighted, density of states in the direction of incident beam. For an anisotropic single crystal it shows direction dependence. It is related to $S_1(E, \vec{\mathbf{k}})$ in the same way as in Eq. (2.46),

$$S_1(E, \vec{\mathbf{k}}) = \frac{f\, E_R}{E\,(1 - e^{-\beta E})}\, \mathcal{D}(|E|, \hat{\mathbf{k}}) \tag{2.48}$$

This is an important result telling us that from measured INRS spectrum we will be able to extract weighted vibrational density of states of resonant isotopes in a sample. For a polycrystalline sample or an isotropic sample with cubic symmetry, the exact phonon DOS is obtained as shown in Eq. (2.46).

With phonon density of states, the contribution from Sn-sublattice to the thermodynamics properties of the sample can be calculated. The phonon system can be represented as a grand canonical ensemble with zero chemical potential. The partition function for a phonon system is

$$Z = \prod_l \sum_n e^{-\beta\hbar\omega_l (n + \frac{1}{2})} = \prod_l \frac{e^{-\frac{1}{2}\beta\hbar\omega_l}}{1 - e^{-\beta\hbar\omega_l}} \tag{2.49}$$

where $\beta = 1/k_B T$. Then the free energy, vibrational entropy, and specific heat are,

$$F = -\frac{1}{\beta} \ln Z = \frac{1}{2} \sum_l \hbar\omega_l + \frac{1}{\beta} \sum_l ln(1 - e^{-\beta\hbar\omega_l}) \tag{2.50}$$

$$S = -\frac{\partial F}{\partial T} = k_B \beta \sum_l \frac{\hbar\omega_l}{e^{\beta\hbar\omega_l} - 1} - k_B \sum_l \ln(1 - e^{-\beta\hbar\omega_l}) \tag{2.51}$$

$$C_V = T \left(\frac{\partial S}{\partial T} \right)_V = +k_B \beta^2 \sum_l \frac{(\hbar\omega_l)^2 e^{-\beta\hbar\omega_l}}{(1 - e^{-\beta\hbar\omega_l})^2} \tag{2.52}$$

Now we can prove a property of $S(E, \vec{\mathbf{k}})$ similar to the detailed balance relation. In the above Eq. (2.48), replacing E by $-E$ and we have,

$$S_1(-E, \vec{\mathbf{k}}) = e^{-\beta E} \, S_1(E, \vec{\mathbf{k}})$$

It can be generalized to $S(E, \vec{\mathbf{k}})$ by virtue of the recursive relation (Eq. 2.43), so that it is held that,

$$S(-E, \vec{\mathbf{k}}) = e^{-\beta E} \, S(E, \vec{\mathbf{k}}) \tag{2.53}$$

Combining this with the condition of detailed balance (Eq. 2.29), we can show that the phonon excitation probability density function is symmetric in $\vec{\mathbf{k}}$,

$$S(E, -\vec{\mathbf{k}}) = S(E, \vec{\mathbf{k}}) \tag{2.54}$$

2.6 Non-Equivalent Sites

For the general case where there are nonequivalent sites in a crystal occupied by resonant isotopes, we shall rewrite Eqs. (2.40) – (2.43) in the sum of lattice sites.

$$S(\omega, \vec{\mathbf{k}}) = \sum_j p_j \, S^j(\omega, \vec{\mathbf{k}}) = \sum_j p_j \left\{ S_0^j(\omega, \vec{\mathbf{k}}) + S_1^j(\omega, \vec{\mathbf{k}}) + \cdots \right\} \tag{2.55}$$

$$S_0^j(\omega, \vec{\mathbf{k}}) = f_j \, \delta(\omega) \tag{2.56}$$

$$S_1^j(\omega, \vec{\mathbf{k}}) = \frac{f_j}{2\pi} \int 2M_{jj}(t) \, e^{-i\omega t} \, dt \tag{2.57}$$

$$S_n^j(\omega, \vec{\mathbf{k}}) = \frac{1}{n \, f_j} \int S_{n-1}^j(\omega - \omega', \vec{\mathbf{k}}) \, S_1^j(\omega', \vec{\mathbf{k}}) \, d\omega' \tag{2.58}$$

Eq. (2.47) and (2.48) are also generalized to

$$\mathcal{D}(E, \hat{\mathbf{k}}) = \sum_j p_j \, \mathcal{D}_j(E, \hat{\mathbf{k}}) \tag{2.59}$$

$$\mathcal{D}_j(E, \hat{\mathbf{k}}) = \frac{1}{\tilde{N}} \sum_{\vec{\mathbf{q}}, s} (\hat{\mathbf{k}} \cdot \vec{\epsilon}_s^{\,j})^2 \, \delta\Big(E - E_s(\vec{\mathbf{q}})\Big) \tag{2.60}$$

$$S_1^j(E, \vec{\mathbf{k}}) = \frac{f \, R}{E \, (1 - e^{-\beta E})} \, \mathcal{D}_j(|E|, \hat{\mathbf{k}}) \tag{2.61}$$

These relations can be used to simulate $S(\omega, \vec{\mathbf{k}})$, thus the measured INRS cross section, provided a model of partial phonon density of states (Eq. 2.60) is known. However, the inverse problem, i.e., extracting partial DOS from measured spectrum, is not always solvable. To show that, let's rewrite Eqs. (2.40) again by regrouping terms by the order of phonons.

$$S(\omega, \vec{\mathbf{k}}) = S_0(\omega, \vec{\mathbf{k}}) + S_1(\omega, \vec{\mathbf{k}}) + S_2(\omega, \vec{\mathbf{k}}) + \cdots \tag{2.62}$$

$$S_0(\omega, \vec{\mathbf{k}}) = \sum_j p_j \, S_0^j(\omega, \vec{\mathbf{k}}) = \sum_j p_j \, f_j \, \delta(\omega) \tag{2.63}$$

$$S_1(\omega, \vec{\mathbf{k}}) = \sum_j p_j \, S_1^j(\omega, \vec{\mathbf{k}}) = \sum_j p_j \, \frac{f_j}{2\pi} \int 2M_{jj}(t) \, e^{-i\omega t} \, dt \tag{2.64}$$

$$S_n(\omega, \vec{\mathbf{k}}) = \sum_j p_j \, S_n^j(\omega, \vec{\mathbf{k}}) = \sum_j p_j \, \frac{1}{n \, f_j} \int S_{n-1}^j(\omega - \omega', \vec{\mathbf{k}}) \, S_1^j(\omega', \vec{\mathbf{k}}) \, d\omega' \tag{2.65}$$

This set of equations reduce to Eqs. (2.40) – (2.43) when there is only one distinct site for resonant nuclei. With the help of Eqs. (2.59) – (2.61), we can show that the relation Eq. (2.48) still holds for the above defined $S_1(\omega, \vec{\mathbf{k}})$, which means that the single phonon contribution to $S(\omega, \vec{\mathbf{k}})$ is still directly proportional to the phonon density of states. However, for $S_n(\omega, \vec{\mathbf{k}})$ the recursive relation Eq. (2.43) does not hold any more when there are more than one distinct site. For such cases, $S_1(\omega, \vec{\mathbf{k}})$ can not be solved from $S(\omega, \vec{\mathbf{k}})$, since there are only n transcendental equations for $n \times m$ unknowns. Here n is the number of data points of the measured spectrum and m is the number of distinctive sites occupied by nuclear resonant isotopes.

Even though in general when there are non-equivalent sites, single phonon term cannot be separated, we can get around this difficulty under some special conditions. For example, by performing experiments at low temperature, multiple phonon contributions are reduced. When it comes to a point that these high order terms can be neglected, there are only two terms left, where $S_0(\omega, \vec{\mathbf{k}})$ is the average Lamb-Mössbauer factor and $S_1(\omega, \vec{\mathbf{k}})$ is proportional to phonon DOS. On the other hand, we might make the approximation that all sites have very similar phonon frequency distributions, thus simplify the problem to a single site problem. That means when facing a non-equivalent sites problem, we simply go ahead apply the algorithm described in the previous section and obtain a phonon density of states, but we must keep in mind that this is a rough average at the best. In the situation where we believe resonant isotopes occupy different sites which participate in different modes of vibrations, this procedure breaks down.

These results can be easily extended to a lattice without translational symmetry, where the displacement (Eq. 2.32) is replaced by

$$\vec{\mathbf{u}}_\nu(t) = \sum_l \left(\frac{\hbar}{2M\tilde{N}\omega_l} \right)^{\frac{1}{2}} \vec{\epsilon}_l^{\,\nu} \left\{ \mathbf{b}_l \, e^{-i\omega_l t} + \mathbf{b}_l^\dagger \, e^{+i\omega_l t} \right\} \tag{2.66}$$

by which we can show that all the equations derived so far hold, provided the phonon modes are labeled properly with index l instead of $(s, \vec{\mathbf{q}})$. In this case, every site becomes a non-equivalent site in principle, and the subscript j in Eq. (2.37) reduces to ν and p_j is just $1/N$. If nuclear resonant isotopes are more or less randomly distributed in the sample, we can only talk about an averaged vibrational frequency distribution, thus our algorithm can be applied and Eq (2.37) becomes,

$$F_s(\vec{\mathbf{k}}, t) = e^{-\overline{2W}}\, e^{\overline{2M}(t)} \tag{2.67}$$

Formally, this is the same as single site case.

2.7 Experimental Intensity

In this section we will calculate the intensity we can expect from an INRS experiment. Let's start with the INRS cross section (Eq. 2.11),

$$\sigma(E) = \frac{\pi}{2}\,\sigma_0 \Gamma\, S(E) \tag{2.68}$$

In the above expression, we have omitted the $\vec{\mathbf{k}}$ dependency. To avoid nonessential complication of mathematics, we will assume the following model for measured intensity,

$$I_m(E) = \eta \int dE'\, R(E' - E) \int_0^\infty I_0 n\sigma(E')\, e^{-(n\sigma(E') + \mu_\gamma) l}\, dl \tag{2.69}$$

where I_0 is the incident beam flux. $R(E)$ is the instrumentation resolution function, which is the energy resolution function of high resolution monochromator which will be discussed in next chapter. And n is the number density of nuclear resonant isotopes, l is the penetration depth of the incident beam, μ_γ is the electronic absorption coefficient of incident beam in the sample, and η is the detection efficiency which includes solid angle and detector efficiency for the fluorescences. What is assumed here is that all the nuclear resonant events contribute to measured intensity. Under such an assumption, the absorption of both nuclear and atomic fluorescences are neglected. It can be shown that, through slightly involved integrals, the incorporation of these absorptions result in a constant on the order of 1. Carrying out the integration of penetration depth l in the above equation, we have,

$$I_m(E) = \eta\, I_0 \int dE'\, R(E' - E)\, \frac{n\sigma(E')}{n\sigma(E') + \mu_\gamma} \tag{2.70}$$

According to Eq. (2.62), we can separate the phonon excitation probability density function $S(E)$ into elastic and inelastic (phonon) contributions.

$$S(E) = S_0(E) + S'(E) = f\,\delta(E) + S'(E) \tag{2.71}$$

where f is the average of site sum (see Eq. 2.63). The cross section can be separated in the same way, where the δ-function is replaced by Lorentzian resonance profile having a width of Γ,

$$\begin{aligned}\sigma(E) &= \frac{\pi}{2}\,\sigma_0\Gamma\,\left\{f\,\frac{\Gamma/2\pi}{E^2+\Gamma^2/4}+S'(E)\right\}\\ &= \sigma_0\Gamma\,\left\{f\,\frac{\Gamma/4}{E^2+\Gamma^2/4}+\frac{\pi}{2}S'(E)\right\}\end{aligned} \tag{2.72}$$

Thus, for $E=0$,

$$\sigma(E=0)=\sigma_0 f\sim 10^5\sigma_{\rm Thomson} \tag{2.73}$$

while an estimate for $E\neq 0$ is,

$$\overline{\sigma}(E\neq 0)=\frac{\pi}{2}\,\sigma_0\Gamma\,\overline{S'(E)}=\sigma_0\Gamma\,\frac{\pi}{2}\,\frac{1-f}{2\Theta_{\rm D}}\sim 10^{-7}\sigma_0\sim 10^{-1}\sigma_{\rm Thomson} \tag{2.74}$$

Meanwhile the electronic absorption coefficient can be written as $\mu_\gamma=n_{el}\sigma_{el}$, where σ_{el} is typically $10^3\sigma_{\rm Thomson}$, and n_{el} is the number density of all atoms in the sample. The ratio n/n_{el} is smaller than 1 and depends on chemical composition and isotope enrichment. From the above numbers, we conclude that elastic nuclear resonant scattering is much stronger than electronic absorption, and inelastic nuclear resonant scattering is much weaker than it.

Due to the significant difference between $\sigma(E=0)$ and $\sigma(E\neq 0)$, let's treat them separately. For $E\neq 0$,

$$\begin{aligned}I_m(E\neq 0) &= \eta\,I_0\,\int dE'\,R(E'-E)\,\frac{n\sigma(E')}{n\sigma(E')+\mu_\gamma}\\ &\approx \frac{\eta\,I_0\,n}{\mu_\gamma}\int dE'\,R(E'-E)\,\sigma(E')\end{aligned} \tag{2.75}$$

Besides the convolution with resolution function, the measured intensity is proportional to the INRS cross section for the whole spectrum except the elastic peak. For an estimate, let $R(E)=1/\Delta E$ for $|E|<\Delta E/2$ and otherwise vanishes. Then,

$$\overline{I_m}(E\neq 0) \;=\; \eta\,I_0\,\frac{n\sigma_0}{\mu_\gamma}\,\frac{\pi}{2}\,\frac{1-f}{2\Theta_{\rm D}}\Gamma \;\sim\; \eta\,I_0\,\times 10^{-5} \tag{2.76}$$

where we have assumed, for typical situations, that $n\sigma_0/\mu_\gamma\sim 10^3$, $f\sim 0.5$, $2\Theta_{\rm D}\sim 10^{-1}eV$, and $\Gamma\sim 10^{-9}eV$.

On the other hand, for $E=0$, we have,

$$I_m(E\sim 0) \;=\; \eta\,I_0\,\int dE'\,R(E'-E)\,\frac{n\sigma(E')}{n\sigma(E')+\mu_\gamma}$$

$$\begin{aligned} &\approx \quad \eta\, I_0 \int dE'\, R(E'-E)\, \frac{n\frac{\sigma_0 f\Gamma^2/4}{E'^2+\Gamma^2/4}}{n\frac{\sigma_0 f\Gamma^2/4}{E'^2+\Gamma^2/4}+\mu_\gamma} \\ &= \quad \eta\, I_0 \int dE'\, R(E'-E)\, \frac{n\sigma_0 f\Gamma^2/4\mu_\gamma}{E'^2+(n\sigma_0 f/\mu_\gamma+1)\Gamma^2/4} \end{aligned} \tag{2.77}$$

In the above equation, we can see the broadening of nuclear resonance, and this is in accord with the forming of nuclear exciton in the sample when elastic nuclear resonance occurs. With the above assumed instrumentation function $R(E)$, its range of being non-zero ($\sim meV$) is much wider than the width of the Lorentzian, thus we have,

$$\begin{aligned} I_m(E\sim 0) \quad &\approx \quad \frac{\eta\, I_0}{\Delta E}\int_{-\infty}^{\infty} dE'\, \frac{n\sigma_0 f\Gamma^2/4\mu_\gamma}{E'^2+(n\sigma_0 f/\mu_\gamma+1)\Gamma^2/4} \\ &= \quad \eta\, I_0\, \frac{\pi}{2}\left(\frac{n\sigma_0 f}{\mu_\gamma}\right)^{1/2} \frac{\Gamma}{\Delta E} \quad \sim \quad \eta\, I_0\, \times 10^{-4} \end{aligned} \tag{2.78}$$

Compare the measured intensity at elastic peak ($E=0$) and that at phonon part of the spectrum ($E\neq 0$), the former is about one order of magnitude larger than the latter. The same ratio in the cross section is on the order of 10^6. This enormous elastic peak suppression is the result of strong recoiless absorption, which causes only a very thin top layer of the sample contribute to elastic peak, while a much thicker portion of the sample contribute to the inelastic part of the spectrum. The penetration depth of incident X-rays with energy "off resonance" is essentially determined by electronic absorption. This can be demonstrated very clearly by the following estimation for a sample of enriched SnO. According to Eq. (2.73) the INRS cross section at exact nuclear transition energy is $3.8\times 10^5\, barn$, which corresponds to an absorption length of $0.9\ \mu m$. This is very small compared to the electronic absorption in the material with the absorption length of $134\ \mu m$. The cross section and absorption length for the inelastic part of the spectrum are $1\ barn$ and $0.34\times 10^6\ \mu m$ according to Eq. (2.74).

Now we can verify an assumption made earlier in deriving the cross section for INRS (see page 9). The assumption is that the resonant absorption of incident photons by individual nuclei are independent, or that, there is no multiple excitations simultaneously in the sample. At the third generation synchrotron sources, I_0 in the above estimations after a high resolution monochromator is on the order of 10^8 photons per second. With a filling pattern of 25 bunches in the storage ring, there are $1s/3.68\mu s\times 25\sim 10^7$ bursts of X-ray pulses per second. Here the revolution time of $3.68\mu s$ at APS is used. Thus the nuclear resonant events happen at a rate of less than 10^{-3} per pulse, and there is virtually no chance of multiphoton excitations. We have verified the assumption of independent absorption. However, for a much brighter source, as the planned X-ray FELs, the peak brilliance may be ten orders of magnitude higher than that of current storage rings. The independent absorption

assumption is not valid any more. The number of multiple excitations may be as high as 10000, and the beam is fully coherent over the entire beam cross section.

2.8 Normalization and Recoilless Fraction

In previous sections, we have calculated cross section for INRS, and explained how it is related to vibrational dynamics of sample. Next, let's consider data analysis procedure of an INRS experiment [12, 28, 29], particularly how to normalize the spectrum and extract lattice dynamic informations. In this section we do not write the $\vec{\mathbf{k}}$-dependence explicitly for the sake of simplicity. Since the measured flux is a convolution involving the normalized instrument resolution function $R(E)$,

$$I_m(E) = \int I(E')\, R(E - E')\, dE' \ , \tag{2.79}$$

we have the following relations for the moments of spectrum,

$$\langle I_m \rangle_0 = \langle I \rangle_0 \tag{2.80}$$
$$\langle I_m \rangle_1 = \langle I \rangle_1 + \langle I \rangle_0 \langle R \rangle_1 \tag{2.81}$$
$$\langle I_m \rangle_2 = \langle I \rangle_2 + 2\langle I \rangle_1 \langle R \rangle_1 + \langle I \rangle_0 \langle R \rangle_2 \tag{2.82}$$
$$\langle I_m \rangle_3 = \langle I \rangle_3 + 3\langle I \rangle_2 \langle R \rangle_1 + 3\langle I \rangle_1 \langle R \rangle_2 + \langle I \rangle_0 \langle R \rangle_3 \ , \tag{2.83}$$

where $\langle\ \rangle_{\rm n}$ denotes the n-th moment. Using these relations, the moments of $S(E)$ can be calculated from those of $I_{\rm m}(E)$ and $R(E)$, which are experimentally measured quantities.

From the discussion in last section, we understand that $I(E)$ is proportional to the INRS cross section except in the region of elastic peak, where it is severely suppressed. With the help of Eqs. (2.71) and (2.72), we can write $I(E)$ as,

$$I(E) = aS'(E) + bf\delta(E) \tag{2.84}$$

where $b/a \ll 1$ represents the peak suppression. Since the sum rules concern $S(E)$ rather than $S'(E)$, we will rewrite $I(E)$ as,

$$I(E) = A\, S(E) - B\, \delta(E) \tag{2.85}$$

where $A = a$ is the normalization factor and $B = (a - b)f$. Substituting this $I(E)$ into Eqs. (2.79) – (2.81), we find,

$$A = \frac{1}{E_R}(\langle I_m \rangle_1 - \langle I_m \rangle_0 \langle R \rangle_1) \tag{2.86}$$
$$B = \langle I_m \rangle_0 - A \tag{2.87}$$

As can be seen from the above expression (2.85) of $I(E)$, that except the zero-th moment, all other moments of $I(E)/A$ are equal to those of $S(E)$. Thus we are able

to use the sum rules (2.22) and (2.23) to calculate mean kinetic energy $\overline{T}$ and mean force constant $\overline{K}$ directly from measured spectrum. From the mean kinetic energy, we can also calculate the second order Doppler shift,

$$\delta_{\rm SOD} = -E_0 \frac{\langle v^2 \rangle}{2c^2} = -E_0 \frac{\overline{T}}{Mc^2} \tag{2.88}$$

For moments higher than the third one, the part of spectrum with large $|E|$ will dominate. Since the count rates at these regions of a spectrum (towards both ends of it) are low, the large statistical uncertainties obscure the values that can be calculated. So usually we do not calculate moments higher than the third one.

The f-factor can be calculated from Eqs. (2.71) and (2.84),

$$\begin{aligned} f &= 1 - \int S'(E)\, dE \quad = \quad 1 - \int \frac{I(E) - bf\delta(E)}{A}\, dE \\ &= 1 - \frac{1}{A}\int I'(E)\, dE \quad = \quad 1 - \frac{1}{A}\langle I' \rangle_0 \quad = \quad 1 - \frac{1}{A}\langle I'_m \rangle_0 \end{aligned} \tag{2.89}$$

where I'_m is the measured spectrum with elastic peak removed.

To remove elastic peak, first we fit the central peak with the instrument resolution function and the inelastic contribution under the elastic peak. Then the fitted resolution function is subtracted from data. The instrument resolution function is measured by nuclear forward scattering, in which the elastic resonance is enhanced coherently in forward direction so that the nuclear resonance acts as an extremely fine probe to measure the energy bandpass of the high resolution monochromator (see page 39). The inelastic contribution is complicated. In principle, all terms in Eq. (2.40) make contribution at $E = 0$, not just S_0. So we need a model to simulate the inelastic contribution in the vicinity of $E = 0$. In the close vicinity of the elastic peak, S_1 can be very well approximated by the Debye model,

$$S_1(E) = \frac{f\,R}{3E\,(1 - e^{-\beta E})}\, \mathcal{D}(|E|) \propto \frac{f\,R}{3E\,(1 - e^{-\beta E})}\, E^2 \propto (1 + \frac{\beta}{2}E) \tag{2.90}$$

for small $|E|$. If the single phonon term S_1 is the dominate one in the series, then we can fit the elastic peak with the sum of monochromator resolution function and the above approximation for inelastic contribution, and subtract from the data only the instrumentation resolution part.

The peak fitting is also important for combining several scan data sets into one spectrum. Usually for one sample, the spectrum is scanned repeatly many times, so that each scan can be completed in a short period of time for the reasons of X-ray beam and instrument, especially temperature, stabilities. To combine these data sets, we need to find the $E = 0$ point. If we have a distinguishable central peak, then it is fitted with the monochromator resolution function plus the inelastic contribution under the peak. Then the data is shifted in energy so that the elastic

peak is at exactly $E = 0$ in the new data set. Afterwards, all data sets are added up to improve statistics. Another way to find $E = 0$ is to monitor the forward scattering simultaneously, whose dominant elastic signal will indicate $E = 0$.

The f-factor and second order Doppler shift are important paramenters in Mössbauer spectroscopy. They can be obtained in Mössbauer transmission experiments, but with some complications. In such measurements, the f-factor is almost always tied to area density of resonant isotopes, which is very difficult to determine accurately. The sample geometry, its uniformity, and the isotope abundance all contribute to the determination of area density, and this causes a lot uncertainties of the value of f-factor obtained in such experiments. As a result, the absolute value of f is not very reliable and most times relative ratios are used to extract information. In studying local electronic environments of resonant nuclei, chemical isomer shifts are much desired numbers by Mössbauer spectroscopy. However, the isomer shift is always accompanied by second order Doppler shift. Inelastic nuclear resonant scattering provides a way to obtain second order Doppler shift independently, and obtain f-factor more precisely. A general discussion of f-factor and second order Doppler shift can be found in Ref. [29].

Chapter 3

Instrumentation and Experimental Setups

3.1 Experimental Setups

The experiments described in this thesis were all conducted at the Advanced Photon Source Sector 3-ID undulator beamline. The undulator is a 90 pole 2.7 cm period device optimized for 14.4 keV at first harmonic. For ^{119}Sn experiments, third harmonic has to be used with an undulator gap of 11.45 mm. The energy width of the 3rd harmonic is about 300 eV. The general layout of experimental setup is shown in Fig. 3.1. Following the undulator, there are water-cooled white beam slits, that have a horizontal opening of 3 mm and a vertical opening usually set at about 0.5 mm or less, which corresponds to a 18 μrad vertical angle from the source (the distance between the white beam slits and the center of the undulator is 28 m). The angular divergence of the undulator $3rd$ harmonic is about 15 μrad. A water-cooled diamond double-crystal monochromator is used as premonochromator, or high heat load monochromator as it is often called. For both diamond crystals, nearly-symmetric (1 1 1) reflection is used, which has a Bragg angle of 7.24° and theoretical Darwin width of 7.24 μrad at 23.880 keV X-ray energy. However, the measured beam divergence after two different sets of diamond crystals used at different times are about 12 and 9 μrad respectively. The measured X-ray beam energy bandwidth are about 3 and 2 eV. Usually there is a vertical slit before the high resolution monochromator to restrict the X-ray beam both spatially and angularly to no more than the high resolution monochromator can accept.

The high resolution monochromator crystals are mounted on high resolution rotation stages with adjustable height. They are placed on air pads to allow positioning in the horizontal plane. The crystals are placed on L-brackets which in turn are connected to the rotation axis. To minimize strain, the back of the crystals is attached to the holder by applying a thin layer of Vaseline. Nylon screws are used against the sides of crystals to restrict sliding motion. In case of channel-cut crystals, the monochromatized beam is parallel to the incident beam with a vertical offset. For two-crystal monochromator with different reflections, as those used in this ^{119}Sn work, the meV-beam is reflected away from the incident beam direction going backwards and up. So the sample and detector are placed upstream to the high resolution monochromator. Arrangements of sample and detector for both INRS and resolution function measurement are shown in Fig. 3.1.

For INRS experiments, detector is placed very close to the sample to cover as large

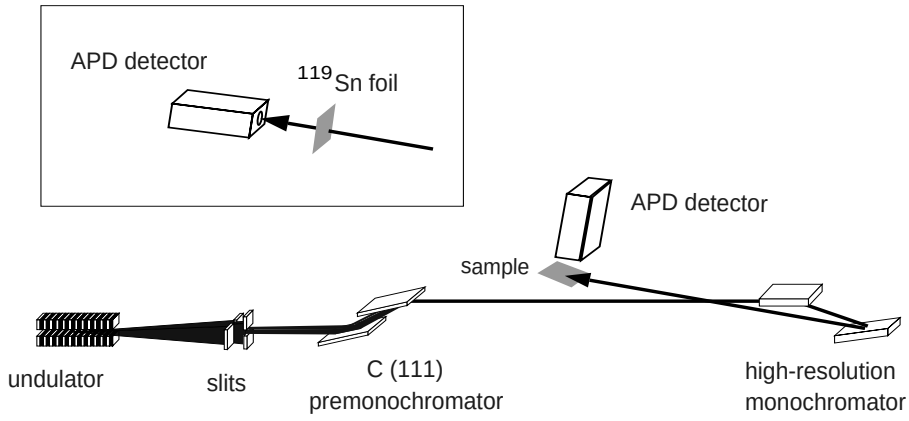

Figure 3.1: Experimental setup for INRS experiments and resolution measurement (inset).

a solid angle as possible. Avalanche Photodiode (APD) detectors are used because of their good time resolution and large dynamic range [8, 9, 10]. We use APDs from EG&G Optoelectronics Canada. The active region of silicon chip has a thickness of 100 μm. The active areas of the diodes we have used are 5×5 and 10×10 mm^2. The typical rise time is about 1 ns and the pulse lasts from a few ns to 10 ns.

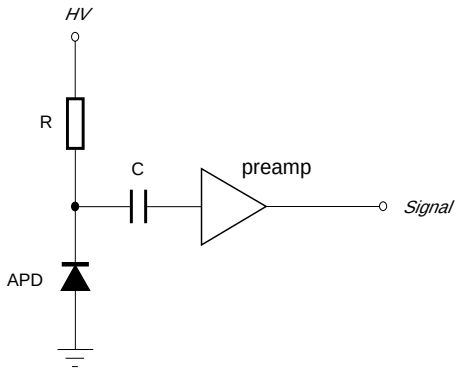

Figure 3.2: Schematics for APD detector.

The current amplifier is very important to the successful application of APD detectors. It needs to have high bandpass and low noise characteristics. The general scheme for such detector is shown in Fig. 3.2. The housing design for the diode and the preamp is equally crucial to avoid oscillation and reduce noise. Good contact and proper shielding are important. The off-the-shelf preamp from Phillips Scientific, model 6954, works reasonably well. However, some in-house designed preamps and

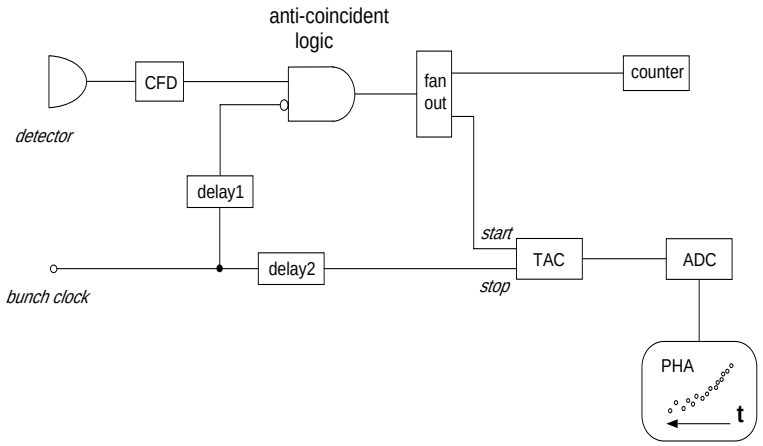

Figure 3.3: Schematics of electronic setup for timing. CFD: constant fraction discriminator, TAC: time to analog converter, ADC: analog to digital convertor, PHA: pulse height analyzer.

housing work better [30, 31].

As mentioned in the introduction, it is the characteristic nuclear decay time that makes it possible to separate weak nuclear resonant signals from the overwhelming electronic scattering. Compared to the nuclear resonant scattering intensities of Eqs. (2.78) and (2.76), the electronic scattering intensity is on the order of ηI_0, which can be five orders of magnitude larger. So, timing is a very important part of nuclear resonant scattering experiments. With a proper filling pattern of the storage ring, timing is achieved by employing fast NIM (Nuclear Instrument Module) electronics. The basic idea is to gate out prompt signals by fast anticoincident logic. To do that we need a timing signal which is synchronized with each bunch of electrons in the storage ring. Such bunch signal can be generated from the storage ring RF oscillators or from the injection to the storage ring. With proper delay, the bunch signal is set to coincide with the prompt signal from detector. Then through an anticoincident logic, the prompt signals are gated out. The diagram in Fig. 3.3 displays the basic electronic setup for timing.

3.2 Basic Principles of Crystal Monochromator

From previous discussions we understand that in order to measure phonon spectra, the radiation needs to be monochromatized into a bandwidth of a few meV or less. This requires the energy resolution $\delta E/E$ to be 10^{-7} or better at the nuclear resonant energy of ^{119}Sn. How do we achieve such a high degree of monochromatization? Not very long ago, X-rays were considered "a far less powerful probe of the phonon spec-

trum" (p. 480 in Ref. [32]) than neutron and light, mainly because of the difficulties in analyzing small energy change of X-rays. Crystal diffraction is usually employed to select a portion of radiation with particular energies. However, the mosaic nature of real crystals limits their resolving power. The development in crystal growing techniques and the demand of high purity crystals from semiconductor industry have substantially improved the crystal quality. Today, it is not too difficult to get so called "perfect crystals" — the high purity silicon single crystals[1]. The availability of such crystals not only revived the interest in the dynamical theory of X-ray diffraction, but also provides necessary materials for optics used at synchrotron radiation facilities. According to dynamical theory calculations, a spectral resolving power of 10^{-7} at about 24 keV can be achieved with certain choices of silicon crystal reflections.

The fundamental principle of monochromatization by crystal diffraction is Bragg's law,

$$\lambda = 2d \sin\theta \tag{3.1}$$

where d is the interplanar spacing of the crystallographic planes with Miller index (h k l). It describes the relationship between the wavelength of the radiation (or the energy) and the so called Bragg angle of the diffraction of order (h k l). Bragg's law can be derived by calculating the interference of the scattering of plane waves from a periodic array of atoms, where it is assumed that each atom sees the incident or the primary wave only. This treatment is called the kinematical theory. It neglects absorption and multiple scattering and does not allow extinction, thus violates the conservation of energy [33]. It can be regarded as an approximation for small crystals. Nevertheless, Bragg's law holds very nicely, needing correction to θ only on the order of μrad.

The dynamical diffraction theory takes a more realistic view of large prefect crystal. It treats the crystal as a medium with periodic, complex dielectric constant, and solves the Maxwell equations in the medium with proper boundary conditions [34, 35, 36, 37, 38, 39, 40, 41, 42]. Thus it includes absorption, multiple scattering, and extinction naturally. The dynamical theory of diffraction describes the perfect crystal optics used at various synchrotron radiation facilities quite satisfactorily. Concerning crystal monochromator, the relevant dynamical theory results are the refractive index correction to the Bragg angle, the Darwin width, the reflectivity, and the effects of asymmetric diffraction. A collection of formulas and the methods used in designing monochromators can be found in Ref. [43, 44]. Crystal diffraction can be classified geometrically into the Bragg case, where the incident and the reflected

[1]For example, those used to make the monochromators described in this chapter. One silicon boule, purchased from Wacker, is a 38.4 cm long cylinder with a diameter of 10 cm. It is grown by the floating zone technique in (1 1 1) orientation. The transverse resistivity at the seed end is 3490 Ω-cm, and 17.52 Ω-cm at the opposite end. A portion of it is used to make the (4 0 0) flat crystal described later.

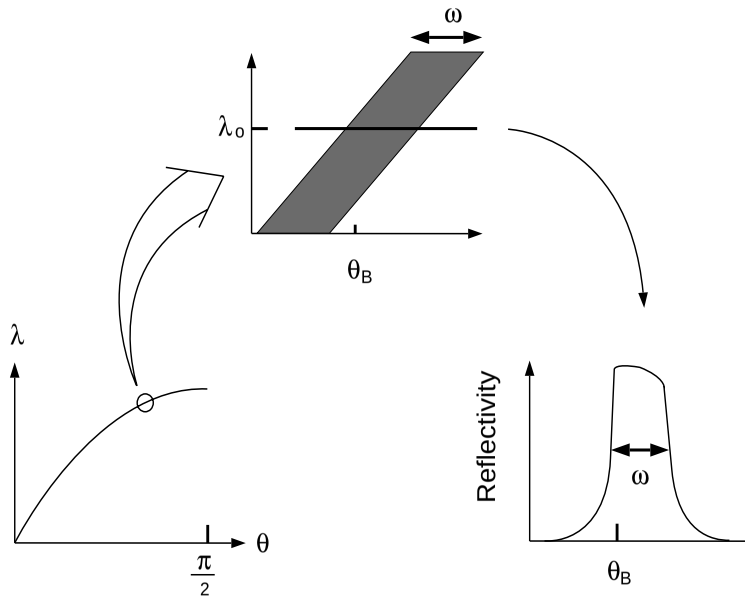

Figure 3.4: An illustration of diffraction from both the kinematical and dynamical theory's point of view. θ_B is the Bragg angle at wavelength λ_o, i.e., $\lambda_0 = 2d \sin\theta_B$. Notice that in dynamical theory, the center of Darwin curve (the reflectivity curve) is not θ_B. The difference is on the order of μrad. The Darwin width is shown as ω.

beams enter and exit through same surface, and the Laue case, where the reflected beam goes through the crystal and comes out from the other side of the crystal. Here we only consider Bragg geometry. An illustration of the refractive index correction and the Darwin width is shown in Fig. 3.4, while Fig. 3.8 shows the geometry of an asymmetric diffraction.

Taking the width of a crystal reflection into account, the energy resolution we will be able to get with a single crystal reflection is

$$\left|\frac{\Delta E}{E}\right| = \frac{\Delta\lambda}{\lambda} = (\Delta\theta + \omega)\cot\theta \tag{3.2}$$

where ω is the Darwin width or the angular acceptance of the reflection, and $\Delta\theta$ is the angular divergence of the incident beam, which, for example, can be defined by a slit. Eq. (3.2) suggests that in order to achieve high energy resolution, it is necessary to use high order reflection (i.e., large Bragg angle, thus smaller $\cot\theta$). But high order reflection will also cause other effects. One is that the Darwin width ω has a strong dependence on Bragg angle (e.g., see Fig. 3.6 and Fig. 3.7). The change in width by going to higher order reflection will change energy resolution slightly according to Eq. (3.2), but it will have significant effect on the X-ray flux being reflected within the

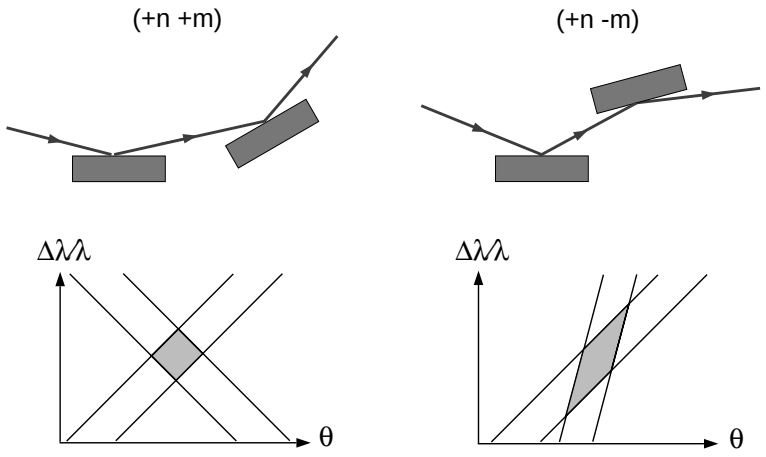

Figure 3.5: The relative geometries of two crystal reflections, along with their respective DuMond diagrams. The angle between the second and the first crystal $\theta_{12} = \theta_{\rm B}^{(1)} + \theta_{\rm B}^{(2)}$ for $(++)$ geometry and $\theta_{12} = \theta_{\rm B}^{(1)} - \theta_{\rm B}^{(2)}$ for $(+-)$ geometry.

energy bandwidth. The other effect is that the reflectivity for higher order reflection is lower, and that will reduce the flux throughput. The tradeoff between resolution and flux is one of the many unavoidable ones in the designing of crystal monochromators. Another one, for example, is between the matching of angular acceptances and X-ray beam size. The angular width can be manipulated by asymmetric diffraction, but that will also change beam size, which is a practical concern in the designing of monochromators and sometimes in their applications. Instead of a slit, a preceding crystal can be used to provide a limited angular range $\Delta\theta$. Usually, the two crystals need to be placed in the $(++)$ reflection geometry (Fig 3.5).

Since the Darwin width plays a very important role in perfect crystal optics, we will say more about it. The intrinsic Darwin width, which is defined as the angular range within which the reflectivity is unity in the zero-absorption approximation, is given by

$$\omega = \frac{2}{\sin 2\theta_B} \frac{r_e \lambda^2}{\pi V} C |F_{hkl}| e^{-W} \tag{3.3}$$

where λ is the incident X-ray wavelength, θ_B the corresponding Bragg angle of the reflection (h k l), $r_e = e^2/m_e c^2$ is the classical radius of electron, V is the unit cell volume, $C = 1$ for σ polarization and $C = |\cos 2\theta_B|$ for π polarization, $F_{hkl} = S_{hkl} \times (f_0 + f')$, and S_{hkl} is the crystal structure factor, f_0, f' are the atomic scattering factor and the real part of its dispersion correction, e^{-W} is square root of the Debye-Waller factor.

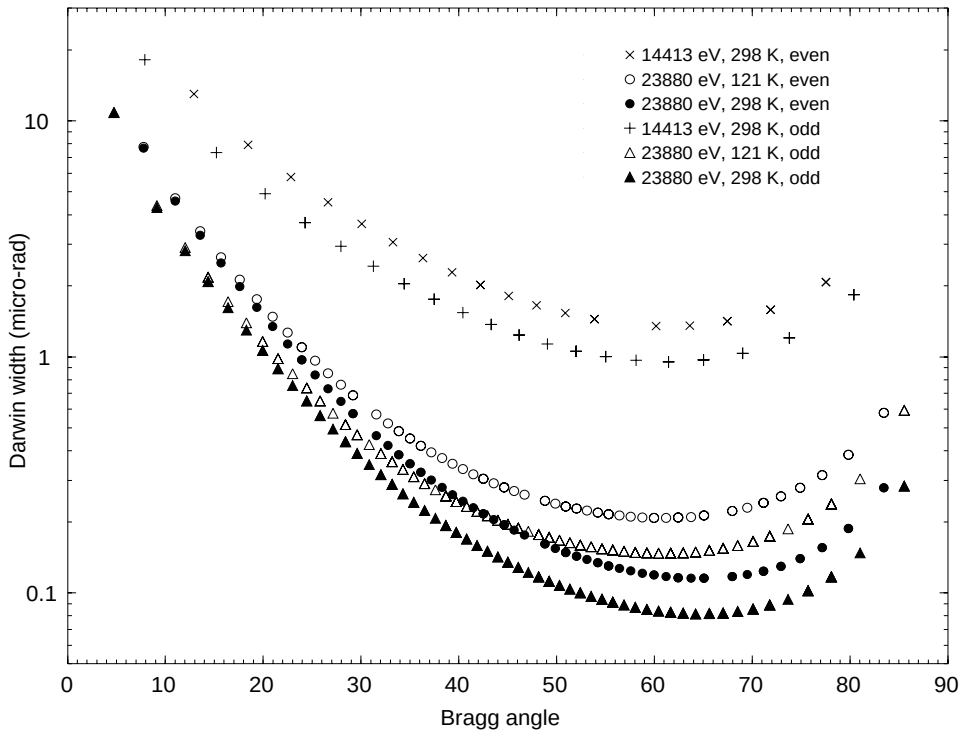

Figure 3.6: The intrinsic Darwin width for σ-polarized incident X-ray. In the legends, "even" and "odd" refer to even reflections (the Miller indices are all even numbers) and odd reflections (the Miller indices are all odd numbers).

The dependence of ω on Bragg angle, thus on the order of reflection, is a crucial factor in choosing proper reflections for a monochromator. The width also depends on X-ray energy, its polarization, the crystal structure, and the temperature of crystal. For silicon crystal, we have plotted the intrinsic Darwin widths in Fig. 3.6 and Fig. 3.7 for two different energies, 23880 eV and 14413 eV (the nuclear resonant energies for ^{119}Sn and ^{57}Fe respectively), at two temperatures, 298 K and 121 K. There are a couple of observations we can make from these figures which are true in general. First of all, for higher energy the Darwin widths are lower at comparable Bragg angles. Second, lowering temperature will increase the width more noticeably for high order reflections. Third, the even-order reflections generally have larger widths. This is because of that silicon has the diamond type structure and its geometric structure factor S_{hkl} is equal to 8 for even reflections and $4(1+i)$ for odd ones. For the very

same reason, the even reflections also have relatively higher reflectivities. The fourth interesting point is that for both σ- and π-polarized beams the width decreases to a minimum as the Bragg angle increases before it increases again as the Bragg angle approaches 90°. The temperature dependence of the intrinsic Darwin width can be evaluated from Eq. (3.3),

$$\frac{\Delta\omega}{\omega} = \left[-\alpha(2+\tan^2\theta_{\rm B}) - W(2\alpha - \frac{x}{T})\right]\Delta T \tag{3.4}$$

where

$$x = \begin{cases} \dfrac{3.2898}{\dfrac{y^2}{4}+1.6449} & for \quad y=\dfrac{\Theta_{\rm D}}{T} > 4.18 \\ \dfrac{1-\dfrac{y^2}{36}+\dfrac{y^4}{1200}}{1+\dfrac{y^2}{36}-\dfrac{y^4}{3600}} & for \quad y=\dfrac{\Theta_{\rm D}}{T} < 4.18 \end{cases}$$

$\Theta_{\rm D}$ is the Debye temperature of the crystal, which for silicon is 543 K [45], and α is the linear thermal expansion coefficient[2]. In above derivation, we use the following approximation for Debye-Waller factor in a harmonic model,

$$W = 3\,\frac{\hbar^2k^2/2m}{k_B\Theta_{\rm D}}\,\frac{T}{\Theta_{\rm D}}\,\Phi(y) \tag{3.5}$$

where

$$\Phi(y) = \begin{cases} \dfrac{y}{4}+\dfrac{1.645}{y} & for \quad y=\dfrac{\Theta_{\rm D}}{T} > 4.18 \\ 1+\dfrac{y^2}{36}-\dfrac{y^4}{3600} & for \quad y=\dfrac{\Theta_{\rm D}}{T} < 4.18 \end{cases}$$

For silicon at room temperature, $\alpha = 2.56\times10^{-6}K^{-1}$ [47]. At 23880 eV X-ray energy, room temperature, for silicon reflection (4 0 0) ($\theta_{\rm B} = 11.02°$), $\Delta\omega/\omega = -1.77\times10^{-4}\Delta T$; for (12 12 12) reflection ($\theta_{\rm B} = 83.48°$), $\Delta\omega/\omega = -4.85\times10^{-3}\Delta T$. These numbers demonstrate that the Darwin width is not sensitive to small temperature variations.

As mentioned before, the intrinsic width can be changed by asymmetric diffraction. The concept of asymmetric diffraction is shown in Fig. 3.8. The asymmetry angle, α, is the angle between crystal surface and the diffracting crystallographic

[2]An empirical formula of α for Si in the temperature range 120 K to 1500 K can be found in Ref. [46].

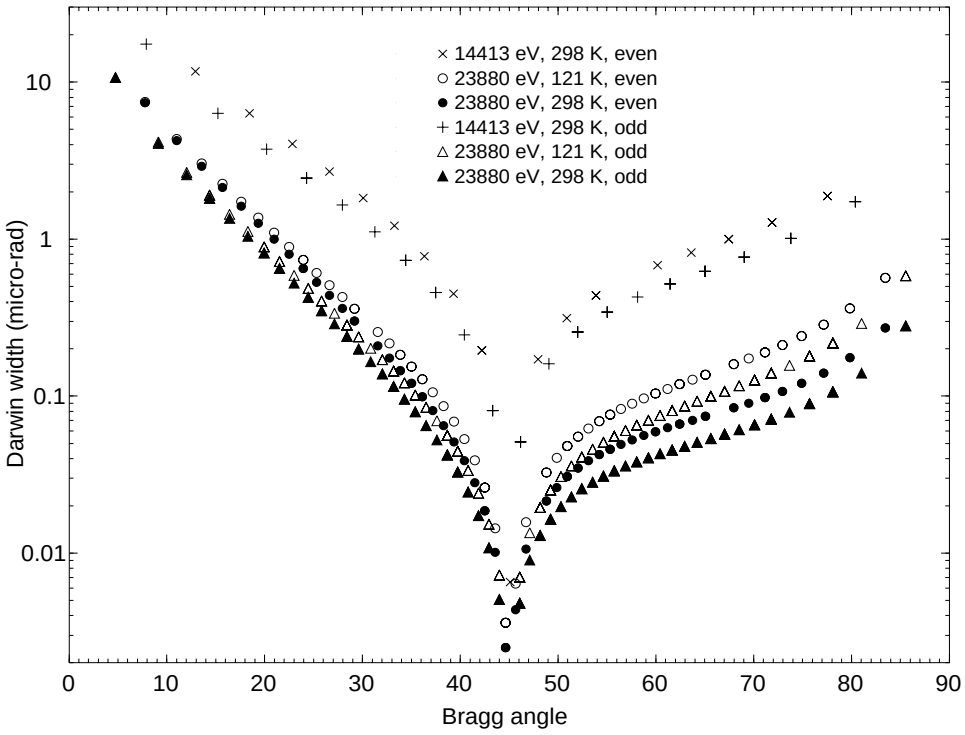

Figure 3.7: The intrinsic Darwin width for π-polarized incident X-ray. In the legends, "even" and "odd" refer to even reflections (the Miller indices are all even numbers) and odd reflections (the Miller indices are all odd numbers).

planes. It is defined in such a way that $\theta_B + \alpha$ is the incident angle of X-ray. The angular acceptance ω_o to the incident beam and angular divergence ω_h of the diffracted beam are changed from the intrinsic Darwin width ω by

$$\omega_o = \frac{\omega}{\sqrt{b}} \tag{3.6}$$

$$\omega_h = \omega\sqrt{b} \tag{3.7}$$

where b is the asymmetry factor defined as following

$$b = \frac{\sin(\theta_B + \alpha)}{\sin(\theta_B - \alpha)} \tag{3.8}$$

By simple geometry argument we can find the relation between the sizes of incident

and reflected beams,

$$S_h = S_o/b \tag{3.9}$$

From the above equations, we can verify the relationship between angular divergences and the beam sizes for the incident and diffracted X-ray beams,

$$\omega_h S_h = \omega_o S_o \tag{3.10}$$

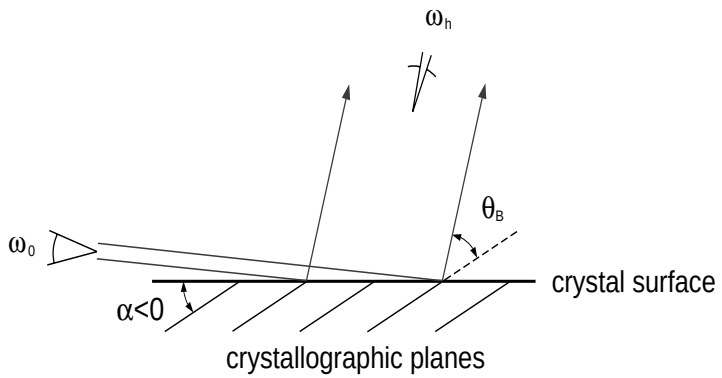

Figure 3.8: Asymmetric diffraction for a mono-energetic X-ray beam.

Transmission of X-rays through a series of crystals can be described by a graphic method called the DuMond diagram [48]. It is a two dimensional energy–angle space representation of the X-ray beam anywhere along the path through a series of crystals. It plots $\Delta\lambda/\lambda$ vs. $\theta - \theta_{\rm B}$, using the linearized Bragg's law,

$$\frac{\Delta\lambda}{\lambda} = \Delta\theta \, \cot\theta_{\rm B} \, , \tag{3.11}$$

since the angular range of such plots is usually in μrads or tens of μrads. The allowed energy–angle space region for an X-ray beam to be reflected by a crystal is a stripe with a width of ω in the θ-direction, which resembles the expanded diagram in figure 3.4. At the incident beam side of the crystal, the Darwin width $\omega = \omega_o$, while at the reflected beam side, $\omega = \omega_h$. The DuMond diagram between two crystals has two overlaid stripes representing the reflected beam of the first crystal and the incident beam of the second one, Fig. 3.5 has two examples. By the correspondence of the DuMond diagrams before and after a crystal, a DuMond diagram at any point in the system can be projected into a diagram at a different point. In such manner, we can project all the crystal reflections into a single DuMond diagram at any point along a series of crystals. In this diagram the common area of all stripes represents the part of energy–angle space of an X-ray beam that will be reflected through all these crystals, i.e., it represents the beam transmitted through the system.

In theory, the behavior of an X-ray beam through an optical system should be studied in its full phase space as discussed in Ref. [43, 44]. However, at a third-generation synchrotron radiation facility, X-ray beams from an insertion device are highly collimated in both vertical and horizontal directions. So, it is usually sufficient to treat the problem in the reflecting plane only, which often is the vertical plane. The characteristics of a monochromator can be shown in its reflectivity profile in λ–θ space, where we are concerned only with the vertical angle and energy of the X-rays. This is an approximation to the full phase-space approach [43, 44]. It is justified due to the very small horizontal divergence of the X-ray beam from an undulator. The change of Bragg angle for the X-ray having a small horizontal angle of α from the center of the beam is

$$\Delta\theta_B = -\frac{\alpha^2}{2}\tan\theta_B \tag{3.12}$$

At the beamline where the later on described monochromators are designed for, the horizontal divergence is about 40 μrad. Thus $\alpha = 2 \times 10^{-5}$, and $\Delta\theta_B$ is on the order of 10^{-10} which is quite negligible on the scale of μrad. So the horizontal divergence is not a concern and we will discuss characteristics of monochromators only in the energy – vertical angle space. In the following discussions, we also assume that the crystals are large enough or the X-ray beam is slit down so that the location of beam hitting the crystal does not matter. These assumptions allow us to discuss monochromator in terms of only two variables, angle and energy. A thorough study of flat crystal monochromators can be found in Ref. [44].

3.3 High Resolution Monochromator for 24 keV X-rays

After the first observation of nuclear resonant scattering of ^{57}Fe using synchrotron radiation, attempt has been made to extend the study to ^{119}Sn. A nested channel-cut monochromator for ^{119}Sn was reported [7] which used Si(3 3 3) and Si(5 5 5) reflections and had an energy resolution of 23 meV with an angular acceptance of 7 μrad. It was used in the first observation of the ^{119}Sn nuclear resonance in a nuclear forward scattering experiment with synchrotron source [15]. The main purpose of a monochromator in such cases is to reduce the energy bandwidth of incident X-ray beam to improve the signal-to-noise ratio. In order to study inelastic nuclear resonant scattering, a higher energy resolution is needed since the phonon features are typically on the scale of meV.

To achieve high energy resolution, we ought to use the highest order reflection possible in silicon. Table 3.1 lists four such reflections for 23.880 keV, the X-ray energy of ^{119}Sn resonance. Even though the largest Bragg angle is 85.55° associated with two odd-order reflections, we choose to use (12 12 12) because it has the same Darwin width but higher reflectivity due to the fact that it is an even-order reflection.

Table 3.1: The four highest order reflections for 23.880 keV X-rays in silicon at room temperature. The intrinsic Darwin width ω and reflectivity are listed for σ-polarized beam only.

reflection	θ_B	$\omega(\mu rad)$	$reflectivity$	$\cot\theta_B$
(12 12 12) or (20 4 4)	83.48°	0.28	0.754	0.114
(17 11 5) or (19 7 5)	85.55°	0.28	0.667	0.0778

It has the additional benefit of being in an easy to find orientation (1 1 1). However, it should be noted that the energy resolution will be about 46% wider from the $\cot\theta_B$ term. In the first attempt to achieve a few meV resolution at this energy, the flux throughput is also an important consideration. With the choice of (12 12 12) over (19 7 5) for example, the spectral flux is about 14% higher due to the difference in reflectivities.

The difficulties in making high resolution monochromators for X-rays with energy above 20 keV are rooted in the narrow angular acceptances of high order reflections. This is evident from the numbers in Table 3.1. Even though the narrow angular acceptance is advantageous in terms of energy resolution, it limits the transmitted X-ray intensity and may prevent any practical use of the monochromator. The small angular acceptance has two adverse effects. One is just that the crystal may not accept the full beam. The narrow angular acceptance also puts stringent requirements on mechanical control and temperature stability. With one (12 12 12) reflection alone, the energy resolution is about 42 meV according to Eq. (3.2) where an incident beam divergence of 15 μrad is assumed. This was the initial estimate of the vertical beam divergence at APS 3-ID undulator beamline with the high-heat-load monochromator crystals used at the time the first milli-eV monochromator at 23.880 keV was designed. To use a slit to reduce the beam divergence from 15 μrad to about the size of the angular acceptance of 0.3 μrad of the crystal is too inefficient in terms of flux.

Here we can employ the principle of asymmetric diffraction to overcome this severe mismatch between the incident beam divergence and the angular acceptance of high order reflection. We know that an asymmetrically diffracting crystal with the asymmetric factor b smaller than one ($\alpha < 0$ in Fig. 3.8) will have larger acceptance ω_o and smaller divergence ω_h (see Eqs. (3.6) and (3.7)). So we can add a second crystal placed before the high order reflection crystal to "funnel" the more divergent incident beam into a smaller angular range. Its order of reflection and asymmetry factor b are chosen so that its ω_o and ω_h match the incident beam divergence and the angular acceptance of the high order reflection respectively.

The energy resolution of a monochromator is measured by nuclear forward scat-

tering. The experimental setup is shown in the insert of Fig. 3.1. The undulator produces an x-ray beam with a broad energy spectrum and a high power density. A water-cooled diamond (1 1 1) premonochromator is used to reduce the bandwidth to 2.6 eV centered around 23.880 keV. The sample is a tin metal foil about 180μm thick and is 95% enriched in ^{119}Sn. An avalanche photodiode (APD) detector is used because of its nanosecond time resolution and large dynamic range [8, 9, 10]. It is placed behind the sample to measure the coherent nuclear forward scattering of 23.880 keV X-rays. Timing is employed to look for delayed nuclear resonant events only. The delayed counts are integrated in a time window of about 25 ns to 85 ns after the synchrotron x-ray pulse. The tin foil is placed perpendicular to the beam. The distance between the sample and the detector is sufficient to avoid signals due to incoherent nuclear resonant scattering. In this setup, essentially no delayed transmission occurs if the incident x-ray energy is off resonance. When the x-ray energy is on resonance, the elastic nuclear scattering from the sample is coherently enhanced in the forward direction. Thus the energy response of the sample in the forward direction, as seen by the detector, has a width on the order of the resonant linewidth, which is 25.5 neV. On the scale of meV, this narrow width acts like a very fine and fixed energy probe and permits very accurate measurement of the monochromator resolution. The energy of the x-ray beam that passes through the monochromator is determined by the angles of the crystals by

$$\frac{\delta E}{E_0} = \frac{\delta\theta_1 - \delta\theta_2}{\tan\theta_{\rm B1} + \tan\theta_{\rm B2}} \tag{3.13}$$

for the (++) geometry. The resolution function of the monochromator is then measured by scanning the crystal energy, i.e., rotating the second crystal relative to the first one. Such measured energy response function of the monochromator is actually its resolution function with the energy scale reversed, as can be seen from the following equation,

$$R_{\rm m}(\epsilon) = \int \delta(\epsilon') R(\epsilon' - \epsilon) d\epsilon' = R(-\epsilon) \tag{3.14}$$

where the δ-function represents the narrow nuclear resonance.

3.4 A 3.6-meV Monochromator for ^{119}Sn

For the first attempt[3], we have chosen (4 0 0) with $b = 0.1$. The parameters of this two-crystal monochromator are listed in Table 3.2. With a modest asymmetry angle, $\alpha = -8.9°$, it matches the assumed incident beam divergence fairly well, but does not quite match the acceptance of (12 12 12). Its resolution can be estimated to be 4.9 meV under the assumption of a widely divergent beam, that is, the incident beam

[3]A description of this monochromator is published as Ref. [49].

Table 3.2: The parameters for the 3.6-meV monochromator.

reflection	θ_B	α	b	$\omega_o(\mu rad)$	$\omega_h(\mu rad)$
(4 0 0)	11.02°	-8.9°	0.108	13.9	1.50
(12 12 12)	83.48°	70.53°	1.96	0.20	0.39

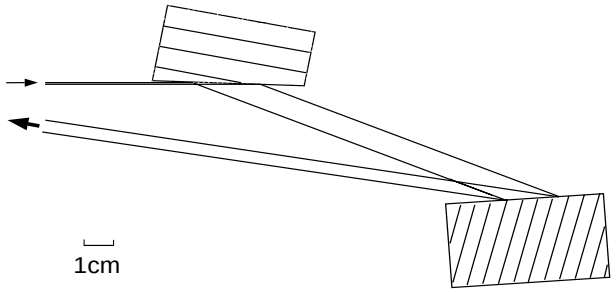

Figure 3.9: The schematic of a 3.6 meV two-crystal monochromator for 23.880 keV X-rays with reflections Si(4 0 0) – (12 12 12). For a list of parameters see Table 3.2.

has a uniform distribution in the interested region in λ–θ space. Later we will see that the actual resolution also strongly depends on the profile of the incident beam in λ–θ space.

A point worth noting is that the (12 12 12) reflection is also diffracting asymmetrically with $b > 1$. For the purpose of matching the angular widthes, its factor b should also be made smaller than one so that there is even better match between the two reflections. However, as mentioned before, accompanying the changes in angular width an asymmetric diffraction also alters the beam sizes. With $b = 0.1$ for the first reflection, the beam after the first reflection will be ten times as large as the incident beam. The typical incident beam size is about 0.5 to 1 mm. In many experiments samples cannot be made very large, or detector is not large enough or it has to be put very close to the sample, and sometimes grazing incidence is used especially for thin film experiments. So we want to keep the beam size small and choose $b > 1$ for (12 12 12) to partially compensate the beam enlargement caused by the first asymmetric diffraction.

The schematic of this two-crystal monochromator is shown in Fig. 3.9. The final exiting beam from this monochromator has a vertical size five times that of the incident beam and is going backwards with an angle of 9° from the horizontal plane.

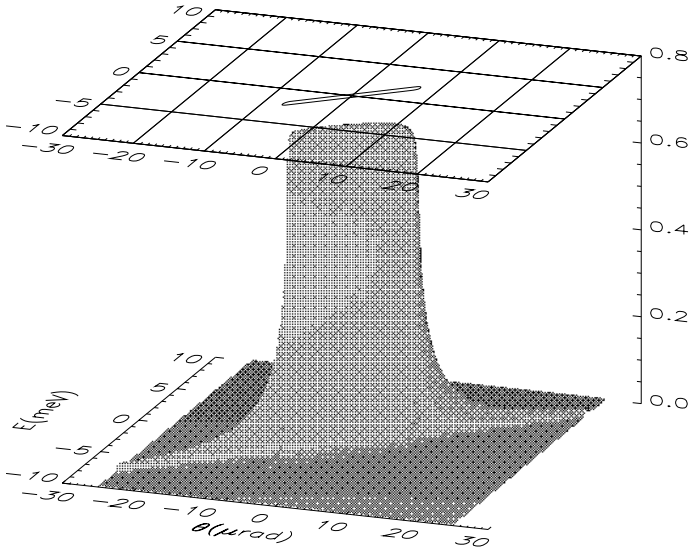

Figure 3.10: The calculated transmission function of the monochromator Si(4 0 0) – (12 12 12). The peak reflectivity is 0.734 and the contour is drawn at half the maximum reflectivity.

In comparison to a channel-cut design [7, 50], which preserves the beam direction and size, this might cause inconvenience in sample and detector positioning. However, this two-crystal design avoids the losses from two more reflections in a channel-cut design, and does not suffer from the adverse effect of temperature differences between the reflecting surfaces of channel-cut crystals.

As discussed before, the characteristics of a monochromator can be shown in its reflectivity profile in λ–θ space. In Fig. 3.10 it is shown for this monochromator the reflectivity as a function of vertical angle and energy. The angles shown in the figure are those on the incident side of the (4 0 0) reflection. The contour plot on the top is similar to the DuMond diagram at this incident face of (4 0 0). From the figure we can clearly see the mismatch between the widths of these two reflections. The slender stripe is for the (12 12 12) and its width is significantly smaller than the total expand of the contour in angle which is basically determined by the width of the (4 0 0) reflection.

The result of the resolution measurement is presented in Fig. 3.11 along with a simulation. The energy resolution is determined to be the full width at half maximum (FWHM) of the measured energy response function, which is 3.6 meV. The simulation is done by combining the transmission function of the monochromator (Fig. 3.10) and an incident beam profile in the λ–θ space. Here the incident beam is assumed to have a Gaussian vertical angular profile of 12 μrad FWHM, which is the measured angular divergence. The measurement uses two Si(11 11 11) channel-cut

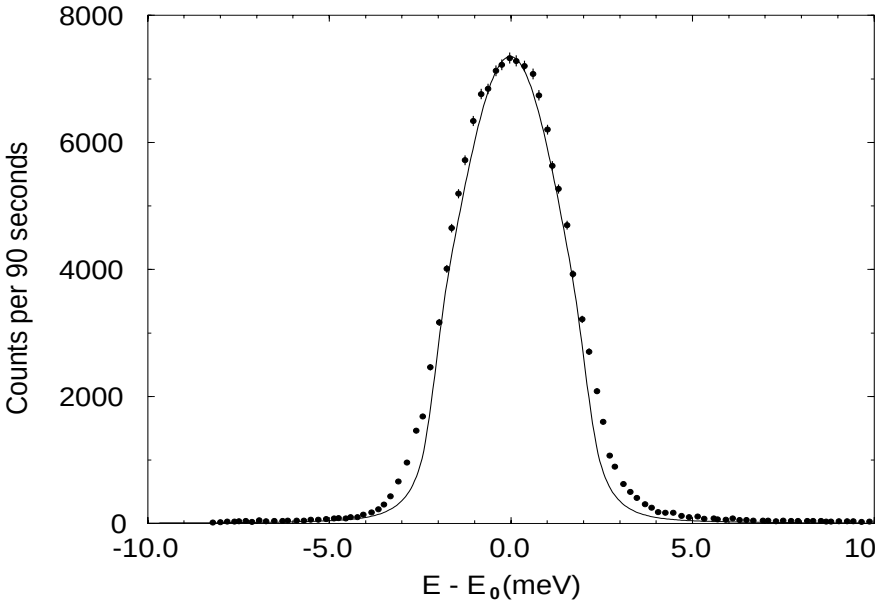

Figure 3.11: The measured energy response function (dots with error bars) compared with a simulation (solid line). $E_0 = 23.880\,keV$ is the nuclear transition energy of ^{119}Sn. The FWHM of the measured energy response function is 3.6 meV.

crystals one after another in a dispersive geometry, which provides 0.1 μrad angular resolution and has an energy bandwidth of 0.6 meV. It is done at X-ray energy of 22.649 keV. It turned out to be narrower than the initial estimation of about 15 μrad. The transmitted beam profile is shown in Fig. 3.12. The simulated energy resolution function is obtained by first integrating the curve in Fig. 3.12 over the angle and then reversing the energy scale. The FWHM of this simulated resolution function is 3.54 meV. By comparing Fig. 3.12 and Fig. 3.10, we can see that the result we will get from a monochromator, e.g. the energy resolution, depends on the characteristics of the monochromator as well as on the incident beam. It is our experience that the performance of a monochromator is affected quite strongly by the performance of upstream optics, e.g., the high-heat-load premonochromator.

The throughput of the monochromator is measured by placing ionization chambers before and after the high-resolution monochromator. The flux of the x-ray beam before the high-resolution monochromator was measured as 8.3×10^{12} photons per second per 100 mA storage ring current in a measured energy bandwidth of 2.6 eV. This gives a spectral flux of $3.2 \times 10^{12} ph/s/100mA/eV$. After the monochromator, we obtained $9.0 \times 10^{8} ph/s/100mA$ in the energy bandwidth of 3.6 meV, or a spectral flux of $2.5 \times 10^{11} ph/s/100mA/eV$. These numbers are derived from the current

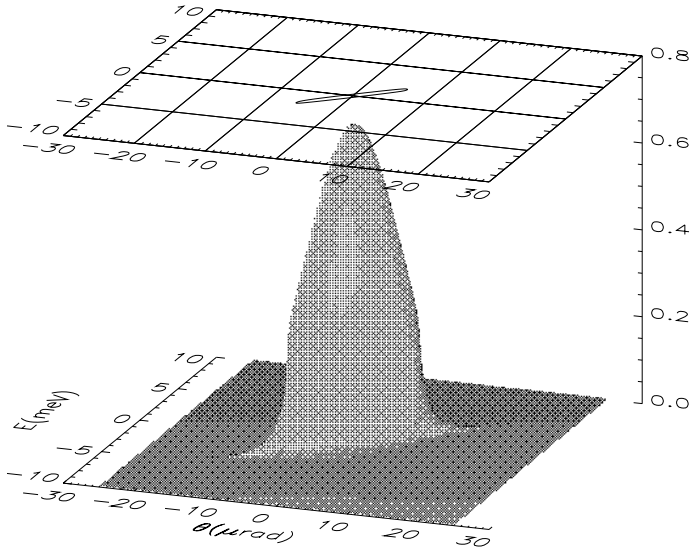

Figure 3.12: The transmitted beam profile of an incident beam with a Gaussian vertical angular profile of 12 μrad FWHM through the Si(4 0 0) – (12 12 12) monochromator.

readings from ionization chambers flowing He and N_2, respectively. It should be pointed out that both the incident beam and the beam transmitted through the monochromator have structure in their respective energy-angle space. So the above mentioned "spectral flux" — that obtained by taking the total flux and dividing it by the energy bandwidth — is only an averaged characteristic of the beam considered. But due to the significant difference in the bandwidths, only a small energy region of the incident beam, which is comparable to the monochromator bandpass, affects the transmission through the monochromator. As a result of this, the local spectral flux of that part of the incident beam should be used to compare with that of the beam transmitted by the monochromator. Lacking such detailed knowledge of the incident beam, we content ourself with the average spectral flux. The efficiency of this optical element can be understood as the ratio of spectral fluxes before and after the monochromator. From the above numbers, we obtain an efficiency of 8%. To simulate this measured efficiency we assume the incident beam has a Gaussian profile in the energy-angle space with FWHM of 12 μrad in angle and FWHM of 2.6 eV in energy and take the two dimensional integral of the curve in Fig. 3.12 and the integral of the incident beam profile. The integrals are regarded as the total fluxes of the transmitted and the incident beams respectively. Then dividing them by the corresponding energy bandwidth gives the averaged spectral fluxes, from which the efficiency is estimated to be 12%.

Table 3.3: The parameters for the 1-meV monochromator.

reflection	θ_B	α	b	$\omega_o(\mu rad)$	$\omega_h(\mu rad)$
(4 4 4)	19.34°	-18.47°	0.0248	10.3	0.25
(12 12 12)	83.48°	70.53°	1.96	0.20	0.39

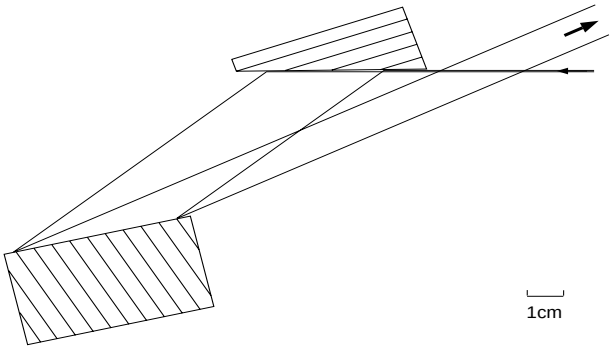

Figure 3.13: The schematic of the 1 meV two-crystal monochromator for 23.880 keV X-rays with reflections Si(4 4 4) – (12 12 12). For a list of parameters see Table 3.3.

3.5 A 1-meV Monochromator for ^{119}Sn

The previously described 3.6 meV monochromator for 24 keV X-rays is not very efficient due to the angular mismatch between the first and the second reflections. In light of the fact that the beam divergence at the beamline is only about 12 μrad (vertical) and may become even smaller as the high-heat-load monochromator is improved (the intrinsic width of symmetric diamond (1 1 1) reflection, which is used as the premonochromator, is 7.24 μrad), the design for this high resolution monochromator can be improved by using a reflection of higher order than (4 0 0). Table 3.3 lists the parameters for a new monochromator [44], which is shown in Fig 3.13. Its DuMond diagram (Fig 3.14) clearly shows the improvement over the previous monochromator. Its transmission function is shown in Fig. 3.15. If the same incident beam condition as assumed in Section 3.4 is used, we simulate the transmitted beam profile as shown in Fig. 3.16. With this incident beam, it has an energy resolution of 0.80 meV and an efficiency of 44%. The increased efficiency or spectral flux is the direct result of the better angular acceptance matching between the two reflections.

Its resolution function is measured and the result is shown in Fig. 3.17. The

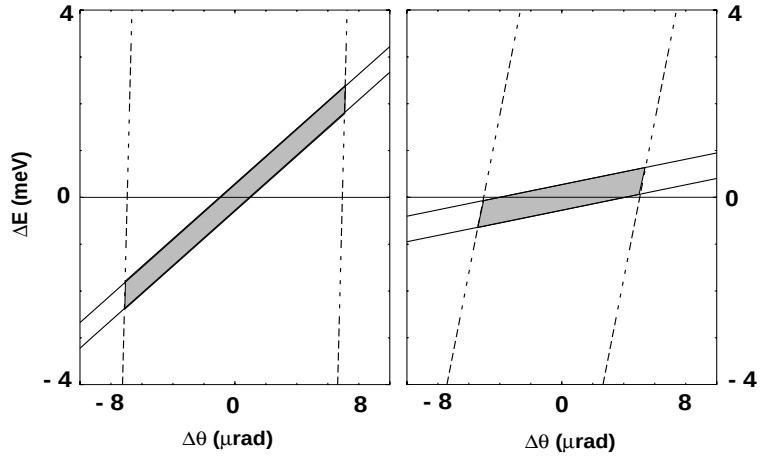

Figure 3.14: The DuMond diagrams at the incident faces of first crystal for both Si(4 0 0) – (12 12 12), on the lift, and Si(4 4 4) – (12 12 12), on the right. The dashed lines represent the first crystal and solid lines Si(12 12 12).

measured resolution is 0.98 meV and is wider than the simulation and the measured total flux is also about forty percent lower. In an attempt to better monitor the crystal temperature, a hole is drilled through beneath the surface of the Si(4 4 4) crystal to put thermistor in. The hole has a diameter of about 2.5 mm and is 1 mm under the center of the surface. Its residual strain or its mere presence might cause deformation of the part of the crystal diffracting X-ray beam. The other possibility could be the quality of the silicon boule used to make this crystal.

Nevertheless, we obtain a total flux of about $3 \times 10^8 ph/s/100mA$ after this monochromator with an incident beam size of 0.4 mm vertical by 3 mm horizontal. It provides adequate flux for conducting nuclear resonant scattering experiments.

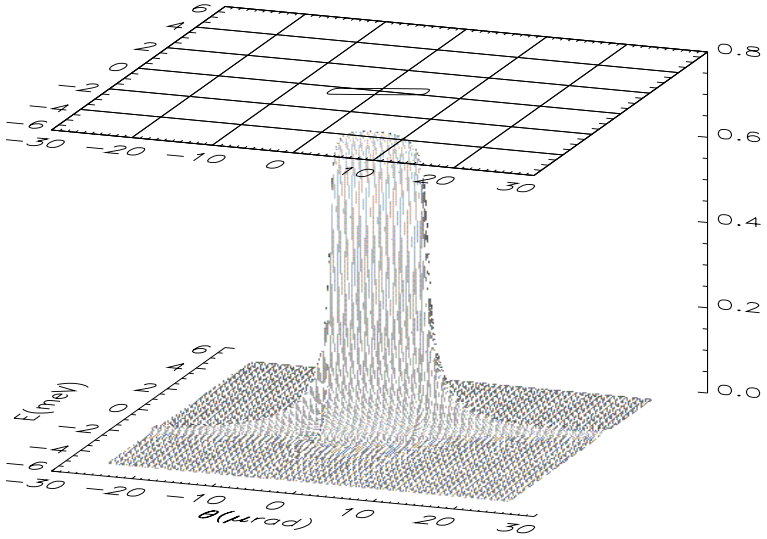

Figure 3.15: The calculated transmission function of the monochromator Si(4 4 4) – (12 12 12). The peak reflectivity is 0.705 and the contour is drawn at half the maximum reflectivity.

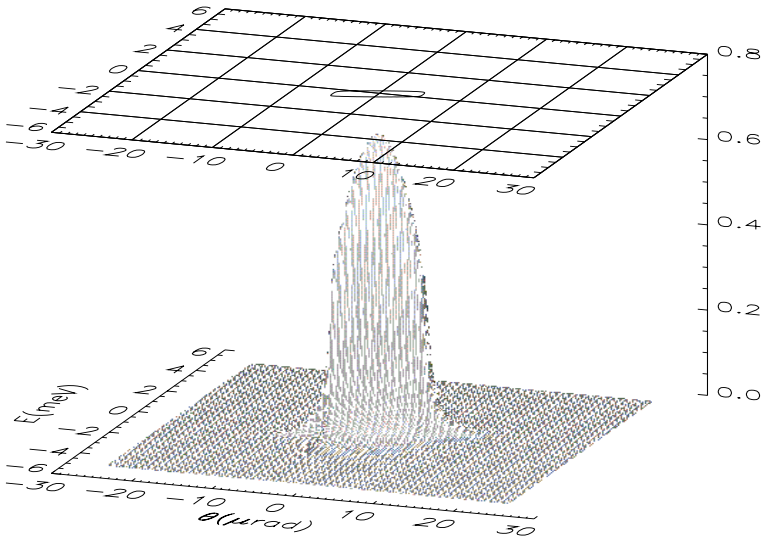

Figure 3.16: The transmitted beam profile of an incident beam with a Gaussian vertical angular profile of 12 μrad FWHM through the Si(4 4 4) – (12 12 12) monochromator. The peak reflectivity is 0.704 and the contour is drawn at half the maximum reflectivity.

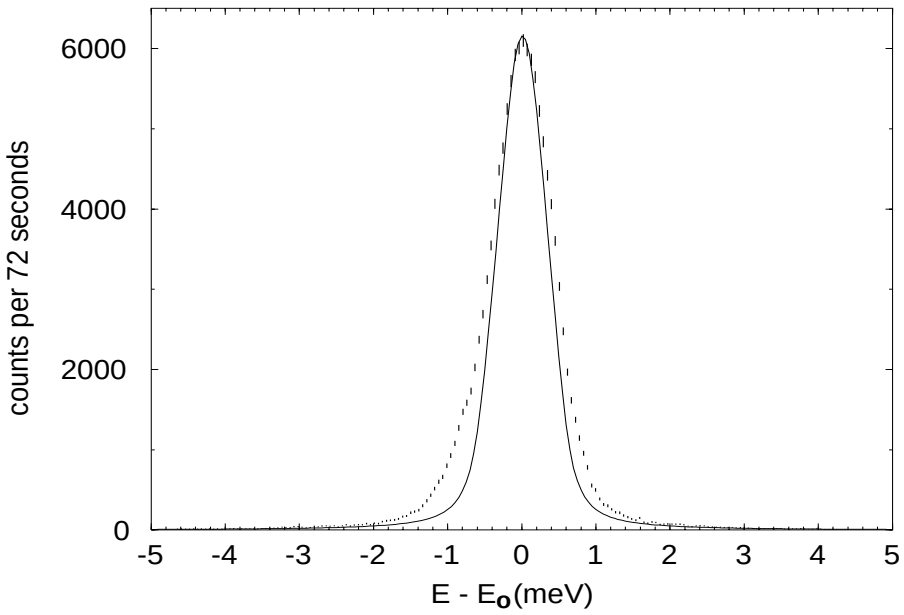

Figure 3.17: The measured energy response function (vertical bars) compared with a simulation (solid line). The vertical bars represent the error bars. $E_0 = 23.880\,keV$ is the nuclear transition energy of ^{119}Sn. The FWHM of the measured energy response function is 0.98 meV. The width of the simulation is 0.80 meV.

Table 3.4: The parameters for the 1-meV monochromator with a "beam contractor".

reflection	θ_B	α	b	$\omega_o(\mu rad)$	$\omega_h(\mu rad)$	reflectivity
(4 4 4)	19.34°	-18.47°	0.0248	10.3	0.25	0.983
(12 12 12)	83.48°	70.53°	1.96	0.20	0.39	0.754
(1 1 1)	4.75°	4.12°	14.02	2.89	40.6	0.990

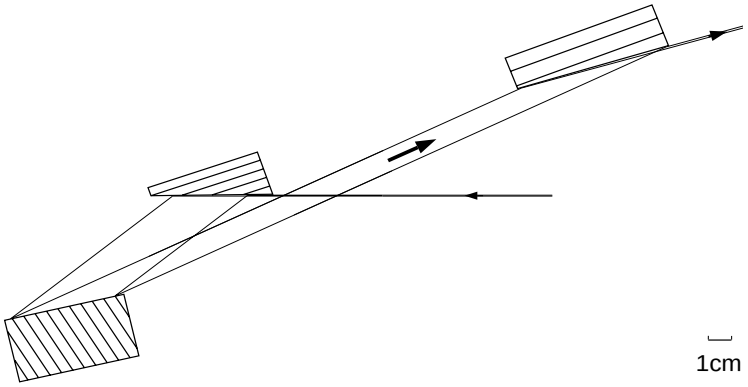

Figure 3.18: The schematic of the 1 meV two-crystal monochromator for 23.880 keV X-rays in 3-crystal setup, with reflections Si(4 4 4) – (12 12 12) – (1 1 1). For a list of parameters see Table 3.4.

3.6 An X-ray Beam Contractor

One tradeoff of this 1 meV monochromator is its big exiting beam size, which is obviously seen in Fig. 3.13. Use the asymmetry parameters b from Table 3.3 in the equation of beam size, Eq. (3.9), we find that the exiting beam has a vertical beam size 20.6 times that of the incident beam. This is a practical problem as we discussed before (page 40). One way to solve this problem without using the channel-cut design is to use a third crystal, which is asymmetrically cut to reduce the beam size. We want its asymmetry factor close to 20 and its angular acceptance larger than the exiting beam divergence from the first two crystals. To get maximum reflectivity and angular acceptance, we choose Si(1 1 1) reflection, the lowest order reflection in silicon with $\theta_B = 4.75°$ for 23.880 keV X-rays. The finished crystal has an asymmetry angle of 4.12°, which corresponds to an asymmetry factor of 14.02. With this third crystal, the final vertical beam size is only 1.47 times that of the incident beam. With this

asymmetry factor, it has an angular acceptance of 2.89 μrad, which is much larger than the 0.39 μrad exiting beam divergence from the second reflection (see Table 3.3). The large angular acceptance and 99% reflectivity of this beam contractor ensure that it has only minute effects on the transmission function of the monochromator and thus leaves its energy resolution and spectral transmission basically unchanged. The expanded table of parameters for this setup is shown in Table 3.4. The arrangement of three crystals is illustrated in Fig. 3.18. This set-up has been successfully used in measurements of thin films and with high pressure diamond anvil cells.

3.7 Energy Scale Generation

The operation of flat crystal monochromators involves turning one or both crystals relative to the incident beam. The way to translate the angular readings into relative energies is prescribed in Eq. (3.13), from which we can see that the operation of the high-resolution monochromator requires very precise mechanical control of the movements of the crystals. For example, to scan the resolution function shown in Fig. 3.11, the second crystal moves in angular steps of 0.07 μrad, which corresponds to energy steps of 0.2 meV. For monochromators with higher energy resolution the step size will be even smaller. We mount the crystals onto Kohzu KTG15 high resolution rotation stages which have a minimum step size of 0.025 μrad and a total range of 4°. These rotation stages are also coupled to Heidenhain ROD800C angle encoders with AWE1024 interpolator electronics. They have a resolution of 0.175 μrad, and are used to calibrate long range angular motions.

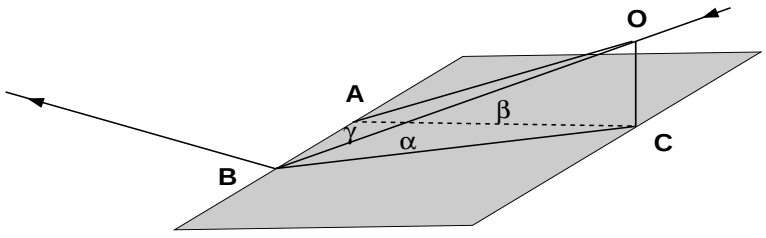

Figure 3.19: Misalignment of the rotaion axis. $\overline{AB}$ is the rotation axis, $\overline{OB}$ represents the incident X-ray beam, and points A, B, and C define the crystallographic plane. $\overline{AC} \perp \overline{AB}$, $\overline{OC} \perp$ plane ABC.

Care must also be taken to make sure that the motor readings, whose changes are denoted as $\delta\theta_1$ and $\delta\theta_2$, represent the true rotations of the crystallographic planes relative to the X-ray beam. In two cases this may not be true. One is if the rotation

axis is not perpendicular to the incident beam. The other is when the rotation axis is not in the crystallographic plane. The first case is illustrated in Fig 3.19. The relation among α, the true Bragg angle, β, the rotation angle, and γ, the angle between the incident beam and rotation axis, is,

$$\sin\alpha = \sin\beta \, \sin\gamma \tag{3.15}$$

from which we can find for small changes in α and β,

$$\Delta\alpha = \Delta\beta \left[1 - \frac{\cos^2\gamma}{\cos^2\alpha}\right]^{1/2} \tag{3.16}$$

It tells us that when γ is not 90° the measured angular change is bigger than the real change of Bragg angle ($\Delta\alpha < \Delta\beta$) and the deviation is more pronounced for higher Bragg angles when α is close to 90°. For Si(12 12 12) reflection at 23.880 keV ($\alpha = 83.48^\circ$), 1° misalignment, i.e., $\gamma = 89^\circ$, results in 1% difference between $\Delta\alpha$ and $\Delta\beta$; and 2° gives 5%.

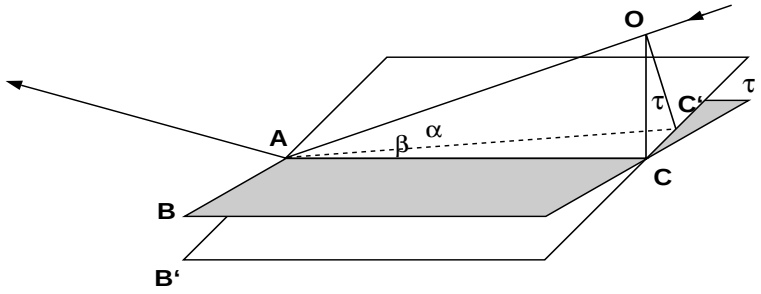

Figure 3.20: Misalignment of the tilt axis. $\overline{AB}$ is the rotation axis, $\overline{AC}$ is the tile axis, $\overline{OA}$ represents the incident X-ray beam. Points A, B', and C (or C') define the crystallographic plane. $\overline{AC} \perp \overline{AB}$, $\overline{OC} \perp$ plane ABC, and β is the angle between $\overline{AC}$ and $\overline{AO}$, the rotation angle. The tilt angle is τ. $\overline{OC'} \perp$ plane AB'C, the crystallographic plane. $\overline{OC'} \perp \overline{CC'}$, and α is the angle between $\overline{AC'}$ and $\overline{AO}$, the true Bragg angle.

The second type of misalignment, as shown in Fig 3.20, can be adjusted by tilt rotation. The tilt axis is perpendicular to the rotation axis and is in the crystallographic plane. Rotation along this axis moves the diffracting plane in and out of the vertical plane. For this case, we have the following relation,

$$\sin\alpha = \sin\beta \, \cos\tau \tag{3.17}$$

where τ is the tilt angle. Then we have

$$\Delta\alpha = \Delta\beta \left[1 - \frac{\sin^2\tau}{\cos^2\alpha}\right]^{1/2} \tag{3.18}$$

The expression resembles the one for the first case, so similar arguments follow for the tilt misalignment too. Again, for Bragg angle of $\alpha = 83.48°$, $\tau = 1°$ will cause $\Delta\beta$ to be 1% bigger than $\Delta\alpha$. These misalignment effects will introduce systematic errors in generating energy scales from the motor readings by Eq. (3.13). The overall effect can be approximated as a scaling factor of the energy scale generated. It will affect the accuracy at large energy differences, e.g., the high energy modes measured in an INRS experiment.

One other effect we have to consider concerns the temperature stability of monochromator crystals. A temperature variation will cause a slight change in lattice spacing d and will in turn affect the Bragg angle at a fixed energy, the Darwin curve width, and the refractive correction to the Bragg angle. In Section 3.2 we have shown that the Darwin width is not sensitive to small temperature variations. Thus we can assume the characteristics of monochromator, i.e. its transmission function, is not affected by small temperature changes. What is actually affected is the center energy of the X-ray beam which passes through the monochromator. The temperature variation has the apparent effect of changed angles of the monochromator crystals, which causes a shift in energy. This effect of shift in energy can be expressed as

$$\frac{\delta E}{E_0} = \frac{\Delta\theta_1 + \Delta\theta_2}{\tan\theta_{B1} + \tan\theta_{B2}} \tag{3.19}$$

where

$$\begin{aligned} \Delta\theta &= \Delta\theta_B + \Delta\rho \\ \Delta\theta_B &= -\alpha\,\delta T\,\tan\theta_B \\ \Delta\rho &= -\alpha\,\delta T\,(2 + \tan^2\theta_B)\,\rho \end{aligned}$$

Here $\Delta\theta$ is used to distinguish from $\delta\theta$ in Eq. (3.13), which is the actual change of the crystal angle by moving motor. And $\Delta\theta_B$ is the change in Bragg angle and $\Delta\rho$ the change in the refractive correction. Since ρ is on the order of μrad (i.e. 10^{-6}), $\Delta\rho \ll \Delta\theta_B$. It is sufficient to consider the changes in Bragg angle only. In case of our (4 0 0)–(12 12 12) monochromator, a 17 mK change in the temperature of second crystal, δT_2, will cause an energy shift of 1 meV of the X-rays pass through the monochromator.

Besides taking certain measures to improve the temperature stability of the crystals, in an experiment that does not have high count rate, we can take several shorter scans to minimize the temperature effect and later combine these data sets into a single spectrum to get better statistics. Even then, sometimes there is still going to

be small temperature drift during each short scan. In such cases we can use Eq. (3.19) to correct energy scale obtained by Eq. (3.13). To monitor the crystal temperatures, thermistors are attached to them, and both the temperature and the angle readings are used to determine the energy scale according to

$$\frac{\delta E}{E_0} = \frac{\delta\theta_1 - \delta\theta_2 - \alpha \cdot (\delta T_1 \tan\theta_{\mathrm{B1}} + \delta T_2 \tan\theta_{\mathrm{B2}})}{\tan\theta_{\mathrm{B1}} + \tan\theta_{\mathrm{B2}}} \,. \tag{3.20}$$

Chapter 4

Applications to Tin Materials

Tin is an element which is in the same group as carbon and silicon and can be found in many inorganic and organic compounds and materials. Its dynamics inside these materials will provide us better understanding of their properties. Inelastic nuclear resonant scattering method had been successfully applyed to iron materials. Our task was to extend this technique to ^{119}Sn. The binding strength of Sn varies significantly among Sn compounds. A measure of this strength is the recoilless factor, which is valued at 0.66 for $CaSnO_3$ and can be as low as 0.03 for white tin at room temperature. We have performed INRS experiments on several Sn materials, and established that this technique is applicable to a variety of Sn materials, including metal, alloy, oxides, and superconducting compounds, in various forms, powders, films, and inside high pressure cells. Through these studies, we have tested the lower limits of f-factor, concentration and total number of resonant isotopes for this technique, which can be used to assess the feasibility of future experiments with other samples. From the measurements we have done, we obtained Sn-partial phonon density of states of these compounds for the first time. They will increase our understandings of their dynamical and thermodynamical properties and will be useful in theoretical modeling of these systems.

4.1 Sn Oxides and Count Rate Estimation for INRS

Three tin oxides, SnO, SnO_2, and $CaSnO_3$, were measured by INRS. They are powder samples and enriched over 90% in ^{119}Sn. The experiments were done at room temperature. Initially, all three were measured using the 3.6 meV monochromator described in Section 3.4. The spectra are shown in Figures 4.1 and 4.2. Later, SnO and SnO_2 were measured again using the monochromator in Section 3.5 with 1 meV resolution. SnO samples under high pressure were also measured with 1 meV resolution. The 1 meV spectra of SnO and SnO_2 are shown in Figures 4.3 and 4.4. No dependence on incident photon wave vector is present because for powder samples this dependence is averaged out. Comparing the spectra of same sample with different resolutions, we see clearly the effect of energy resolution, the relative height of elastic peak to the phonon part of the spectrum increases as resolution improves. This agrees with the estimate we did in Section 2.7 (see Eqs. 2.78 and 2.76). The energy scan ranges in these scans are about $\pm 80\, meV$, that is more than twice the Debye temperature for Sn sublattice in these oxides. The scan step size is generally

Table 4.1: Recoilless factor f, mean kinetic energy per atom, mean force constant, and mean displacement of Sn atoms of listed Sn oxides, derived from INRS measurements.

compound and (resolution) used	f	$\overline{T}$ (meV)	$\overline{K}$ (N/m)	$\overline{u}$ (Å)
SnO (3.6 meV)	0.28(4)	13.1(7)	208(8)	0.16
SnO (1.2 meV)	0.271(8)	13.5(1)	178(4)	0.16
SnO_2 (3.6 meV)	0.631(9)	14.2(3)	462(26)	0.097
SnO_2 (1.2 meV)	0.629(3)	13.97(6)	371(6)	0.097
$CaSnO_3$ (3.6 meV)	0.657(7)	14.1(2)	377(14)	0.093

chosen to be one third of the energy bandwidth of monochromatized X-ray beam. For the 3.6 meV experiments, the step size is 1 meV for SnO_2 and $CaSnO_3$, and 0.5 meV for SnO. The step sizes in the 1-meV experiments are 0.25 meV.

There is only one equivalent site for Sn atoms in these compounds, as can be seen in their crystal structures (Figures 4.6, 4.8, and 4.10). Thus, as discussed in Section 2.5, the phonon excitation probability function can be separated into single and multi-phonon contributions, and this is shown in the figures. For SnO the multi-phonon contribution is relatively strong, on the same order of magnitude compared to single phonon part. This reflects the fact that SnO lattice is soft. It is also obvious from the derived partial phonon density of states, Figures. 4.5, 4.7, and 4.9. The Sn partial DOS in SnO_2 and $CaSnO_3$ extends to about 40 meV, while it stops at 25 meV for SnO. The recoilless factor f, mean kinetic energy, and mean force constant of Sn atoms for these sample are derived from the spectra by the moment sum rules in Section 2.4. They are listed in Table 4.1. Also listed are the square roots of the mean square displacements derived from the recoilless factor f.

The partial DOS for SnO_2 and $CaSnO_3$ have almost identical peak positions and very similar structures (Figures 4.7 and 4.9). This may be explained by the fact that Sn atoms have similar local environments in both compounds, despite the very different structures and symmetries of the two lattices. The Sn atom is centered at an oxygen octahedron in both compounds, though the octahedron is slightly stretched in one direction for SnO_2. The bond lengthes are also close. In perovskite $CaSnO_3$, the six Sn–O bonds have a length of 1.96 Å (Fig. 4.10), while in SnO_2, there are four Sn–O bonds in a plane which is 2.052 Å, and two perpendicular to the plane with length of 2.057 Å (Fig. 4.8). This suggests that the dynamics of Sn atoms is

mostly determined by the surrounding oxygen octahedron, and in lattice dynamics calculations only the nearest neighbor Sn-O force constants are important for Sn atoms.

In Fig. 4.5, we show a shell model calculation of partial phonon density of states of Sn sub-lattice in SnO [51]. In this model, Buckingham potential, $V(r) = ae^{-br} - c/r^6$, between ions is used and force constants are taken from lattice dynamics study of SnO_2 [52] and then adjusted to fit optical modes frequencies measured by IR and Raman experiment [53]. The model calculation has the basic features of the DOS we measured. However, a similar calculation performed for SnO_2 does not yield DOS which resembles the result from INRS measurement.

Before we go on with more samples, let's compare the experimentally observed intensity with the estimations by Eq. (2.76). For SnO, the density is 6.45 g/cm^3. For highly enriched sample, this equals to a density of nuclear resonant isotope of about 2.8 $\times 10^{22} cm^{-3}$. Using this number together with nuclear resonance properties listed in Table 2.1 and f factor, Debye temperature derived from the experiment, we have the following estimation of intensity for the phonon part of the spectrum,

$$\overline{I_m}(E \neq 0) \quad = \quad 3 \times 10^{-4}\, \eta\, I_0$$

where I_0 is the incident beam flux and η represents the detection efficiency. The detector efficiency is assumed to be 6% (the absorption rate of 23.88 keV X-ray in 100 μm silicon). And as discussed before, for ^{119}Sn inelastic nuclear resonant experiments, it is dominantly the nuclear fluorescence, ie., 23.88 keV X-rays, that are detected. With a internal conversion coefficient of 5.12, this gives another factor of 6. We can also assume about one third of total solid angle is covered by the detector. The incident beam flux was about 3 $\times 10^8$ photons per second. Plugging in these numbers, we will have 300 counts per second. In Fig. 4.1 panel (d), we can see about 3000 counts average for the phonon part, dividing it by the counting time of 20 second, we have 150 counts per second. That is on the same order as the estimate. A similar estimate for SnO_2 gives 100 counts per second, while the averaged intensity of phonon part in panel (e) of Fig. 4.1 is about 25 counts per second. So we can use Eq. (2.76) as a fairly good estimate for INRS experiments.

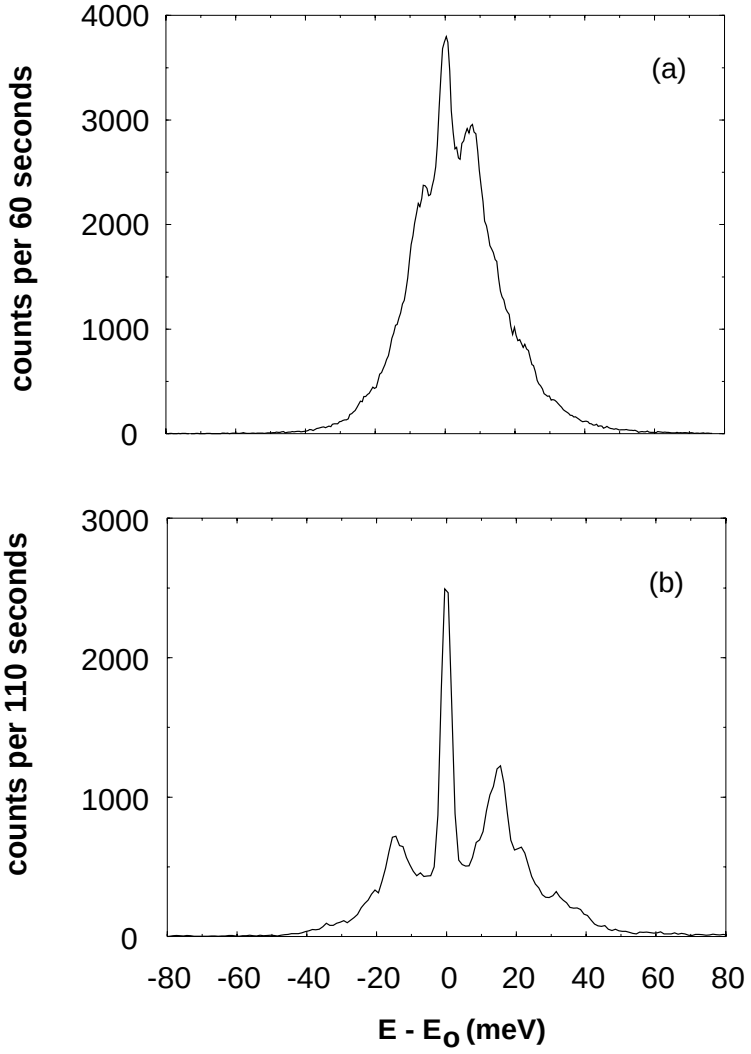

Figure 4.1: INRS spectra for SnO (a) and SnO_2 (b) with 3.6 meV resolution. E is the X-ray energy and E_0 is the nuclear transition energy.

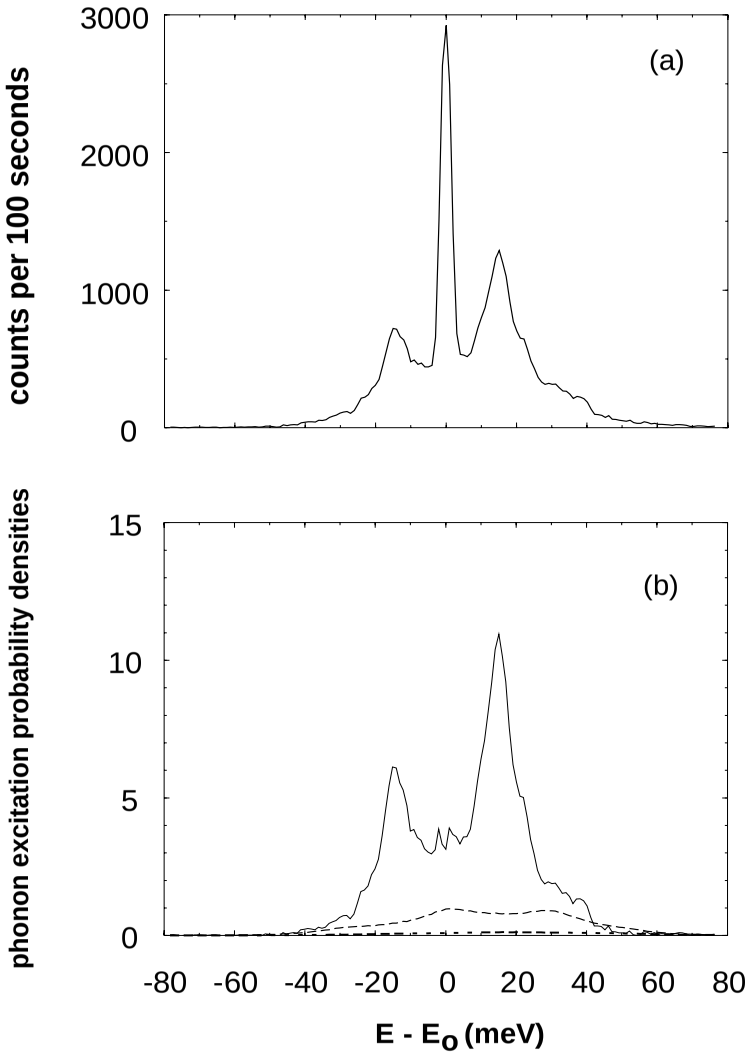

Figure 4.2: INRS spectrum for $CaSnO_3$ (a) with 3.6 meV resolution. Panel (b) shows separated phonon excitation probability densities $S_1(E)$ (solid line), $S_2(E)$ (dashed line), and $S_3(E)$ plus the rest (dotted line). E is the X-ray energy and E_0 is the nuclear transition energy. The same conventions are used for results shown later.

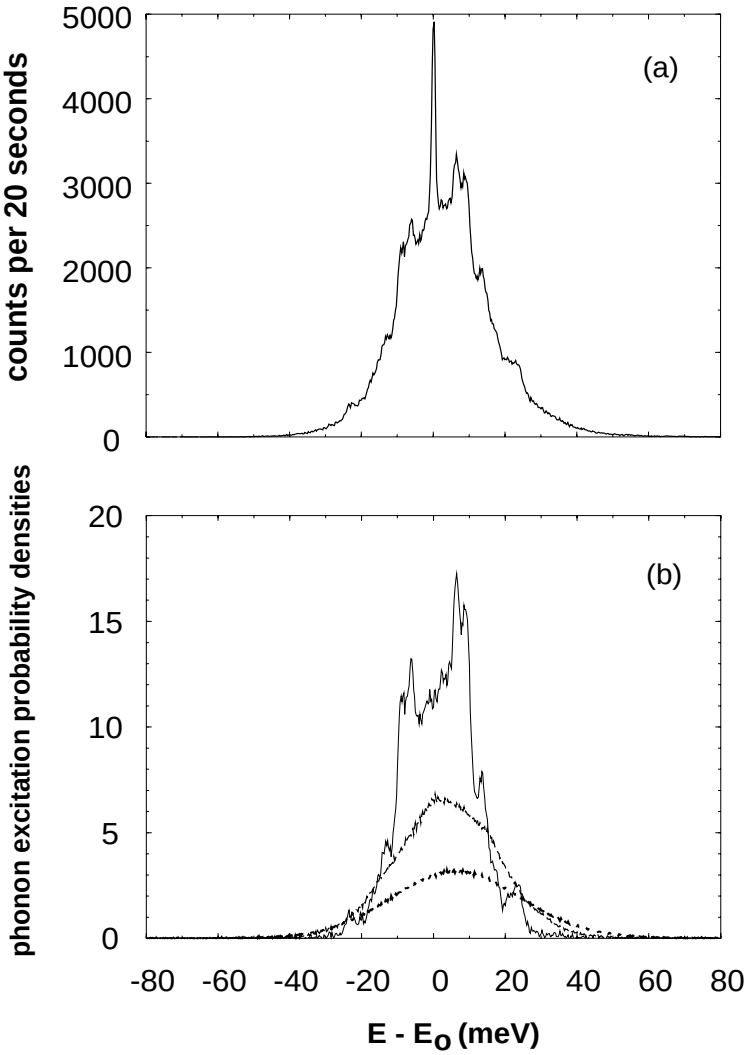

Figure 4.3: INRS spectrum for SnO (a) with 1 meV resolution. Panel (b) shows separated phonon excitation probability densities $S_1(E)$, $S_2(E)$, and $S_3(E)$ plus the rest. E is the X-ray energy and E_0 is the nuclear transition energy.

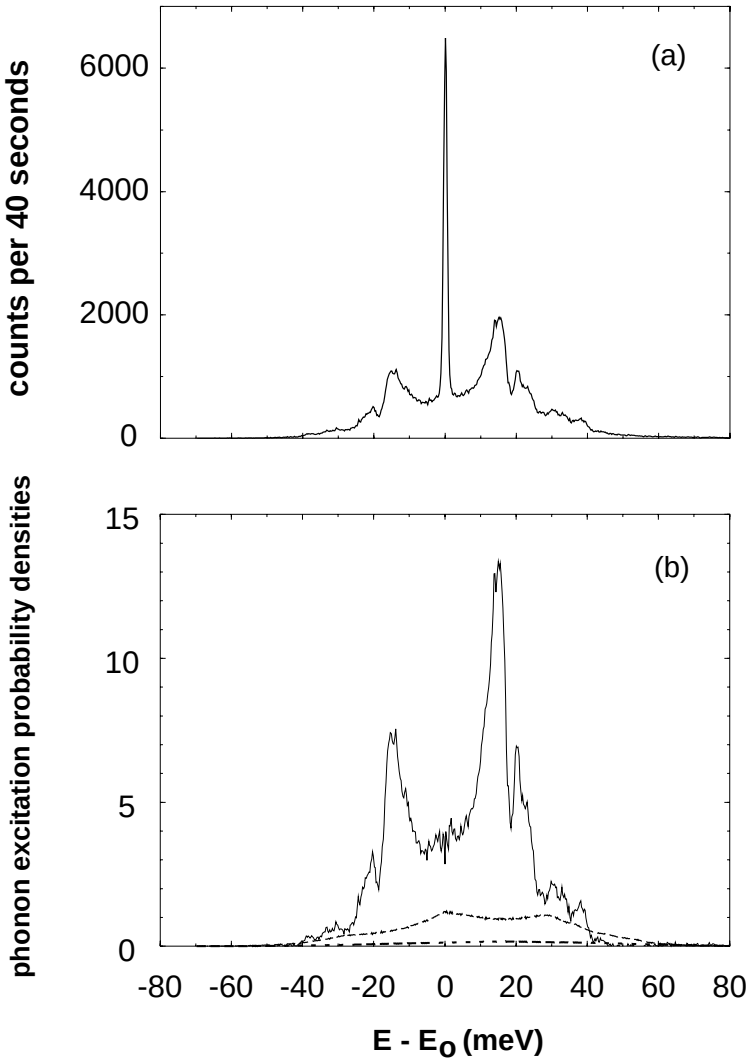

Figure 4.4: INRS spectrum for SnO_2 (a) with 1 meV resolution. Panel (b) shows separated phonon excitation probability densities $S_1(E)$, $S_2(E)$, and $S_3(E)$ plus the rest. E is the X-ray energy and E_0 is the nuclear transition energy.

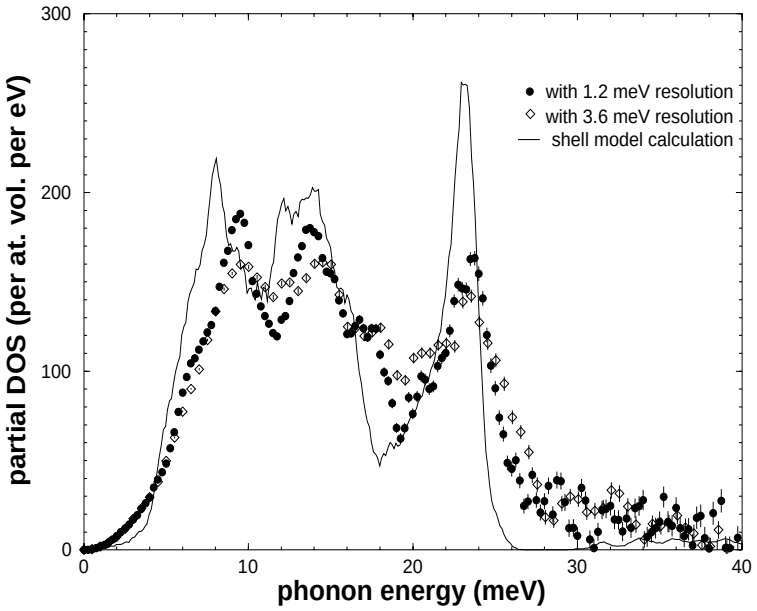

Figure 4.5: Partial phonon density of states for SnO.

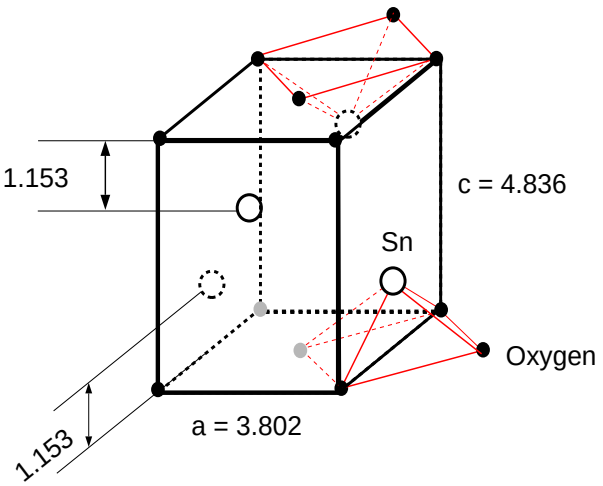

Figure 4.6: Crystal structure of SnO.

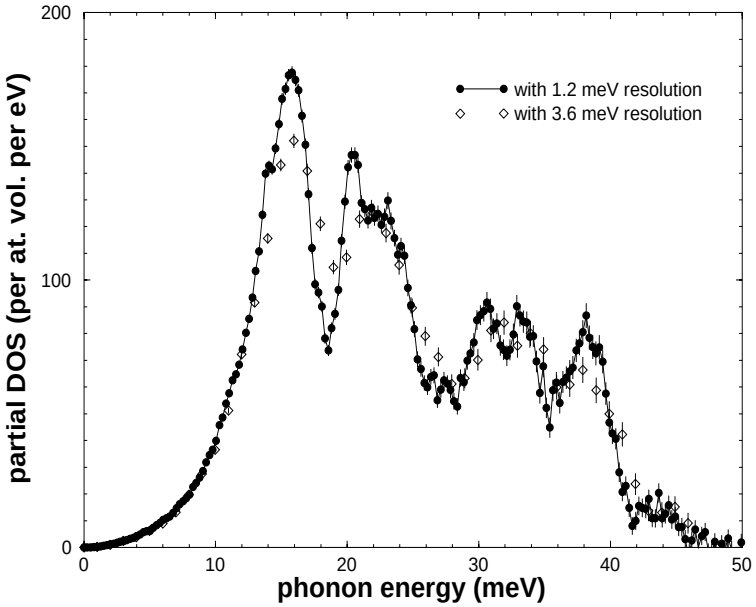

Figure 4.7: Partial phonon density of states for SnO_2.

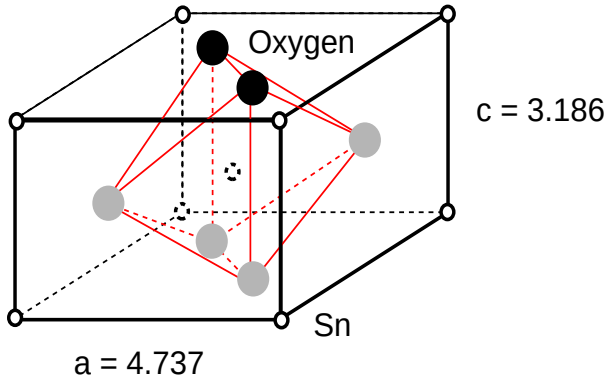

Figure 4.8: Crystal structure of SnO_2.

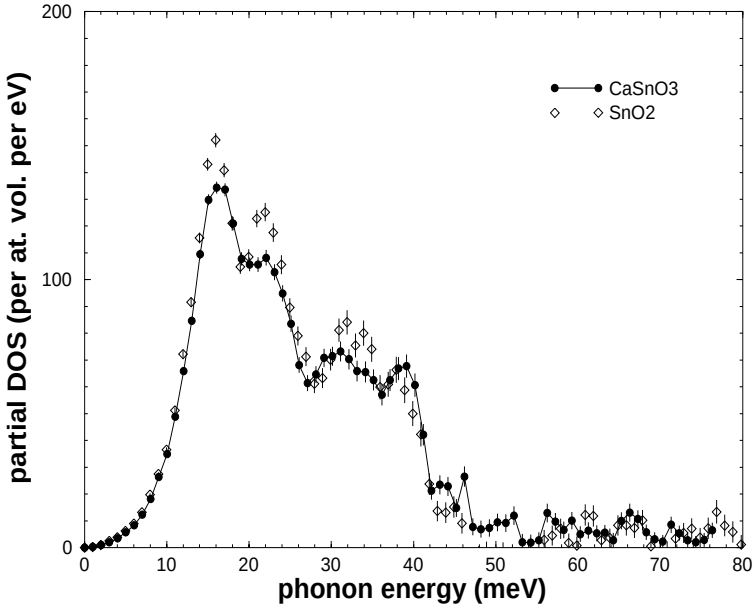

Figure 4.9: Partial phonon density of states for SnO_2 and $CaSnO_3$. Here data with 3.6 meV resolution is used.

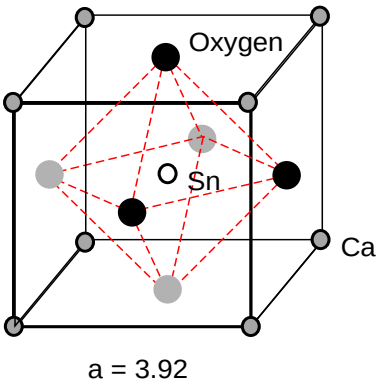

Figure 4.10: Crystal structure of $CaSnO_3$.

4.2 SnO under High Pressures

SnO has a second phase above 1.5 GPa, which is an orthorhombic structure with space group Pm2n. INRS measurements were conducted for samples under 3.5 GPa and 7 GPa pressures[1]. The sample size in the Diamond Anvil Cell (DAC) used is about 200 μm in diameter and 20 μm in thickness. The sample is enriched over 90% in ^{119}Sn. That corresponds to only about 7 $\times 10^{16}$ nuclear resonant isotopes in the sample. With the help of a third crystal to reduced the vertical beam size after high resolution monochromator, we are able to increase the flux density at the sample. However, a good portion of the beam in horizontal direction is not being used and a factor of 15 (3 mm beam size over 0.2 mm sample size) is lost in flux. Focusing in both directions is necessary to utilize the full beam. The DAC uses beryllium gasket and has two wide openings perpendicular to the X-ray beam path through the sample region. Two APD detectors with active area of 100 mm^2 are placed into these openings. With this setup and incident flux about 3 $\times 10^8$ photon per second, we have a count rate of 1 per second at the phonon peak.

The experiments were done at room temperature using 1.2 meV monochromator with an additional third crystal to reduce the vertical beam size (see Section 3.5. The energy scan range is $\pm 80\, meV$ and step size is 0.3 meV. Measured spectra and normalized phonon excitation probability density functions are shown in Figures 4.11 and 4.12 for samples under high pressure. For comparison the data under normal pressure is show in previous section in Fig. 4.3. Derived lattice dynamic properties are listed in Table 4.2 and partial phonon DOS of Sn sub-lattice is shown in Fig. 4.13 together with that at ambient pressure. We observe significant increase of f-factor with increasing pressure. By going from ambient pressure to 3.5 GPa in phase II, the phonon spectrum undergoes significant changes besides a slight shift of all phonon modes to higher energy. Among them, there is the disappearance of low energy modes at about 6 meV and the appearance of new modes at 18 meV. It is also interesting to see that the phonon spectra at two high pressures are quite different too, though they are supposed to be in the same phase. The most obvious is the broadening of the optical phonon peak at about 25 meV. There are modes at 8 meV disappearing.

[1]These experiments were in collaboration with Prof. G. Wortmann and Dr. Rainer Lübbers of University of Paderborn, Germany, who provided the DACs.

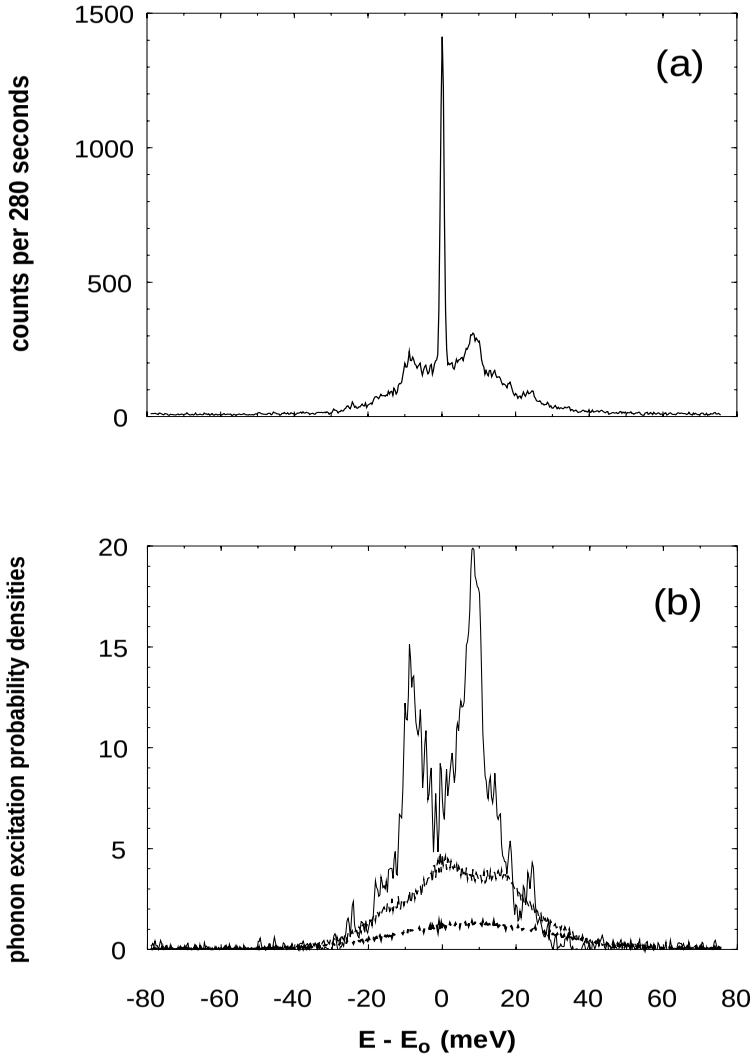

Figure 4.11: INRS spectrum for SnO under 3.5 GPa (a). Panel (b) shows separated phonon excitation probability densities $S_1(E)$, $S_2(E)$, and $S_3(E)$ plus the rest. E is the X-ray energy and E_0 is the nuclear transition energy.

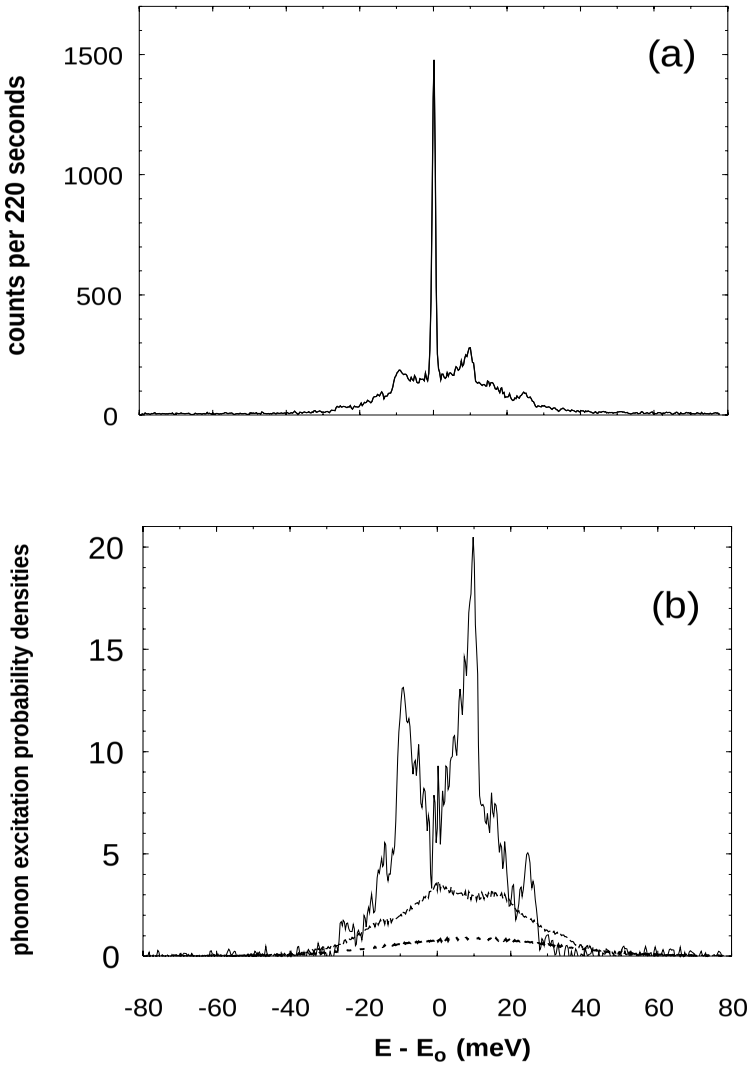

Figure 4.12: INRS spectrum for SnO under 7 GPa (a). Panel (b) shows separated phonon excitation probability densities $S_1(E)$, $S_2(E)$, and $S_3(E)$ plus the rest. E is the X-ray energy and E_0 is the nuclear transition energy.

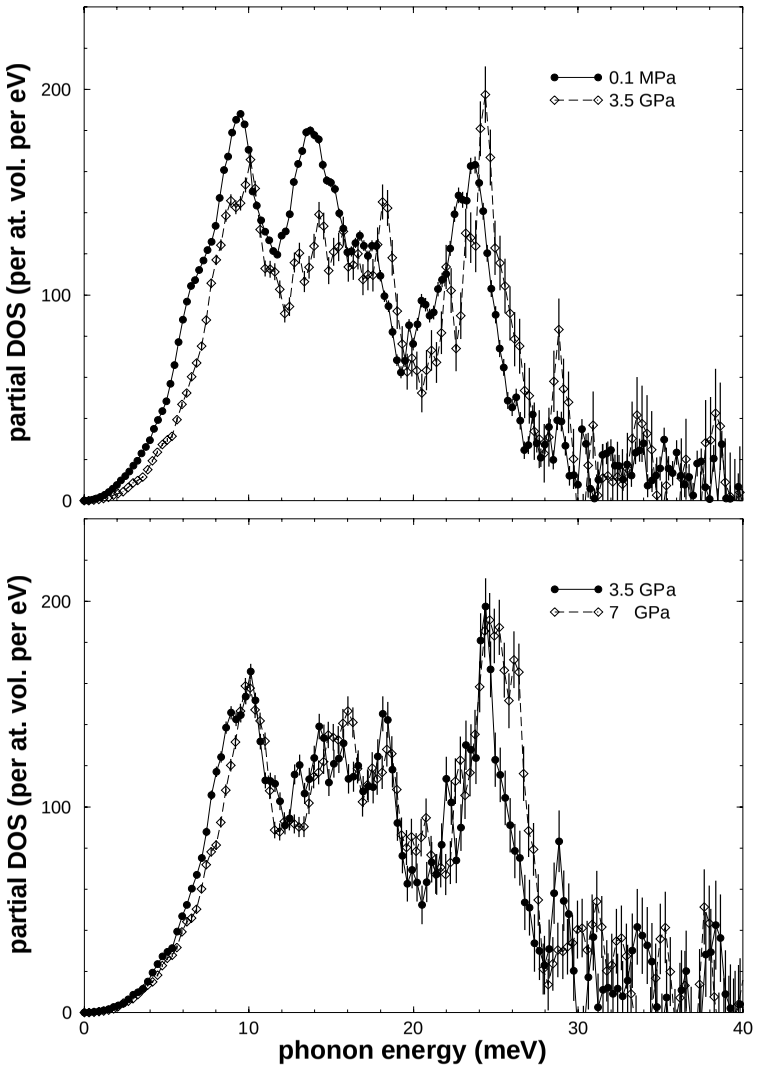

Figure 4.13: Partial phonon density of states for SnO under different pressures.

Table 4.2: Recoilless factor f, mean kinetic energy per atom, and mean force constant of Sn atoms of SnO under different pressures, derived from INRS measurements. Also listed are estimated mean displacement of Sn atoms.

pressure (GPa)	f	$\overline{T}$ (meV)	$\overline{K}$ (N/m)	$\overline{u}$ (Å)
0.1 MPa (ambient)	0.271(8)	13.5(1)	178(4)	0.16
3.5 GPa	0.40(2)	15.0(5)	251(63)	0.14
7 GPa	0.45(2)	13.5(4)	332(57)	0.13

4.3 β-Sn and INRS with Low f-Factor Samples

Tin is a group IV element following C, Si, Ge and preceding Pb. Its bonding characteristics lies on the border between covalency and metallic bonds. Under normal condition tin is a metal with a (double) body-centered tetragonal crystal structure. This phase is called β-Sn, or white tin. While it is a stable phase for tin under normal temperature and pressure, Si and Ge are metallized into the structure under pressure. At low temperature tin is more stable in its α-Sn phase (gray tin) which has the diamond structure as C, Si, and Ge. The α-Sn is a semiconductor with zero band gap. The phase transition under normal pressure happens at 13.2 $^{\circ}C$.

Both an enriched and a natural Sn foil (β-Sn) were measured at room temperature with 1 meV energy resolution. The energy scan range is $\pm 80\, meV$ and step size is 0.25 meV. Measured spectra are shown in Figure 4.14. The difference between the spectra for enriched and natural sample is due to the elastic peak suppression effect. By equations (2.76) and (2.78), the inelastic part of the spectrum is proportional to the nuclear resonant isotope concentration n, while the elastic peak is proportional to its square root. Thus by going from an enriched sample to a unenriched one, i.e., in the above figure, from (a) to (b), the concentration is decreased and the inelastic part is reduced more relative to the elastic peak. We see that the elastic suppression effect is more serious for enriched sample.

For β-Sn at room temperature, the phonon excitation probability function cannot be separated. The reason is that the lattice is very soft, with f factor estimated about 0.03, at room temperature the multi-phonon processes dominate. In Eq. (2.40), if the higher order terms are not small compared with S_1, then the sum is less sensitive to it, as a result S_1 can not determined reliably. Another difficulty comes from the fact that the elastic peak needs to be removed before the separation of multi-phonon terms. However, all terms in Eq. (2.40) make contribution at $E = E_0$, not just S_0. In the close vicinity of the elastic peak, S_1 can be very well approximated by the Debye model (Eq. 2.90), but multi-phonon terms depend on the whole phonon spectrum and thus can not be estimated satisfactorily beforehand. So if multi-phonon terms dominate single phonon term S_1, the elastic peak can not be removed reliably, which in turn prevents separation of single phonon term.

Clearly, f-factor puts a limit on the feasibility of INRS. We just see that data analysis cannot be carried out for sample with $f = 0.03$. In next section we will present another sample with low f-factor, $f = 0.16$ to be exact for α-Sn at room temperature. We will see that it is possible to separate multi-phonon terms in that case, where the higher order terms are almost of the same magnitude that of S_1 (Fig. 4.16). To demonstrate the correlation between the significance of multi-phonon terms and value of f-factor, we can take a look at figures of $S(E)$ for three samples measured, Fig. 4.16 for α-Sn with $f = 0.16$, Fig. 4.3 for SnO with $f = 0.27$, and Fig. 4.4 for SnO_2 with $f = 0.63$. For samples with very low f-factors at room

temperature, in order to get phonon density of states, we can lower the sample temperature, thus reduce the multi-phonon contributions and make the separation of S_1 term possible. Within the harmonic lattice approximation, phonon DOS is not affected by temperature and lowing the temperature provides a solution to the above problem.

High pressure INRS experiments were also done for β-Sn, with 3.6 meV resolution. At room temperature, β-Sn tranforms from a double body-centered tetragonal structure to body-centered tetragonal at 9.2 GPa [54]. Our experiments were performed at below (7.9 GPa) and above (15 GPa, 20 GPa) this transition pressure. The DAC has a sample chamber of 200 μm in diameter and about 30 μm in thickness. The spectra are shown in Fig. 4.15. Unfortunately, as mentioned above, the overwhelming multi-phonon contributions at room temperature prevents further data analysis. The sample put under high pressure is also highly enriched. The different appearances of the spectra under ambient and high pressure (the clear center peaks in cases of high pressures) is due to the fact that in DAC the sample thickness (30 μm) is less than electronic absorption length (105 μm) which determines the penetration of inelastic resonant X-rays. So, the effective area density of resonant isotopes is smaller than that under ambient pressure where the sample is an enriched Sn metal foil about half millimeter thick. The elastic resonant penetration depth is so small and the same in both cases, that the effective area density for elastic resonance is the same and the elastic part of the spectra has same signal rate per beam cross section.

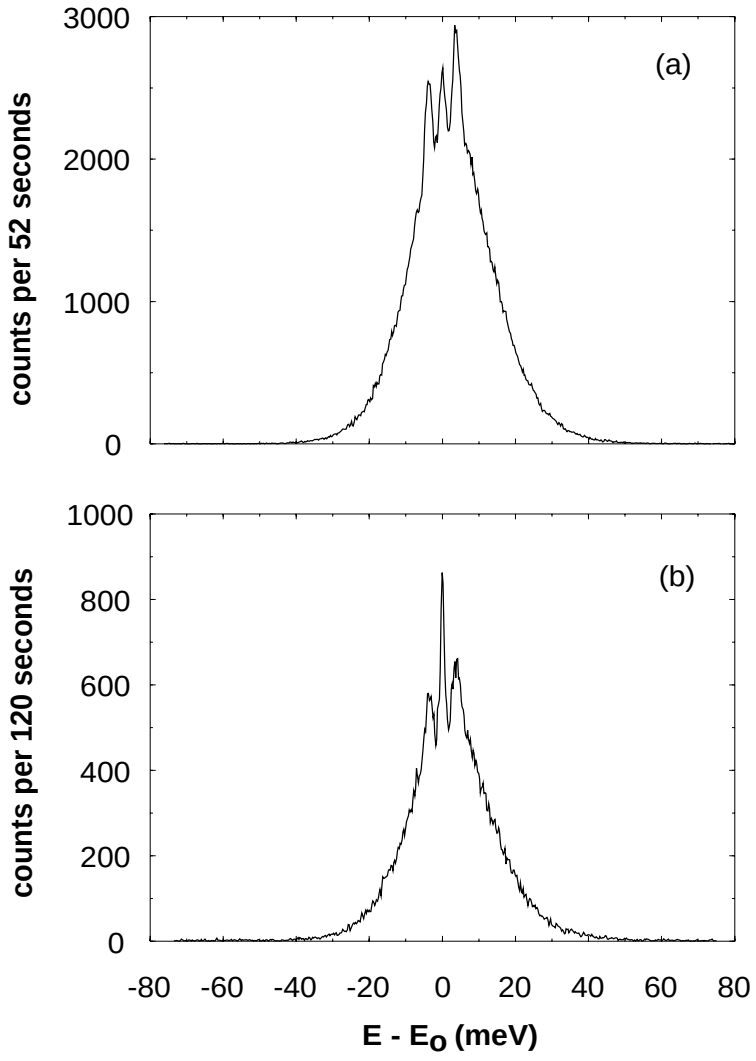

Figure 4.14: INRS spectra from an enriched (a) and an unenriched natural β-Sn sample (b).

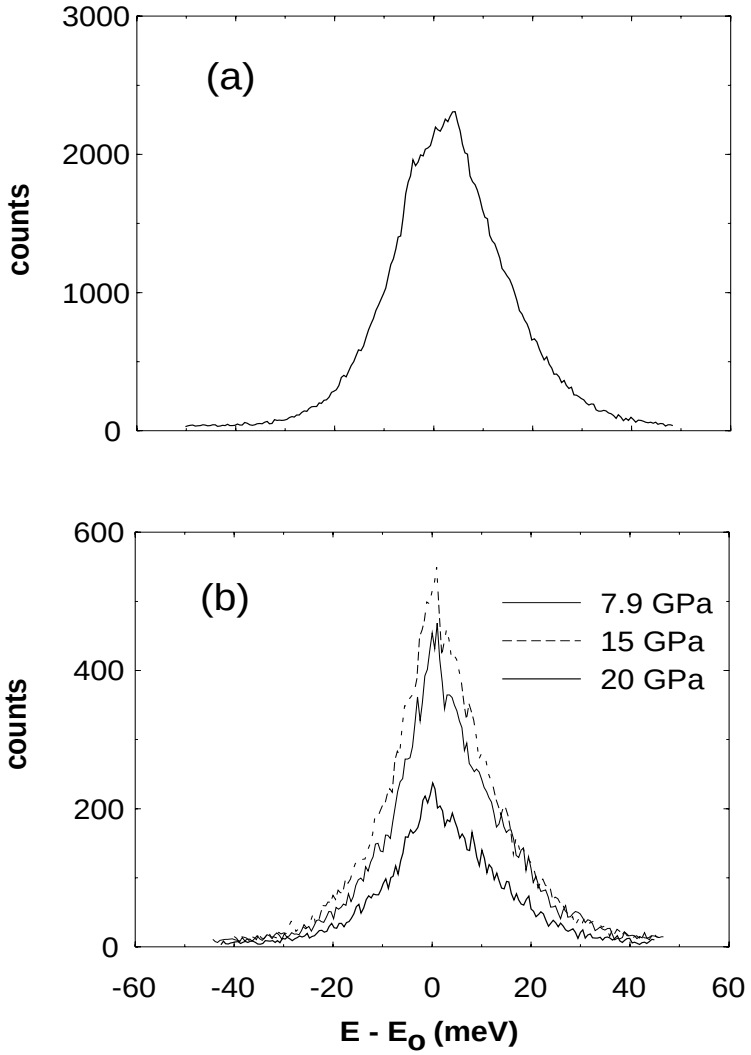

Figure 4.15: INRS spectra for β-Sn under ambient (a) and high pressures (b), with 3.6 meV energy resolution. E is the X-ray energy and E_0 is the nuclear transition energy.

4.4 α-Sn Film

The low temperature phase α-Sn has diamond crystal structure with lattice constant of 6.49 Å. This phase can be stablized at room temperature if grown on lattice-matched substrate. α-Sn films[2] were grown on semi-insulating $CdTe$ (1 0 0) substrates by molecular beam epitaxy (MBE). The in-plane lattice mismatch of α-Sn with $CdTe$ (1 0 0) substrate was 0.18%. The substrate thickness was 1 mm. Prior to depositing the α-Sn, a 3000 Å CdTe buffer layer was grown on the $CdTe$ (1 0 0) substrate at 250 $^{\circ}C$. For α-Sn the growth temperature was 0 $^{\circ}C$. A typical growth rate was 0.4 Å per second. The tin layer is 2000 Å thick and in single crystal phase checked by *in situ* reflection high-energy electron diffraction (RHEED). The α-Sn (1 0 0) film grown on $CdTe$ (1 0 0) has a (1×1) reconstructed surface. The samples are enriched in ^{119}Sn over 95%. In order to increase the count rate, we put two such films side by side along the X-ray beam direction and make X-ray beam incident at a very shallow angle.

The electronic absorption length is 133 μm in α-Sn for 23.88 keV X-rays, and the elastic resonant absorption length is only 0.24 μm. Since the films are only 0.2 μm thick, all parts of the Sn layer contribute to INRS signals. For a 2000 Å thick film, surface and interface constitute only a small part of the sample, we can say that what we measure is the bulk property of α-Sn.

The INRS spectrum is shown in Fig. 4.16 with phonon excitation probability densities. With an f factor of 0.16, α-Sn also has significant multi-phonon contributions, but not to the degree of preventing the separation of $S(E)$. For α-Sn, the derived lattice dynamic properties are listed in Table 4.3 and phonon DOS is shown in Fig. 4.17 together with an *ab initio* calculation [55]. Coherent inelastic neutron experiments were done and resulted in dispersions along a few high symmetry directions [56]. There were also theoretical calculations and modeling for lattice dynamics of α-Sn [57]. Recently, there is an effort to apply *ab initio* electronic structure calculation to examing the vibrational and thermodynamical properties of metals [55]. The calculation is based on direct total energy approach. Force constants are calculated for up to 8 nearest neighbors by the planar force constant method. The total energy is based on electronic structure calculation in the Density Functional Theory in the Local Density Approximation with the expansion of the electronic wave function in plane waves and the use of pseudopotentials. The calculated phonon dispersion is shown in Figure 4.18 compared with inelastic neutron measurements [56]. The overestimate of one of the acoustic mode in this calculation is obvious in both figures showing the dispersion and phonon DOS. By comparing the calculation with both the neutron and INRS measurements, this calculation technique is validated and improvement may be made.

[2]The films were made by Dr. Sunglae Cho at Department of Physics and Astronomy, Northwestern University.

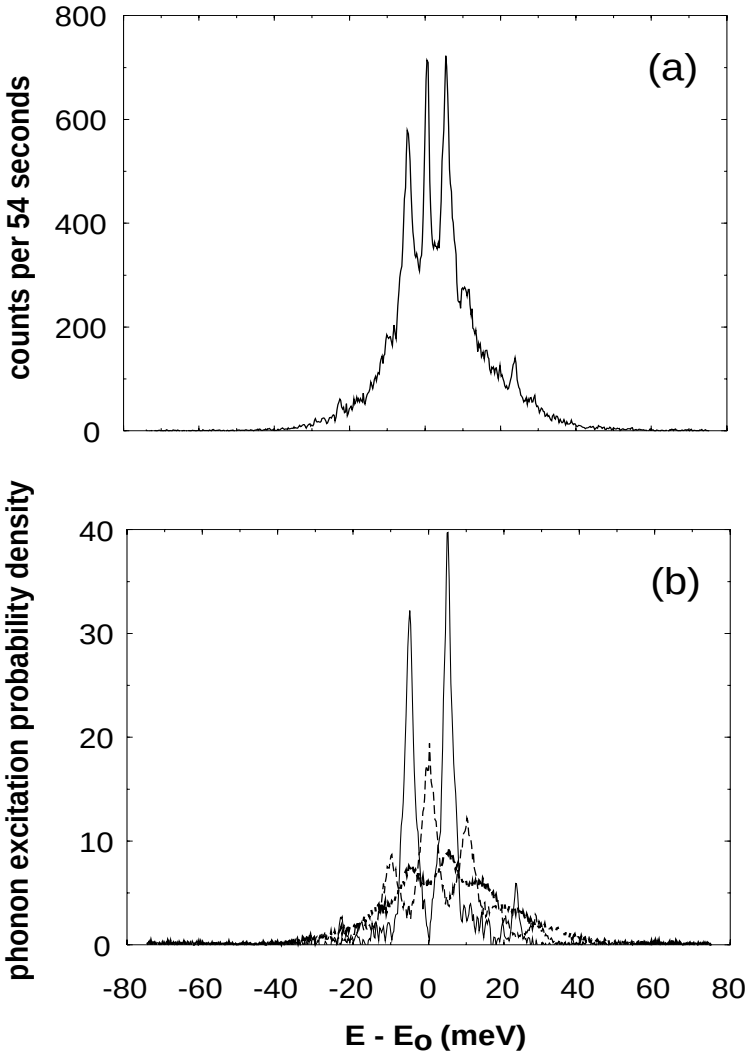

Figure 4.16: INRS spectrum for α-Sn (a). Panel (b) shows separated phonon excitation probability densities $S_1(E)$, $S_2(E)$, and $S_3(E)$ plus the rest. E is the X-ray energy and E_0 is the nuclear transition energy.

Table 4.3: Recoilless factor f, mean kinetic energy per atom, and mean force constant of α-Sn, derived from INRS measurements. Also listed are estimated mean displacement.

	f	$\overline{T}$	$\overline{K}$	$\overline{u}$
		(meV)	(N/m)	(Å)
α-Sn	0.16(2)	13.4(2)	155(16)	0.19

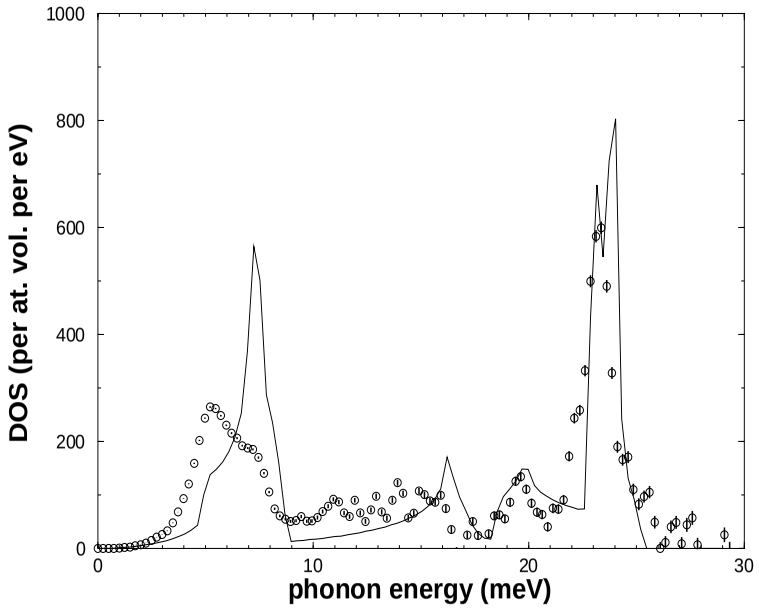

Figure 4.17: Partial phonon density of states for α-Sn from INRS measurement together with an *ab initio* calculation.

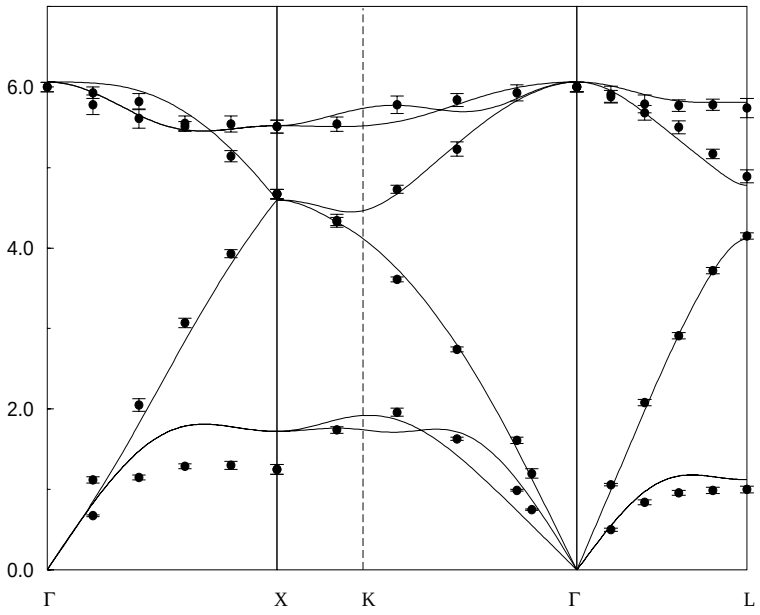

Figure 4.18: Phonon dispersion of α-Sn by an *ab initio* calculation compared with that measured by inelastic neutron scattering.

4.5 *A*-15 *Sn* Compounds

Superconducting intermetallic A15 materials are interesting because of their relatively high superconducting transition temperatures and critical fields, also of the interplay between their superconductivity, their structural phase transitions, and their temperature-dependent anomalies in properties like phonon spectra, elastic constants, and electric resistivities [58, 59]. Two A15 structure compounds Nb_3Sn and V_3Sn were measured by INRS technique, with an energy resolution of 3.6 meV. The energy scan range is $\pm 80\, meV$ and step size is 1 meV. Measured spectra and normalized phonon excitation probability density functions are shown in Figures 4.19 and 4.20. Derived lattice dynamic properties are listed in Table 4.4 and phonon DOS are shown in Fig. 4.21. The different positions of the higher energy peaks in these two materials could be understood as the result of mass difference of the other atoms in the lattice. Since we know that for a diatomic chain the optical mode frequency can be approximated proportional to $\sqrt{(1/M_a + 1/M_b)}$, with the atomic weights of 51 for V, 93 for Nb, and 119 for Sn, we estimate that for optical modes $\omega_{Nb_3Sn}/\omega_{V_3Sn} \sim 0.83$, which is very close to the observed $25meV/30meV = 0.83$ (see Fig. 4.21). The other obvious difference in the phonon DOS for these two materials is the different peak ratio between high and lower energy modes. For Nb_3Sn, the partial phonon DOS is compared with a calculation in Fig. 4.22. The calculation is based on lattice dynamics model derived from inelastic neutron scattering experiments [60].

A Mössbauer spectroscopy experiment was done on Nb_3Sn [61]. One of the main findings was an anomalously large temperature variation of resonant line shifts between 20 and 80 K, and was attributed to the isomer shift. The isomer shift is proportional to the s-electron density, which was found to be increasing with temperature in that range. Then this information was used to suggest that the high density of electronic states near the Fermi level is due to holes rather than electrons. It was argued that the second order Doppler shift in this temperature region has very weak temperature dependence according to several models. However, it was an assumption nonetheless. We can perform INRS experiments to find out the temperature dependent behavior of the second order Doppler shift and reevaluate the Mössbauer data. The finding itself will also be relevant to the dynamics of the system as a function of temperature.

Another conclusion from that study is that the forces on the tin atoms in this system are highly anharmonic. It was demonstrated by showing that the temperature-dependent f-factor data violated a condition set by harmonic approximation. At room temperature, the f-factor measured by Mössbauer spectroscopy was 0.27, which is low compare to our result of 0.46. It is well known that the absolute values of f-factor are not reliable from absorption experiment, but the relative ratio can be quite accurate. After readjusting the data according to the correction at room temperature, the temperature-dependent f-factor data basically agrees with harmonic model.

Table 4.4: Recoilless factor f, mean kinetic energy per atom, mean force constant, and the mean displacement of Sn in Nb_3Sn and V_3Sn, derived from INRS measurements.

	f	$\overline{T}$	$\overline{K}$	$\overline{u}$
		(meV)	(N/m)	(Å)
Nb_3Sn	0.46(3)	12.6(7)	132(79)	0.13
V_3Sn	0.40(2)	13.5(3)	167(24)	0.14

This should correct the original conclusion that the vibration of tin atoms is anharmonic over the entire temperature range. However, there is still a deviation from the harmonic model at around 80 K. Thus a temperature-dependent INRS study will reveal more information on this anomaly. The densities of states from such a study will also help us understand the dynamics of the structural phase transition.

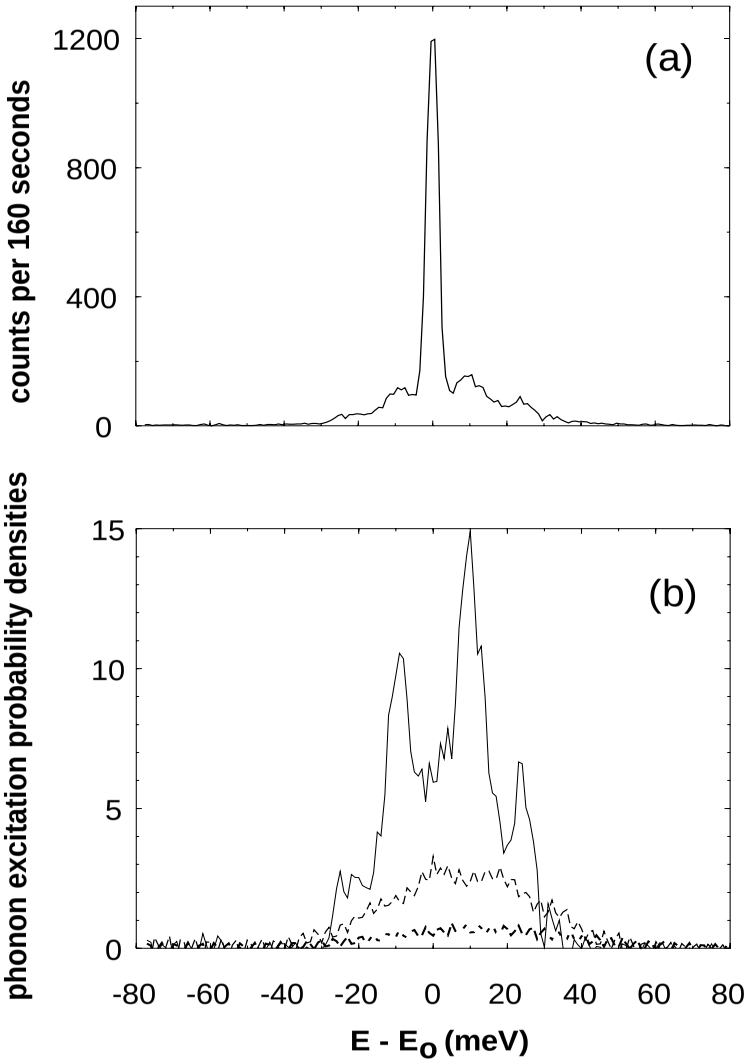

Figure 4.19: INRS spectrum for Nb_3Sn (a). Panel (b) shows separated phonon excitation probability densities $S_1(E)$, $S_2(E)$, and $S_3(E)$ plus the rest. E is the X-ray energy and E_0 is the nuclear transition energy.

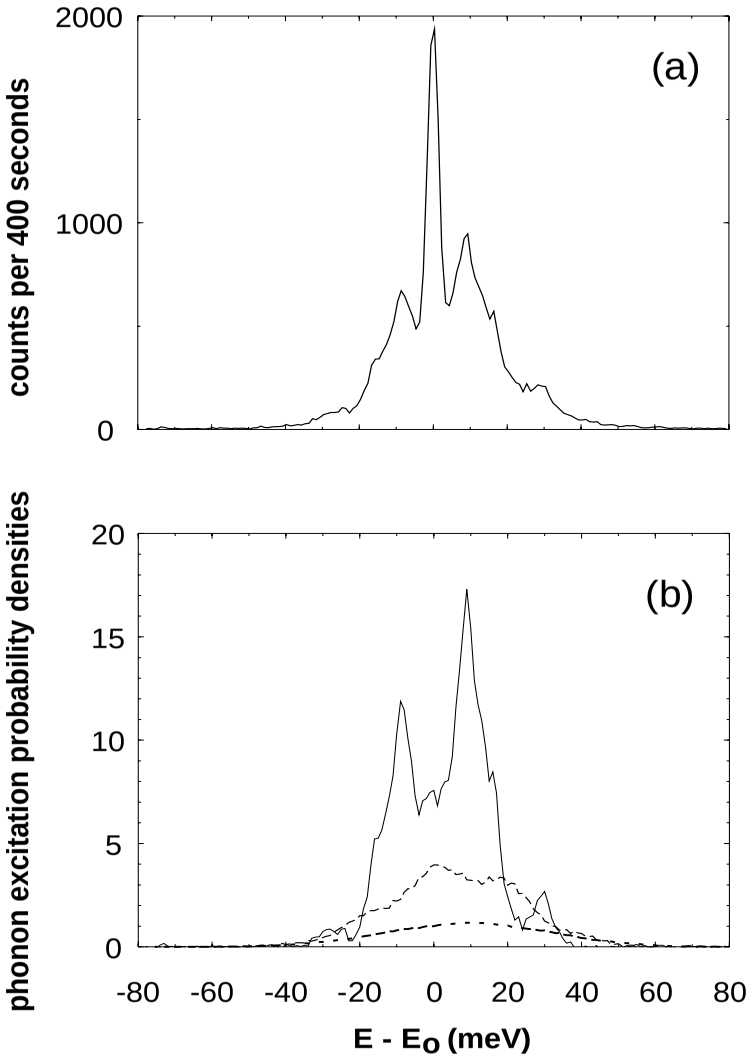

Figure 4.20: INRS spectrum for V_3Sn (a). Panel (b) shows separated phonon excitation probability densities $S_1(E)$, $S_2(E)$, and $S_3(E)$ plus the rest. E is the X-ray energy and E_0 is the nuclear transition energy.

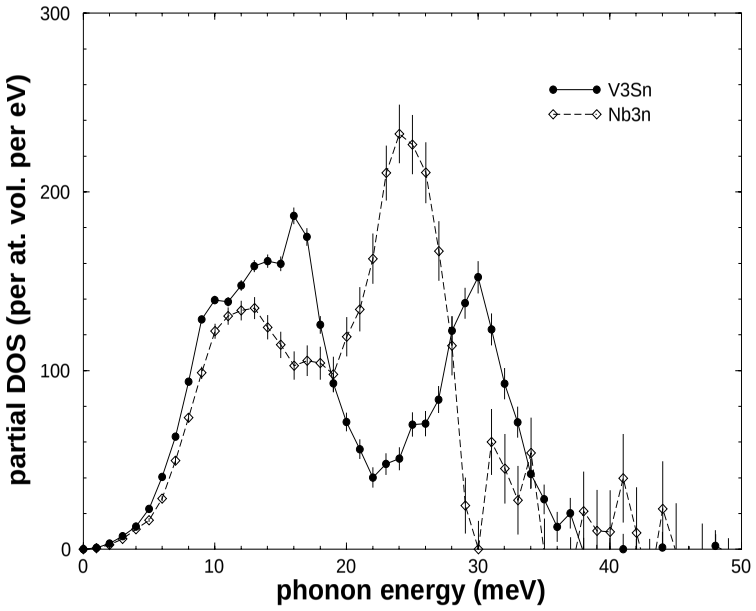

Figure 4.21: Partial phonon density of states for Sn in V_3Sn and Nb_3Sn from INRS measurements.

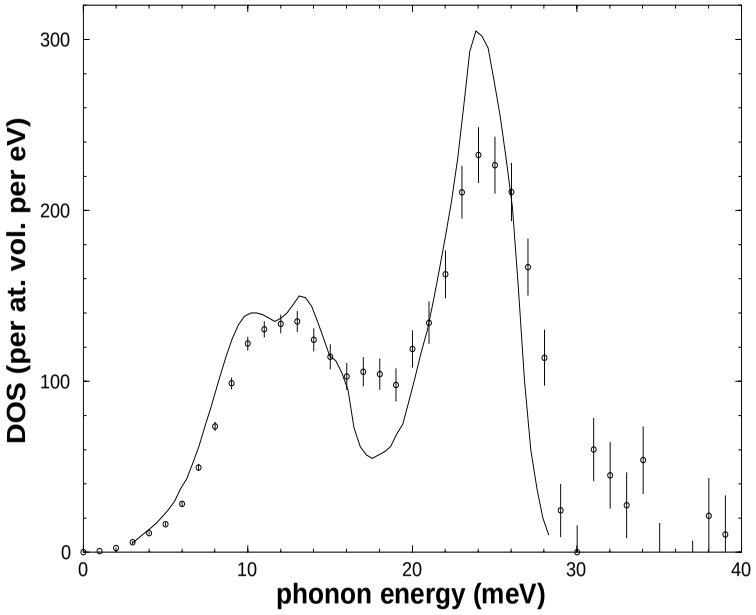

Figure 4.22: Partial phonon density of states for Nb_3Sn from INRS measurement together with a calculation.

4.6 *Pd-Sn* Alloy and INRS with Low Resonant Isotope Concentrations

At the very beginning of INRS ^{119}Sn experiments with meV energy resolution, to test the limit in count rate, we tried a sample of 12.5% Sn in Pd. There is no isotope enrichment. So with the natural abundance, there is only 1 at.% nuclear resonant isotope ^{119}Sn in the sample. Using the density of Pd, we can estimate the isotope density of ^{119}Sn to be 6.8 $\times 10^{20}$ per cubic centimeter. The spectrum is shown in Fig. 4.23. We observed 0.25 counts per second at the phonon peak and 0.75 counts per second at the elastic peak. Even though we performed the measurement for a long time, with accumulated total counting time over ten hours, there are still less than adequate numbers of counts. With this low number of total counts, the big statistical uncertainties prevent any further data analysis. In this measurement, the incident X-ray beam flux is about 9 $\times 10^8$ photons per second at 100 mA storage ring current, in an energy bandwidth of 3.6 meV. The beam has a vertical size of 5 mm. The APD detector has an active area of 5×5 mm^2. Under the same condition, we observed about 50 counts per second for highly enriched tin metal sample. The number density for tin metal is 3.7 $\times 10^{22}$ per cubic centimeter. The numbers are consistent for both samples.

With the improvement of detector and optics, it is quite feasible to measure the same sample today. Counting rate can be improved by using detector with larger active area, for example, we have 10×10 mm^2 APD available now. Reducing the vertical beam size will also help, as it will allow the incident beam on the sample to be at a more shallower angle and allow the detector to be closer to the sample. The crystal beam contractor described in Section 3.6 is designed for this purpose. It can also be achieved with channel-cut crystals, however, a more elaborate design is necessary to provide adequate efficiency, as we are facing difficulties at high X-ray energy (Section 3.3). And finally, a stronger source will ultimately make weak scattering mechanisms and dilute samples more accessible.

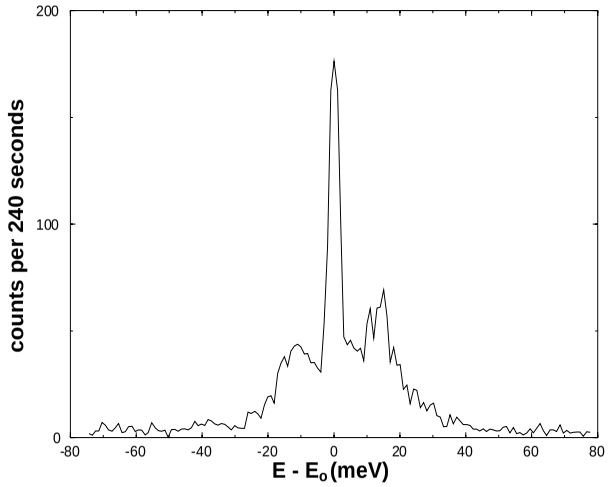

Figure 4.23: INRS spectra for 12.5% natural Sn in Pd. The energy resolution is 3.6 meV. E is the X-ray energy and E_0 is the nuclear transition energy.

Chapter 5

Concluding Remarks

We have extended the inelastic nuclear resonant scattering technique to isotope ^{119}Sn by developing high resolution optics at its nuclear resonant energy. We have analyzed this technique theoretically and experimentally, and showed that it is a unique technique to study lattice dynamics. It can provide useful information which cannot be obtained by other techniques, and it works with a variety of types of samples. It reveals dynamical information of a particular isotope in the sample and is capable to select vibrational modes with certain polarization. We have demonstrated its capability to measure samples with very small amount of materials, thus makes it possible to study thin films, multilayers, interfaces, impurities, dilute samples, and samples under very high pressures. Since the first observation of phonon excitation spectrum in 1994, there are more and more studies applying this method to various problems, e.g., thin film and interfaces [62], amorphous materials [63], molecular motions [64], and biological systems [65], etc. In the following sections we will discuss a few applications where INRS has clear advantages over other techniques.

5.1 Local Vibrational Dynamics

In Section 4.6 we showed an earlier attempt on a dilute sample of 12.5% Sn in Pd without isotope enrichment. As mentioned later in that section, with the improvement of detector and optics, it is quite feasible to measure the same sample today. That is to say, INRS is capable of studying Sn samples with about 1 at.% of resonant isotope concentration, or about 10^{20} per cm^3. This can also be estimated by Eq. (2.76) for the phonon part of the spectrum,

$$I(E) \quad \sim \quad \eta\, I_0\, \frac{n}{n_{el}}\, \frac{\sigma_0}{\sigma_{el}}\, \frac{\pi}{2}\, \frac{1-f}{2\Theta_{\rm D}}\, \Gamma \tag{5.1}$$

As discussed at the end of Section 4.1, for ^{119}Sn, the detection efficiency $\eta \sim 0.004$. Let's assume that $f = 0.5$, $2\Theta_{\rm D} = 100\, meV$, and $\sigma_0/\sigma_{el} \sim 100$, then for ^{119}Sn, we have,

$$I(E) \quad \sim \quad I_0\, \frac{n}{n_{el}} \times 10^{-7} \tag{5.2}$$

For ^{57}Fe, the detector efficiency is 0.94 for 6.4 keV X-rays and 0.23 for 14.4 keV X-rays, assuming the detector has an active region of 100 μm thick. Both nuclear

and atomic fluorescences are detected. With internal conversion coefficient of 8.21 and K-fluorescence yield of 0.347, we can estimate the channel weighted detector efficiency to be 0.3. Again assuming 1/3 of solid angle is covered by the detector, we estimate $\eta \sim 0.1$ for ^{57}Fe. Using the same numbers of σ_0/σ_{el}, f and $2\Theta_{\rm D}$ as for ^{119}Sn, we have,

$$I(E) \quad \sim \quad I_0 \frac{n}{n_{el}} \times 10^{-6} \tag{5.3}$$

Comparing this with the estimate for ^{119}Sn, we may conclude that for ^{57}Fe samples, an resonant isotope concentration of 0.1 at.% is possible to perform INRS experiments. It is the detector efficiency that makes the difference. In case of ^{119}Sn, the detection efficiency can be improved if the detector is capable to detect the 3.5 keV L-fluorescence.

The element selectivity and the ability to measure low concentration samples makes INRS an excellent tool to study local vibrational dynamics, for example, impurities, dopants, and interfaces. For example, in cases of substitutional impurities, besides the mass defects, the changes in force constants in the vicinity of the defect also plays an important role in determining the local impurity dynamics [66, 67, 68]. Analytical expressions were found for the impurity density of states which can be calculated from the DOS for the host lattice and two parameters. One is the mass ratio, the other is the ratio of the impurity-to-host force constant to the host-to-host force constant. Local vibrational states were predicted arising from the change in force constant. The systems of Sn in Pd [69] and Fe in Pd [70] were studied by Mössbauer spectroscopy. The Fe-Pd nearest-neighbor force constant was found smaller than that of Pd-Pd. However the Sn-Pd nearest-neighbor force constant was found to be larger, and there ought to be a localized state associated to Sn. In these studies, the mean kinetic energy and mean displacement for impurity atoms were calculated from the impurity (partial) phonon DOS of Sn, which was derived from Pd phonon DOS measured in neutron experiment by Mannheim's formula [68]. Then they were used to fit the measured resonant line shifts and f-factors at various temperatures. The INRS experiments will yield directly the impurity density of states, thus provides a direct test of Mannheim's theory.

5.2 Thin Films and Interfaces

X-rays have the advantage over neutrons in that only small amount of material is required in X-ray scattering experiments. This in general and the element selectivity in particular makes INRS a unique technique to study interfaces. For example, a single atomic layer of ^{57}Fe is put between layers of ^{56}Fe and Cr. The result partial phonon DOS is different than those of inside the ^{56}Fe or Cr layer [71]. to study the interface dynamics of epitaxially grown Sn on $CdTe$ or $InSb$ substrates, we can

first put a single layer or several layer of ^{119}Sn on the substrate, then start growing the other stable isotope of Sn, e.g., ^{118}Sn or ^{120}Sn. Both α-phase and β-phase of Sn can be grown and the dynamical features of these two different interfaces can be investigated by INRS.

INRS has another feature that can be used to study two dimensional systems. The cross section generally depends on the incident beam direction relative to crystal orientation, as it is shown in Eq. (2.35) and that dependence is carried over to the projected phonon DOS (Eqs. 2.47 and 2.48). In thin film experiments, to maximize count rate in the inelastic channel, the incident X-ray beam is always at a grazing angle slightly above the total reflection angle. In such scattering geometry, the term $(\hat{\mathbf{k}} \cdot \vec{\epsilon}_s)^2$ in the above mentioned equations suggests that only the in-plane vibration modes are measured. This feature can be utilized to investigate interface dynamics in samples grown in different orientations.

5.3 High Pressures

High pressure studies are increasingly active. The Diamond Anvil Cells (DACs) can now put samples at over 1 $MBar$ pressure. This opens up another dimension in the phase space of materials. Understanding dynamics under high pressures has profound implications in geophysics and planetary astronomy. We have performed high pressure INRS experiments and obtained Sn-partial phonon DOS for SnO under modest high pressures. This information cannot be obtained with other experimental techniques and is important to understand its thermodynamics under high pressure.

It is possible to perform such measurements for ^{119}Sn samples, and we did it, with current setup described in Chapter 3 and Section 4.2. However, as mentioned in Section 4.2, the setup is not efficient to deel with the small size of DAC sample chamber. Even smaller chamber is needed to get into higher pressure range. The future high pressure INRS experiments will require focused beam. A K-B mirror was used in a ^{57}Fe high pressure INRS experiment where the DAC sample chamber is about 20 μm across and the highest pressure obtained was 150 GPa [72]. K-B mirrors can focus X-ray beam down to micron or less. But their spatial acceptance is still smaller than the typical beam size. To accommodate focusing mirror, we need in-line high resolution monochromator to keep the monochromatized beam in the horizontal plane and retain the small beam size.

Bibliography

[1] R. L. Mössbauer. *Z. Physik*, 151:124, 1958.

[2] S. L. Ruby. *J. de Phys.*, 35:C6–209, 1974.

[3] E. Gerdau, R. Rüffer, H. Winkler, W. Tolksdorf, C. P. Klages, and J. P. Hannon. *Phys. Rev. Lett.*, 54:835, 1985.

[4] G. V. Smirnov. Nuclear resonant scattering of synchrotron radiation. *Hyperfine Interactions*, 97/98:551 – 588, 1996.

[5] G. Faigel, D. P. Siddons, J. B. Hastings, P. E. Haustein, J. R. Grover, J. P. Remeika, and A. S. Cooper. New approach to the study of nuclear Bragg scattering of synchrotron radiation. *Phys. Rev. Lett.*, 58(25):2699, 1987.

[6] T. Ishikawa, Y. Yoda, K. Izumi, C. K. Suzuki, X. W. Zhang, M. Ando, and S. Kikuta. Construction of a precision diffractometer for nuclear Bragg scattering at the Photon Factory. *Rev. Sci. Instrum.*, 63(1):1015, 1992.

[7] T. M. Mooney, T. S. Toellner, W. Sturhahn, E. E. Alp, and S. D. Shastri. High-resolution, large-angular-acceptance monochromator for hard x-rays. *Nucl. Instr. and Meth. A*, 347:348, 1994.

[8] S. Kishimoto. High time resolution x-ray measurements with an avalanche photodiode detector. *Rev. Sci. Instrum.*, 63:824, 1992.

[9] A. Q. R. Baron and S. L. Ruby. Time resolved detection of x-rays using large area avalanche photodiodes. *Nucl. Instr. and Meth. A*, 343:517, 1994.

[10] T. S. Toellner, W. Sturhahn, E. E. Alp, P. A. Montano, and M. Ramanathan. Avalanche photodiodes as large dynamic range detectors for synchrotron radiation. *Nucl. Instr. and Meth. A*, 350:595, 1994.

[11] M. Seto, Y. Yoda, S. kikuta, X. W. Zhang, , and M. Ando. Observation of nuclear resonant scattering accompanied by phonon excitation using synchrotron radiation. *Phys. Rev. Lett.*, 74(19):3828, 1995.

[12] W. Sturhahn, T. S. Toellner, E. E. Alp, X. Zhang, M. Ando, Y. Yoda, S. Kikuta, M. Seto, C. W. Kimball, and B. Dabrowski. Phonon density of states measured by inelastic nuclear resonant scattering. *Phys. Rev. Lett.*, 74(19):3832, 1995.

[13] W. M. Visscher. Study of lattice vibrations by resonance absorption of nuclear gamma rays. *Annals of Phys.*, 9:194, 1960.

[14] K. S. Singwi and A. Sjölander. Resonance absorption of nuclear gamma rays and the dynamics of atomic motions. *Phys. Rev.*, 120(4):1093, 1960.

[15] E. E. Alp, T. M. Mooney, T. S. Toellner, W. Sturhahn, E. Witthoff, R. Röhlsberger, E. Gerdau, H. Homma, and M. Kentjana. Time resolved nuclear resonant scattering from ^{119}Sn nuclei using synchrotron radiation. *Phys. Rev. Lett.*, 70:3351, 1993.

[16] J. G. Stevens and V. E. Stevens, editors. *Mössbauer effect data index.* IFI/Plenum, New York, 1976.

[17] W. Sturhahn, E. Gerdau, R. Hollatz, R. Rüffer, H. D. Rüter, and W. Tolksdolf. *Europhys. Lett.*, 14:821, 1991.

[18] D. E. Johnson, D. P. Siddons, J. Z. Larese, and J. B. Hastings. *Phys. Rev. B*, 51:7909, 1995.

[19] A. Q. R. Baron, A. I. Chumakov, S. L. Ruby, J. Arthur, G. S. Brown, G. V. Smirnov, and U. van Bürck. *Phys. Rev. B*, 51:16384, 1995.

[20] A. I. Chumakov, A. Q. R. Baron, J. Arthur, S. L. Ruby, G. S. Brown, G. V. Smirnov, U. van Bürck, and G Wortmann. *Phys. Rev. Lett.*, 75:549, 1995.

[21] S. Kikuta. In *Satelite meeting, Sixteenth European Crystallographic Meeting on Interference Phenomena in X-ray scattering*, Moscow, 1997.

[22] H. Frauenfelder, editor. *The Mössbauer effect — A review with a collection of reprints.* Frontiers in Physics. W. A. Benjamin, Inc., New York, 1962.

[23] W. Sturhahn and V. G. Kohn. Theoretical aspects of incoherent nuclear resonant scattering. In E. Gerdau and H. de Waard, editors, *Nuclear Resonant Scattering of Synchrotron Radiation.* Baltzer Science Publishers, Oxford, UK, 1999.

[24] L. van Hove. Correlations in space and time and born approximation scattering in systems of interacting particles. *Phys. Rev.*, 95(1):249 – 262, 1954.

[25] H. J. Lipkin. Mössbauer sum rules for use with synchrotron sources. *Phys. Rev. B*, 52(14):10073, 1995.

[26] A. I. Chumakov, R. Rüffer, A. Q. R. Baron, H. F. Grünsteudel H. Grünsteudel, and V. G. Kohn. Anisotropic inelastic nuclear absorption. *Phys. Rev. B*, 56(17):10758, 1997.

[27] V. G. Kohn, A. I. Chumakov, and R. Rüffer. Nuclear resonant inelastic absorption of synchrotron radiation in an anisotropic single crystal. *Phys. Rev. B*, 58(13):8437, 1998.

[28] M. Y. Hu, W . Sturhahn, T. S. Toellner, P. M. Hession, J. P. Sutter, and E. E. Alp. Data analysis for inelastic nuclear resonant absorption experiments. *Nucl. Instr. and Meth. in Phys. Res. A*, 428(2-3):551, 1999.

[29] W. Sturhahn and A. Chumakov. Lamb-Mössbauer factor and second-order Doppler shift from inelastic nuclear resonant absorption. In E. Gerdau and H. de Waard, editors, *Nuclear Resonant Scattering of Synchrotron Radiation.* Baltzer Science Publishers, Oxford, UK, 1999.

[30] Yuri V. Shvyd'ko. private communication.

[31] Alfrad Q. R. Baron. private communication.

[32] N. W. Ashcroft and N. D. Mermin. *Solid State Physics.* Saunders College Publishing, 1976.

[33] P. P. Ewald. Crystal optics for visible light and x rays. *Rev. Mod. Phys.*, 37(1):46 – 56, 1965.

[34] P. P. Ewald. *Ann. Physik*, 49:1, 1916.

[35] P. P. Ewald. *Ann. Physik*, 49:117, 1916.

[36] P. P. Ewald. *Ann. Physik*, 54:159, 1917.

[37] M. von Laue. *Ergeb. Exakt. Naturw*, 10:133, 1931.

[38] W. H. Zachariasen. *Theory of X-ray Diffraction in Crystals.* John Wiley and sons, Inc., 1945.

[39] M. von Laue. *Röntgenstrahlinterferenzen.* Akademische Verlag, Frankfurt, 1948.

[40] R. W. James. *Optical Principles of the Diffraction of X-rays.* G. Bell and Sons, London, 1950.

[41] R. W. James. The dynamical theory of x-ray diffraction. *Solid State Physics*, 15:53, 1963.

[42] B. W. Batterman and H. Cole. Dynamical diffraction of x-rays by perfect crystal. *Rev. Mod. Phys.*, 36:681, 1964.

[43] T. Matsushita and H. Hashizume. X-ray monochromators. In E. E. Koch, editor, *Handbook on Synchrotron Radiation*, volume 1, chapter 4, pages 261 – 314. North-Holland Publishing Co., Amsterdam, 1983.

[44] Thomas S. Toellner. *High-Resolution X-ray Probes Using Nuclear Resonant Scattering.* PhD thesis, Northwestern University, Evanston, Illinois, June 1996.

[45] B. W. Batterman and D. R. Chipman. *Phys. Rev.*, 127(3):690, 1962.

[46] E. Burkel. *Inelastic scattering of X-ray with very high energy resolution*, volume 125 of *Springer Tracts in Modern Physics*. Springer-Verlag, 1991.

[47] R. D. Deslattes. *Ann. Phys.*, 129:378, 1980.

[48] J. W. M. DuMond. Theory of the use of more than two successive x-ray crystal reflections to obtain increased resolving power. *Phys. Rev.*, 52:872, 1937.

[49] M. Y. Hu, T. S. Toellner, W. Sturhahn, P. M. Hession, J. P. Sutter, and E. E. Alp. A high-resolution monochromator for inelastic nuclear resonant scattering experiments using ^{119}Sn. *Nucl. Instr. and Meth. A*, 430(2-3):271, 1999.

[50] A. I. Chumakov, A. Barla, R. Rüffer, J. Metge, H. F. Grünsteudel, H. Grünsteudel, J. Plessel, H. Winkelmann, and M. M. Abd-Elmeguid. Nuclear inelastic scattering of synchrotron radiation by ^{119}Sn. *Phys. Rev. B*, 58(1):254, 1998.

[51] S. Koval, M. G. Stachiotti, R. L. Migoni, M. S. Moreno, R. C. Mercader, and E. L. Peltzer y Blancá. Shell-model lattice dynamics and Mössbauer recoilless fraction of SnO. *Phys. Rev. B*, 54(10):7151, 1996.

[52] F. Gervais and W. Kress. Lattice dynamics of oxides with rutile structure and instabilities at the metal-semiconductor phase transitions of NbO_2 and VO_2. *Phys. Rev. B*, 31(8):4809, 1985.

[53] J. Geurts, S. Rau, W. Richter, and F. J. Schmitte. SnO films and their oxidation to SnO_2: Raman scattering, IR reflectivity and X-ray diffraction studies. *Thin Solid Films*, 121:217, 1984.

[54] J. D. Barnett, V. E. Bean, and H. T. Hall. X-ray diffraction studies on tin to 100 kilobars. *J. of Appl. Phys.*, 37(2):875, 1966.

[55] Pavlin B. Staikov. *First principle studies of the structural and dynamical properties of metals*. PhD thesis, Kansas State University, Manhattan, Kansas, 1998.

[56] D. L. Price, J. M. Rowe, and R. M. Nicklow. Lattice dynamics of grey tin and Indium Antimonide. *Phys. Rev. B*, 3(4):1268, 1971.

[57] T. T. Oh and W. C. Kok. Analytical phonon dispersion relations for diamond-like structures. *Physica Scripta*, 55:99, 1997.

[58] L. R. Testardi. Elastic behavior and structural instability of high-temperature A-15 structure superconductors. In W. P. Mason and R. N. Thurston, editors, *Physical Acoustics*, volume X, chapter 4, page 193. Academic Press, New York and London, 1973.

[59] M. Weger and I. B. Goldberg. Some lattice and electronic properties of the β-Tungstens. In H. Ehrenreich, F. Seitz, and D. Turnbull, editors, *Solid State Physics*, volume 28, page 1. Academic Press, New York and London, 1973.

[60] W. Weber. Displacement correlation functions for some A15 compounds. *J. Phys. F: Met. Phys.*, 17:27, 1987.

[61] J. S. Shier and R. D. Taylor. Temperature-dependent isomer shift and anharmonic binding of Sn^{119} from Mössbauer-effect measurements. *Phys. Rev.*, 174(2):346, 1968.

[62] R. Röhlsberger, W. Sturhahn, T. Toellner, K. Quast, P. Hession, M. Hu, J. Sutter, and E. Alp. Phonon damping in thin films of fe. *J. Appl. Phys.*, 86:584, 1999.

[63] W. Sturhahn *et al.* unpublished.

[64] H. Paulsen, H. Winkler, A. X. Trautwein, H. Grünsteudel, V. Rusanov, and H. Toftlund. Measurement and simulation of nuclear inelastic-scattering spectra of molecular crystals. *Phys. Rev. B*, 59(2):975, 1999.

[65] T. Sage *et al.* unpublished.

[66] P. D. Mannheim. Influence of force-constant changes on the lattice dynamics of cubic crystals with point defects. *Phys. Rev.*, 165(3):1011, 1968.

[67] P. D. Mannheim and S. S. Cohn. Force-constant changes and the crystal impurity problem. *Phys. Rev. B*, 4(10):3748, 1971.

[68] P. D. Mannheim. Localized modes and cell-model limit in the crystal impurity problem. *Phys. Rev. B*, 5(2):745, 1972.

[69] G. Van Landuyt, C. W. Kimball, and F. Y. Fradin. Lattice dynamics of ^{119}Sn impurities in Pd. *Phys. Rev. B*, 15(11):5119, 1977.

[70] S. S. Cohn, R. H. Nussbaum, and D. G. Howard. *Phys. Rev. B*, 12:4095, 1975.

[71] W. Sturhahn, R. Röhlsberger, E. E. Alp, T. Ruckert, H. Schrör, and W. Keune. Phonon density of states in Fe/Cr(001) superlattices and Tb-Fe thin-film alloys. *J. Magn. Magn. Mater.*, 198-199:590, 1999.

[72] H. K. Mao *et al.* unpublished.